Magneto-ionics in CoFeB based systems

Rohit Pachat

To cite this version:

Rohit Pachat. Magneto-ionics in CoFeB based systems. Condensed Matter [cond-mat]. Université Paris-Saclay, 2023. English. NNT : 2023UPAST032 . tel-04486528

HAL Id: tel-04486528
https://theses.hal.science/tel-04486528v1

Submitted on 2 Mar 2024

université
PARIS-SACLAY

Magneto-ionics in CoFeB based systems

Magnéto-ionique dans les systèmes basés sur CoFeB

Thèse de doctorat de l'université Paris-Saclay

École doctorale n° 575 : Electrical, Optical, Bio-Physics and Engineering (EOBE)
Spécialité de doctorat: Electronique, Photonique et Micro-Nanotechnologies
Graduate School : Sciences de l'ingénierie et des systèmes
Référent : Faculté des Sciences d'Orsay

Thèse préparée au **Centre de Nanosciences et de Nanotechnologies** (Université Paris-Saclay, CNRS), sous la direction de **Liza HERRERA-DIEZ**, Chargée de recherche

Thèse soutenue à Paris-Saclay, le 24 Février 2023, par

Rohit PACHAT

Composition du jury

Membres du jury avec voix délibérative

Julie GROLLIER Directrice de recherche, Unité Mixte de Physique CNRS, Thales, France	Présidente
Karin LEISTNER Professeure à la Technische Universität Chemnitz, Allemagne	Rapporteur & Examinatrice
Reinoud LAVRIJSEN Professeur à la Eindhoven University of Technology, Pays-Bas	Rapporteur & Examinateur
Eva PELLICER Professeure à la Universidad Autonoma de Barcelona, Espagne	Examinatrice
Mohamed BELMEGUENAI Maître de conference HDR à l'Université Sorbonne Paris Nord, France	Examinateur
Shimpei ONO Chercheur au CRIEPI, Japon	Examinateur

THESE DE DOCTORAT

NNT : 2023UPAST032

Titre: Magnéto-ionique dans les systèmes basés sur CoFeB

Mots clés: Magnéto-ionique, anisotropie magnétique, réversibilité, interaction Dzyaloshinskii-Moriya, recuit, stabilité.

Résumé: Le contrôle des propriétés magnétiques par le champ électrique dans les couches minces ferromagnétiques est une caractéristique recherchée pour les dispositifs spintroniques, car il offre un grand potentiel pour le développement de dispositifs de mémoire à faible consommation d'énergie. Outre les effets découlant de l'accumulation de charges induite par le champ électrique à l'interface ferromagnétique/diélectrique, la migration d'ions induite par le champ électrique dans les couches diélectriques adjacentes à une couche magnétique a un effet plus étendu, résolvant le filtrage électrostatique et la volatilité des charges. Cette technique est connue sous le nom de magnéto-ionique. Cependant, les défis clés qui pourraient affecter la performance magnéto-ionique, tels que la chimie interfaciale après oxydation, le recuit post-croissance et la stabilité des états magnéto-ioniques, ont été largement négligés dans la littérature. Cette thèse se concentre sur le développement et l'optimisation de systèmes magnéto-ioniques à base de CoFeB en relevant les défis mentionnés ci-dessus et en fournissant des mécanismes physiques sous-jacents plausibles. L'approche utilisée pour l'étude est celle de l'ingénierie de la pile magnétique dans laquelle la magnéto-ionique pour différentes couches tampons de métaux lourds et stœchiométries de CoFeB a été explorée. Dans le chapitre 4, une oxydation induite par une tension de grille dans Ta/$Co_{20}Fe_{60}B_{20}$/HfO_2 montre le changement de l'anisotropie magnétique d'un échantillon tel qu'il a été cultivé, passant d'un état sous-oxydé présentant une anisotropie magnétique dans le plan (IPA) à un état optimalement oxydé présentant une anisotropie magnétique perpendiculaire (PMA), puis à un état suroxydé présentant une anisotropie magnétique dans le plan. Le passage de l'IPA sous-oxydé au PMA optimalement oxydé est appelé régime I et le passage du PMA optimalement oxydé à l'IPA suroxydé est appelé régime II. Le régime II est réversible, alors que le régime I est irréversible dans les mêmes conditions de tension de grille. La coexistence de deux régimes, alors qu'un seul régime est réversible, a été proposée comme étant le résultat de la différence des énergies de liaison des espèces d'oxygène ajoutées à l'interface CoFeB/HfO_2 dans chaque régime, soulignant la fonctionnalité de la chimie interfaciale pour la performance magnéto-ionique. Le chapitre 5 explore l'impact du recuit thermique sur la magnéto-ionique dans un système qui nécessite généralement un recuit pour obtenir la PMA : W/$Co_{20}Fe_{60}B_{20}$/HfO_2. Dans le W/CoFeB/HfO_2, une oxydation induite par la tension de grille des échantillons bruts ne développe pas de PMA, alors que le recuit post-croissance des échantillons bruts développe un PMA qui, après exposition à des tensions négatives, passe à l'IPA en raison de l'oxydation de la couche de CoFeB. En outre, dans les échantillons recuits à 390°C pendant 1 heure, une forte interaction Dzyaloshinskii Moriya (DMI) de 0,60 pJ/m a également été observée, qui a diminué à 0,06 pJ/m après l'oxydation induite par la tension de grille. Bien que les propriétés magnétiques, y compris la vitesse de la paroi du domaine, se soient considérablement améliorées avec l'augmentation de la température et de la durée du recuit, la réversibilité magnéto-ionique s'est avérée de plus en plus compromise. Cette disparité dans la réversibilité après différentes conditions de recuit a été associée à l'influence de la cristallisation du CoFeB sur la mobilité des ions. Dans le chapitre 6, une oxydation de la couche de CoFeB induite par une tension de grille dans Pt/$Co_{60}Fe_{20}B_{20}$/HfO_2 montre la coexistence de deux régimes, comme pour Ta/$Co_{20}Fe_{60}B_{20}$/HfO_2 ; Cependant, les deux régimes sont réversibles, ce qui établit un lien entre le rôle de la stoechiométrie du CoFeB et la réversibilité. La stabilité des états magnéto-ioniques étudiés dans chaque régime montre que le régime I est significativement plus stable que le régime II, qui évolue avec le temps. De plus, la stabilité des états magnéto-ioniques est significativement améliorée lorsque l'épaisseur du HfO_2 est réduite. Cette disparité dans la stabilité des états magnétiques dans les régimes I et II et les différentes épaisseurs de HfO_2 a été liée à la force de liaison des espèces d'oxygène à l'interface CoFeB/HfO_2 et à la disponibilité de sites "déficients" en oxygène en raison des atomes de Hf avec des espèces d'oxygène moins incorporées à l'interface, respectivement. Les résultats présentés dans cette thèse révèlent la complexité de la magnéto-ionique dans divers systèmes, montrant l'importance de la chimie interfaciale, de la structure et de la composition de l'empilement magnétique, et la stabilité des états magnétiques non volatiles, et fournissent des mécanismes sous-jacents plausibles pour aider à comprendre et à concevoir des dispositifs spintroniques efficaces basés sur la magnéto-ionique.

ÉCOLE DOCTORALE
Physique et ingénierie :
Electrons, Photons,
Sciences du vivant (EOBE)

Title: Magneto-ionics in CoFeB based systems

Keywords: Magneto-ionics, magnetic anisotropy, reversibility, Dzyaloshinskii-Moriya interaction, annealing, stability

Abstract: Electric field control of magnetic properties in ferromagnetic thin films is a sought-after feature for spintronics devices, as it offers great potential for developing energy-efficient memory devices. In addition to the effects arising from electric field-induced charge accumulation at the ferromagnet/dielectric interface, electric field-induced migration of ions in dielectric layers adjacent to a magnetic layer shows a more extended effect, resolving electrostatic screening and volatility of charges. Such a technique is known as magneto-ionics. However, key challenges that could affect the magneto-ionic performance such as the interfacial chemistry after oxidation, post-growth annealing and the stability of the magneto-ionic states have been largely overlooked in the literature. This thesis focuses on developing and optimizing CoFeB-based magneto-ionic systems addressing the above-mentioned challenges and provides plausible underlying physical mechanisms. The approach carried out to investigate is by magnetic stack engineering in which magneto-ionics for different heavy metal buffer layers and stoichiometry of CoFeB were explored. In chapter 4, a gate voltage-induced oxidation in $Ta/Co_{20}Fe_{60}B_{20}/HfO_2$ shows the change of magnetic anisotropy of an as-grown sample from an under-oxidized state exhibiting in-plane magnetic anisotropy (IPA) to an optimally oxidized state exhibiting perpendicular magnetic anisotropy (PMA) and further into an overoxidized state exhibiting IPA. The transition from the underoxidized IPA to optimally oxidized PMA is called regime I and optimally oxidized PMA to overoxidized IPA is called regime II. Regime II is found to be reversible, whereas regime I is irreversible under the same gate voltage conditions. The coexistence of two regimes, where only one regime is reversible, has been proposed to be as a result of the difference in the binding energies of the oxygen species added to the $CoFeB/HfO_2$ interface in each regime, pointing out the functionality of interfacial chemistry for magneto-ionic performance. Chapter 5 explores the impact of thermal annealing on magneto-ionics in a system that typically requires annealing to obtain PMA: $W/Co_{20}Fe_{60}B_{20}/HfO_2$. In $W/CoFeB/HfO_2$, a gate voltage-induced oxidation of the as-grown samples does not develop PMA, whereas post-growth annealing of the as-grown samples develops PMA, which after exposing to negative voltages transitions to IPA due to oxidation of the CoFeB layer. In addition, in the samples annealed at 390°C for 1 hour, a strong Dzyaloshinskii Moriya interaction (DMI) of 0.60 pJ/m was also observed, which decreased to 0.06 pJ/m after gate voltage-induced oxidation. Although magnetic properties, including domain wall velocity, improved drastically with increasing annealing temperature and time, the magneto-ionic reversibility was found to be increasingly compromised. This disparity in reversibility after different post-grown annealing conditions has been associated with the influence of crystallization of CoFeB on ion mobility. In chapter 6, a gate voltage-induced oxidation of the CoFeB layer in $Pt/Co_{60}Fe_{20}B_{20}/HfO_2$ shows the coexistence of two regimes, similarly to $Ta/Co_{20}Fe_{60}B_{20}/HfO_2$; however, both regimes are reversible, linking the role of the stoichiometry of CoFeB and reversibility. The stability of the magneto-ionic states studied in each regime shows that regime I is significantly more stable than regime II, which evolves with time. In addition, the stability of the magneto-ionic states was significantly improved when the thickness of the HfO_2 was reduced. This disparity in the stability of the magnetic states in regimes I and II and different thicknesses of HfO_2 has been linked to the binding strength of the oxygen species at the $CoFeB/HfO_2$ interface and the availability of oxygen "deficient" sites due to the Hf atoms with less incorporated oxygen species at the interface, respectively. The results presented in this thesis reveal the complexity of magneto-ionics in various systems, showing the importance of interfacial chemistry, structure and composition of the magnetic stack, and the stability of the non-volatile magnetic states, and provide plausible underlying mechanisms to help understand and design efficient spintronics devices based on magneto-ionics.

ACKNOWLEDGMENTS

The assistance I received from people both within and outside the laboratory, along with the funding provided by the European Union's Horizon 2020 research and innovation programme under the Marie Skłodowska-Curie grant agreement No. 860060, were instrumental in enabling the scientific findings presented in this manuscript. First and foremost, I would like to thank my supervisor, Dr. Liza Herrera-Diez, for her great guidance throughout my PhD. I really learned a lot from you and I am thankful for your constant support. I am also grateful to Dr. Dafiné Ravelosona for his unwavering availability to discuss both fun and scientific topics. I really enjoyed our short yet helpful conversations with you. Many thanks to Dr. Damien Querlioz for being an incredible down-to-earth group leader and being open to discuss scientific and non-scientific matters. I am privileged to express my sincerest thanks to Prof. Karin Leistner and Dr. Reinoud Lavrijsen, my defense reviewers, for the invaluable feedback and constructive criticism that have played a pivotal role in helping me improve my defense and thesis. Additionally, Reinoud's warm hospitality during my secondments at TU Eindhoven was remarkable. I acquired a wealth of knowledge from you, Prof. Bert Koopmans, and the FNA team during my stay at TU/e. I would also like to thank the president, Dr. Julie Grollier, and the examiners, Dr. Eva Pellicer, Dr. Mohamed Belmeguenai, and Dr. Shimpei Ono, for accepting their role and providing great feedback.

I would like to express my sincere gratitude to my dear colleagues and friends from C2N who have made the work environment more enjoyable than I could have ever imagined. From my office, I want to give a special thanks to Atreya for being an excellent office mate, engaging in fun discussions, and introducing me to the Parisian restaurant I had been longing to try. Sometimes, your descriptions of the food were even better than the food itself! Kamel, thank you for being extremely helpful and for organizing the trip to the south of France, and other fun events. I had a wonderful time! Subhajit, I appreciated your great company during our random coffee breaks, VSM measurements, helpfulness, and all the discussions about food and money. I was amazed at how much you loved Indian desserts and a particular vegetable! Gyan, thank you for your great support and suggestions for my project and for organizing pizza Fridays, even though I couldn't attend most of the time. Tanvi, I'm grateful for all the ridiculous (yet fun) discussions we had and for helping me a lot with the VSM measurements. Xing, thanks for the enjoyable discussions and for always being kind and helpful. Clément, your constant reminders that I was awesome really made my day! Axel, thank you for the peaceful coffee breaks after lunch. Amine, I enjoyed all the wild (yet fun) conversations we had. Thibaut, thank you for being great company and for the free rides to Paris. Roméo, your scientific discussions were really helpful in understanding several concepts. Benjamin, thanks for sharing your PhD life. Finally, I'd like to express my sincere appreciation to Maryam, Marie, Sukanya, Ritwik, Elmer, Corina, Mamour, Song, Amina, and Asma for being so helpful and for making the work environment truly beautiful.

I would like to express my gratitude to everyone at C2N who played a role in ensuring the smooth functioning of the lab. Special thanks to Christophe Chassat and Alain Péan from the IT department, Léa Lemaître, Bernadette Laborde and Marina Ferreira from the administration team for handling the expenses. Many thanks to Dr. Sophie Bouchoule and Emilia Davodeau from the doctoral school for my registration. I would also like to extend my appreciation to the receptionists, securities, logistics team and janitors.

Next, I would like to thank everyone from my innovative training network called MagnEFi. Even though our first interaction was online, we quickly formed a strong connection that only grew stronger when we finally met in person in Turin for our first in-person MagnEFi meeting. I would like to express my sincere gratitude to Mandy for taking care of all the early stage researchers (ESRs). I had a great time during your secondment at C2N. It was great meeting you and thanks very much for all the memorable moments and help, including depositing the samples for my project. Thanks a lot, Adriano, for all the help and support you showed for our projects together. Also, thanks a lot for being a great ESR representative. Thanks a lot, Jintao, for keeping good company, caring, and being really helpful. Thanks a lot, Adrien, for constantly making sure everyone was doing good emotionally and your constant availability to help. Thanks a lot, Pingzhi, for the wonderful experiments we did together at TU/e and the discussions. Thanks a lot, Cristina, for helping me with the domain wall motion experiments and keeping good company at Institut Néel. Thanks a lot, Mouad, for all the fun topics that we discussed and the coffee breaks we had during your secondment at C2N. Thanks a lot, Giovanni, for the wonderful time we had in the Netherlands during our secondments. I really enjoyed exploring cities with you. Thanks a lot, Beatrice, for keeping good company and all the fun and serious discussions we had during your secondment at C2N. Thanks a lot, Golam, Sreeveni, and Adithya, for keeping good company during all our MagnEFi meetings and your secondments at C2N. I would also like to extend my gratitude to Prof. Luis Lopez-Diaz, Prof. Gianfranco Durin, and Dr. Andreas Kehlberger for the enjoyable conversations we had, and Dr. Stefania Pizzini for being a gracious host during my secondment at Institut Néel

I would like to express my sincere gratitude to all my collaborators and friends. Special thanks to Djoudi for helping me with the BLS measurements and analyses and keeping great company when I was at Université Paris Sorbonne Nord. You have been very kind and helpful. Thanks a lot, Dr. Yves Roussigné and Dr. Mohamed Belmeguenai, for all the scientific discussions regarding BLS and fun topics. I really enjoyed working in your lab. Many thanks to Dr. Alessio Lamperti for all the XPS measurements and analyses. It played a crucial role in understanding and explaining the results of my project. Thanks a lot Dr. Ludovic Largeau for the XRD measurements and discussions. Thanks a lot, Nitin, for being really helpful, supportive, and keeping good company. Thanks a lot, Milad, for being really helpful, providing all the suggestions, and occasional meetups to find great restaurants in Paris. Thanks a lot, Caitlin, for keeping good company. Thanks a lot, Victoire, for your invaluable support for my defense. I wish you the best for your great future plans.

Finally, and importantly, I would like to express my heartfelt gratitude to my parents and brother for your unconditional love and support throughout my life.

Contents

1 - INTRODUCTION AND MOTIVATION

1.1 . Spintronics

Spintronics, also known as spin electronics, is a field of technology in which the charge as well as the spin property of the electron is used in devices. The discovery of giant magnetoresistance effect (GMR) in 1988 [1] by the team of Albert Fert and, independently, by Peter Grunberg and coworkers in 1989 [2] is usually considered as the starting line of the field of spintronics, for which its discoverers received the Nobel Prize in Physics in 2007. In a GMR structure, two ferromagnetic (FM) thin films sandwich a thin non-magnetic metal (spacer), in which the magnetization in both FM thin film layers can be set either parallel or antiparallel. The GMR effect describes the large difference in electrical resistance between the parallel and anti-parallel alignments, occuring due to spin-dependent scattering in the FM thin film layers. Similar to the GMR effect, higher magnetoresistances could be achieved in a magnetic tunnel junction in which the metal spacer is replaced by an insulating spacer. This effect is known as tunnel magnetoresistance (TMR), discovered by Michel Jullière in 1975 [3]. An illustration of the GMR and

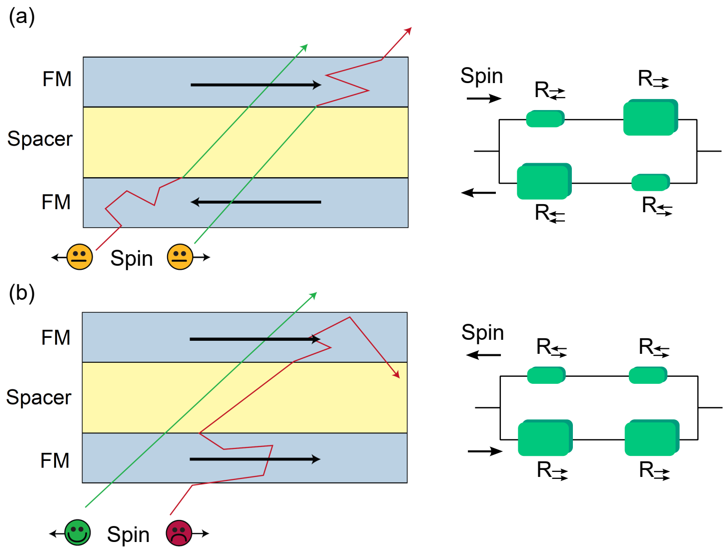

Figure 1.1: Schematic view of a GMR (when the spacer is a non-magnetic metal) and a TMR (when the spacer is an insulator) structure showing the scattering of spin up and spin spin down electrons resulting in: (a) a high resistance state in the anti-parallel configuration of magnetization, and (b) a low resistance state in the parallel configuration of magnetization. The images are adapted from [4].

TMR effects showing high and low resistance states corresponding to antiparallel and parallel alignments of the FMs is shown in Figure 1.1. The GMR and TMR effects highly increased the sensitivity of the magnetic-field sensor in the read heads of the magnetic hard-disk drives (HDD), enabling the development of data storage from 2000 bits per square inch to 1 Terabit per square inch [5].

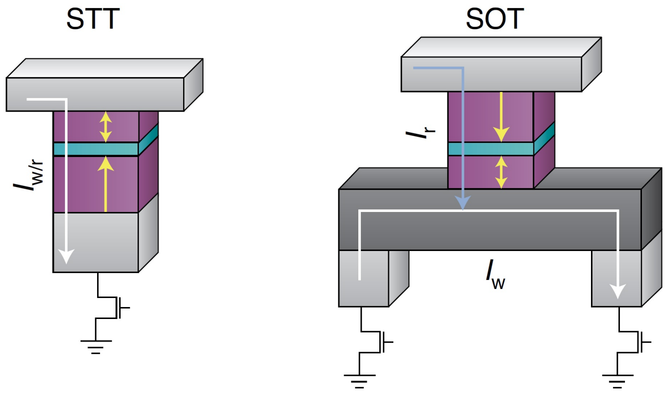

Figure 1.2: Two terminal spin transfer torque (STT) MRAM (on the left), and three terminal spin-orbit torque (SOT) MRAM. I$_w$ and I$_r$ are write current and read current, respectively. Adapted from [6]

Spintronics, nowadays, is developing the next generation of memory and logic devices such as magnetic random access memory (MRAM) [7], and the more experimental racetrack memory [8]. The first commercial MRAM chip was released in 2006 [9]. The field-switched MRAMs were however, limited by scalability as shrinking the device required an increased switching field distribution width that affected the write currents and error rates and also resulted in a critical reduction of data retention times [6]. The discovery of spin transfer torque (STT) [10, 11] and spin-orbit torque (SOT) [12] enabled a great leap forward in the development of MRAMs in terms of nonvolatility, scalability, fast switching, energy efficiency and durability [6]. In STT, a charge current passing through a ferromagnetic layer gets spin-polarized through the s-d exchange interaction, which then exerts a torque to the ferromagnetic layer it flows through by transferring the angular momentum. In the case of SOT, a spin polarized current is generated in a heavy metal adjacent to the ferromagnetic layer by the spin Hall effect [13–15] and Rashba effect [16, 17]. The spin current accumulated in the heavy metal then diffuses into the ferromagnetic layer exerting a torque (spin-orbit torque) to switch the magnetization. A schematic representation of the STT-MRAM and SOT-MRAM is shown in Figure 1.2.

The racetrack device consists of a magnetic strip, in which the data bits ("0"s and "1"s) are stored in magnetic domains with opposite magnetization directions as shown in Figure 1.3. Reading and writing information is done electrically and the data can be shifted along the magnetic strip using STT or SOT assisted domain wall motion by sending current pulses through the magnetic strip. Figure 1.4 shows

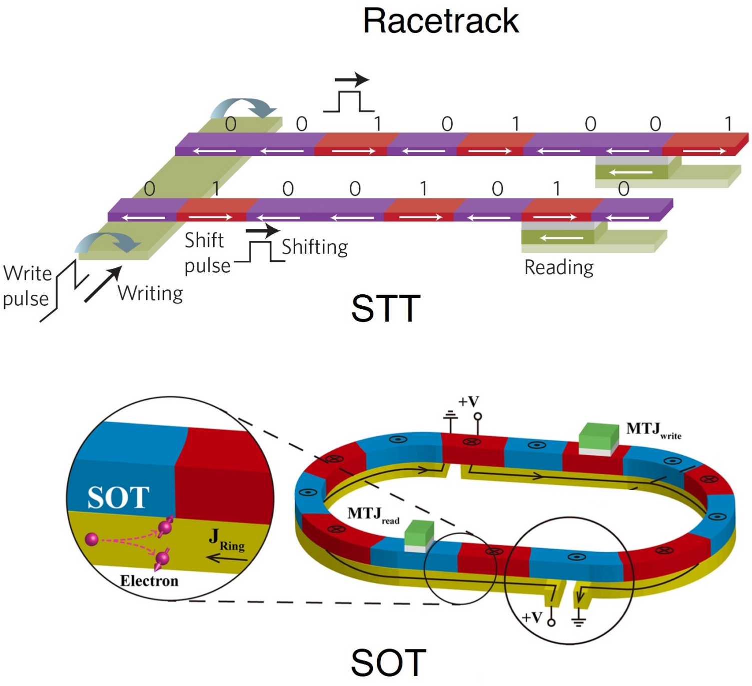

Figure 1.3: Schematic view of an STT racetrack memory (on the left). A write current pulse on the left generates magnetic fields to reverse the direction of magnetization in the desired direction. A shift current pulse is then sent through the magnetic strip that exerts spin transfer torque and shifts all the domain walls in the direction of shift pulse. To read, a magnetic tunnel junction is used. Adapted from [18]. SOT racetrack (on the right) that relies on spin-orbit torque current to move the domain walls. Adapted from [6, 19]

a timeline of some of the major milestones in the history of spintronics research and devices and a rapidly progressing interest in MRAM [20].

A comparison of different memory technologies such as dynamic RAM (DRAM), static RAM (SRAM), perpendicular STT-MRAM (pSTT-MRAM), and SOT-MRAM is shown in Figure 1.5. It may be noted that the MTJ pillar diameter of 35 nm in MRAM technology and the energy consumption in STT-MRAM are substantially larger than the complementary metal oxide semiconductor (CMOS) node. Hence, an improvement in density by downscaling is required for MRAM to be competitive with the current CMOS technology. The larger energy consumption/dissipation in STT-MRAM is due to Ohmic conduction from the charge current. In STT-MRAMs, to downscale to smaller technological nodes, thermal stability must be retained, which requires an increased magnetic anisotropy that in turn would lead to a need for higher switching currents. SOT-MRAMs on the other hand offer high speed, but require larger writing currents and in some configurations, SOT alone cannot switch a perpendicular magnetization deterministically, requiring a static magnetic field [6]. As a consequence, there is a pressing need to develop

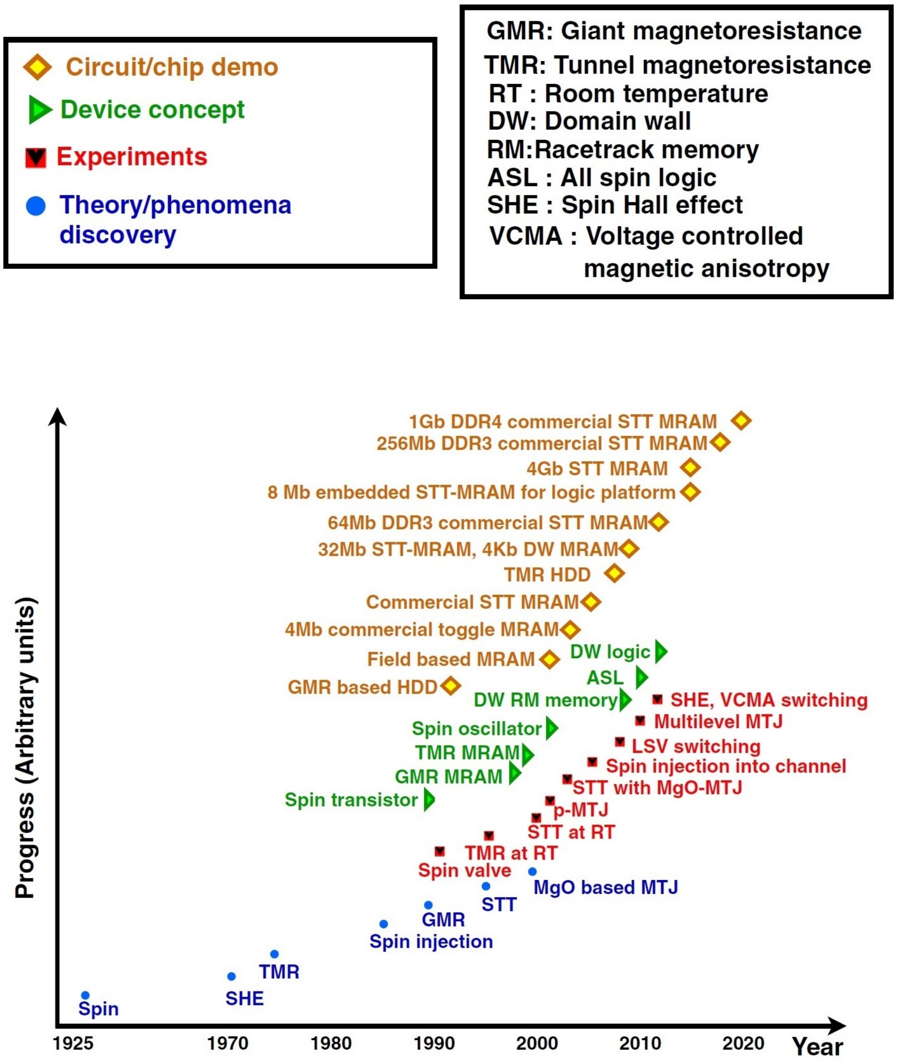

Figure 1.4: Timeline of some of the major milestones in the history of spintronics research and devices. Adapted from [20].

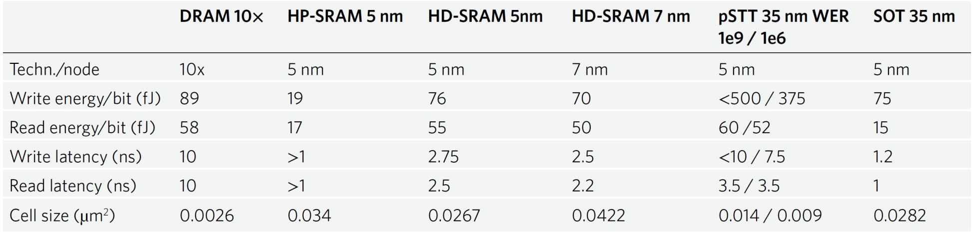

	DRAM 10×	HP-SRAM 5 nm	HD-SRAM 5nm	HD-SRAM 7 nm	pSTT 35 nm WER 1e9 / 1e6	SOT 35 nm
Techn./node	10x	5 nm	5 nm	7 nm	5 nm	5 nm
Write energy/bit (fJ)	89	19	76	70	<500 / 375	75
Read energy/bit (fJ)	58	17	55	50	60 /52	15
Write latency (ns)	10	>1	2.75	2.5	<10 / 7.5	1.2
Read latency (ns)	10	>1	2.5	2.2	3.5 / 3.5	1
Cell size (μm^2)	0.0026	0.034	0.0267	0.0422	0.014 / 0.009	0.0282

Figure 1.5: A comparison of the properties of different memory technologies. Adapted from [6].

energy-efficient means to manipulate magnetic properties.

A novel solution circumventing the key issues of downscaling the devices while keeping both a high thermal stability and good perspectives for low power operation is based on electric field gating of magnetism [6]. The device geometry needed for such a technique is that of a capacitor, where one of the plates is the magnetic layer, which only requires energy to charge. The general principle behind electric field control of magnetism is the electric field-induced changes in magnetic anisotropy in a magnetic material due to the changes in the electronic density close to the Fermi level, for instance, the density of 3*d* electrons in ferromagnets [21]. The concept of the influence of electric fields on magnetism was first explored theoretically in [22–24], where magnetocrystalline anisotropy energies were found to depend on the bandfilling in materials such as Co, Ni and Fe [24]. The first experimental demonstration of electric field manipulation of magnetic properties was reported in 2000 [25] in a diluted magnetic semiconductor (In,Mn)As. In this system, an applied negative voltage was shown to increase the hole concentration that enhanced the ferromagnetic interaction among Mn ions, whereas positive gate voltages had an opposite effect [25]. Since then, a large number of works have emerged focusing on the influence of electric fields on magnetic materials [26]. The electric field effects on magnetism in metals was first demonstrated and reported in 2007 for thin films of FePt and FePd [27]. In this study, a change in coercivity of FePt and FePd at room temperature was reported for an applied gate voltage, owing to the electrical double layer formation that mediated the surface charge accumulation/depletion as shown in Figure 1.6 [27].

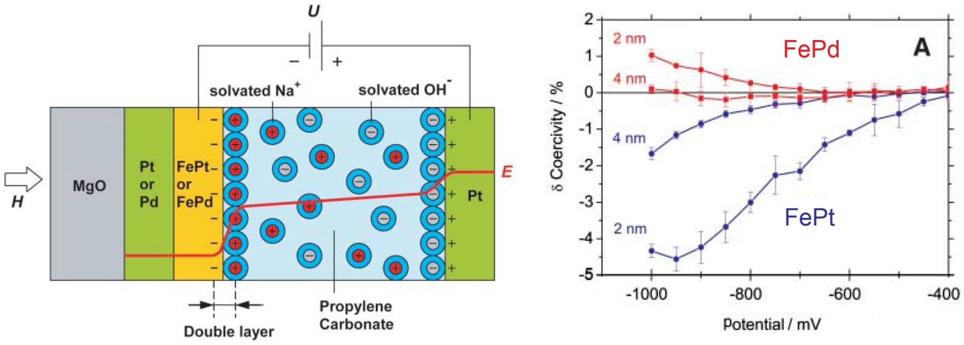

Figure 1.6: A schematic of the electrolytic gating of FePt or FePd film showing the formation of an electric double layer under an applied potential *U* (on the left). Changes in the coercivity of FePd (red) and FePt (blue) as a function of applied potential for different thicknesses of the films (on the right). Adapted from [27].

Charge based effects on magnetic properties have been shown to be a very efficient tool to control magnetic phase transition [25], perpendicular magnetic anisotropy (PMA) [21], domain wall pinning and velocities [28, 29], Dzyaloshinksii-Moriya interaction (DMI) [30, 31], skyrmions [32] and significantly reduce the MTJ switching current density [33]. In addition, recently, a device architecture that combines STT, and SOT with voltage controlled magnetic anisotropy (VCMA) has reported to improve the switching time [6, 34]. It is worth mentioning that the most accessible region to generate the electric field changes in the electronic density is the surface of a magnetic material, hence a large surface to volume ratio is required.

In addition to the conventional charge accumulation effects, electric fields can also be used to induce ion migration inside an oxide at the interface with a ferromagnetic layer. This gate voltage-driven ion migration and subsequent interaction with a magnetic material have been reported to show a more extended effect over the entire magnetic layer, including the second interface of a thin magnetic layer [35], and can also provide nonvolatility [36], resolving charge volatility and electrostatic screening [37] in ferromagnets. This technique, where the modulation of magnetic properties achieved via the migration of ions toward/away from the magnetic interface using a voltage is known as magneto-ionics [38]. Magneto-ionic gating has gained great interest in the recent years due to the possibility of large, nonvolatile modulation of magnetism and the extremely large magneto-electric efficiency of the order of approximately 5000 fJ/Vm [38]. This holds a great promise for the development of improved energy-efficient spintronics devices.

Despite the potential for magneto-ionics to develop energy efficient spintronics devices, there are several challenges that must be surmounted in order to advance research in this emerging field. Among the primary challenges are a lack of comprehension regarding the impact of interfacial chemistry on the reversibility of the process and the underlying physical mechanisms, which hinders the design and optimization of materials for specific applications. Additionally, the difficulty of designing and tuning materials with the desired properties for specific applications, such as amorphous and crystalline magnetic thin films, where thermal annealing is used to enhance crystallinity and magnetic properties of the films, presents a major challenge. This requires a deep understanding of the role of magnetic interfaces and ion mobility in amorphous and crystalline systems. Lastly, magneto-ionics involves complex interactions between ions and materials, and the stability of the non-volatile magnetic states with time must be addressed for the development of spintronics devices applications.

In this thesis, the effect of magneto-ionic gating on magnetic properties in systems based on CoFeB/HfO_2 is presented, highlighting the magneto-ionic reversibility and the complex interaction between mobile ions and the magnetic atoms.

Layout of this thesis

The outline of this thesis is as follows:

- **Chapter 2: BACKGROUND AND THE STATE OF THE ART**
  In this chapter, the fundamental concepts necessary to understand the results presented in this thesis are introduced including magnetic energies of a ferromagnet, and the development and the state of the art in magneto-ionics.

- **Chapter 3: METHODOLOGY**
  In this chapter, a description of the sample preparation methods and the measurement methods used throughout this thesis is presented.

- **Chapter 4: MAGNETO-IONICS IN Ta/CoFeB/HfO$_2$: MULTIPLE MAGNETO-IONIC REGIMES**
  The interest in non-volatility for spintronics applications goes hand in hand with magneto-ionic reversibility. In this chapter, the magneto-ionic behavior of Ta/CoFeB/HfO$_2$ is discussed, where two distinct magneto-ionic regimes have been identified in a single structure. In addition, the chapter also describes the magneto-ionic effects on the effective damping parameter α_{eff}, largely overlooked in the literature and of great importance for fast magnetization dynamics.

- **Chapter 5: MAGNETO-IONICS IN W/CoFeB/HfO$_2$: THE EFFECTS OF POST-GROWTH ANNEALING**
  Post-growth annealing is vital to achieving robust magnetic properties in CoFeB-based materials through crystallization. In this chapter, the magneto-ionic modulation of the Dzyaloshinskii-Moriya interaction (DMI) and PMA in W/CoFeB/HfO$_2$ stacks annealed at different temperatures and for varying annealing times is presented. In addition, the dependence of magneto-ionic reversibility on post-grown annealing has been investigated.

- **Chapter 6: MAGNETO-IONICS IN Pt/CoFeB/HfO$_2$: EVALUATING THE EFFECTS OF TIME EVOLUTION**
  A key factor that determines the potential application of a device is its stability. In this chapter, the stability of the magneto-ionic states of Pt/CoFeB/HfO$_2$ is discussed. Similarly to Ta/CoFeB/HfO$_2$, two magneto-ionic regimes have been identified in Pt/CoFeB/HfO$_2$. However, the stability in each regime shows very distinct behavior, where regime I is more stable than regime II. In addition, the influence of the thickness of HfO$_2$ on stability has been investigated.

2 - BACKGROUND AND STATE OF THE ART

The magnetic heterostructure used throughout this thesis are stacks of heavy metal/ ferromagnet/oxide, which have been subjected to electric fields in order to tune the interfacial anisotropy and DMI. In the following, the energetics of a ferromagnet that determine the magnetic configuration and dynamics of a ferromagnet, and the DMI are oulined.

2.1 . Magnetic energies

The magnetic configuration and the dynamics of a ferromagnet is governed by a compromise between the following competing energies:

$$E_{\text{Total}} = E_{\text{exchange}} + E_{\text{dipolar}} + E_{\text{anisotropy}} + E_{\text{Zeeman}}, \tag{2.1}$$

where E_{Total} is the total energy comprising exchange, dipolar, anisotropy, and Zeeman energies.

Exchange energy is a short range interaction between neighboring spins that is of pure quantum mechanical origin and involves wavefunction overlap. The main element of such interaction is the Coulomb repulsion between electrons. For a system with several electrons with spins $\vec{S_i}$, the Hamiltonian of the exchange interaction is expressed as,

$$\mathcal{H}_{\text{exchange}} = -\sum_{i<j} J_{ij} \vec{S_i}.\vec{S_j}, \tag{2.2}$$

where J_{ij} is the Heisenberg exchange constant. For a ferromagnet, J_{ij}>0, resulting in parallel alignment of neighboring spins.

Dipolar interaction is a long-range interaction that describes the influence of the magnetic field generated by spins in a system on each spin. This field is known as dipolar field or magneto-static field (H_{d}) or stray field (outside the material) or demagnetizing field (inside the material). The Dipolar interaction can be determined by the volume integral of a magnetic system and is expressed as:

$$E_{\text{dipolar}} = -\frac{\mu_0}{2} \iiint_V \boldsymbol{M}.H_{\text{d}}\, dV, \tag{2.3}$$

where $\boldsymbol{M}$ is the magnetization of the material and μ_0 is the permeability of free space. This long-range and non-local behavior of the dipolar interaction makes it difficult to estimate analytically, but can be simplified by introducing the concept of magnetic charges (analogous to electric charges). Eq. 2.3 can then be expressed in terms of surface and volume magnetic charges; volume magnetic charges arise when the magnetization is nonuniform and surface magnetic charges arise when the magnetization has a component perpendicular to an internal or an external surface. Consequently, considering only the dipolar interaction, the divergence of $\boldsymbol{M}$ has to be small in order to minimize volume charges and to minimize the surface charges, the magnetization tends to align parallel to the edges and surfaces of a material. Hence, the shape of the system strongly impacts the dipolar interaction, inducing a shape anisotropy. For instance, in the case of ferromagnetic thin films shown in Figure 2.1 with uniform magnetization and dimensions (l, w, t), the magnetization aligns along the longest dimension (l) of the thin film as it minimizes the magnetic surface charges and the dipolar energy is given by,

$$E_{\text{dipolar}} = \frac{\mu_0 M_{\text{s}}^2}{2} cos^2\theta = K_{\text{d}} cos^2\theta, \tag{2.4}$$

where M_{s} is the saturation magnetization, K_{d} is the shape anisotropy constant (in J/m^3) and θ is the angle between the magnetization and the film normal. Hence, the shape anisotropy favours in-plane magnetization for thin films.

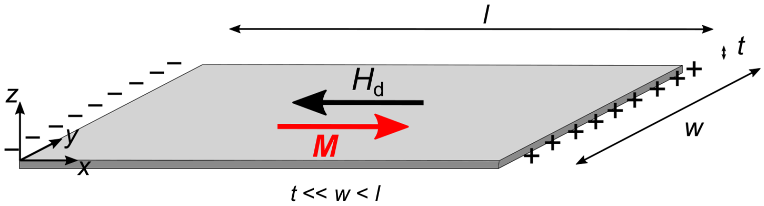

Figure 2.1: A schematic representation of the demagnetizing field in a uniformly magnetized ferromagnetic thin film. +/- are the magnetic surface charges generated by the uniform magnetization.

Anisotropy energy describes the preferential orientation of magnetization that originates from the crystallography, shape and interfaces of a material.

Magnetocrystalline anisotropy energy (E_{mc}) is associated with the crystallographic directions of a material that originates from the crystal field. In the presence of spin-orbit coupling, the spins tend to align along certain crystallographic directions (known as easy axes) in order to minimize the spin-orbit coupling energy. A type of magnetocrystalline anisotropy is uniaxial anisotropy, for instance, present in hexagonal close-packed Co, which is simplified (in the second-order approximation) as,

$$E_{\text{mc}} = K_1 sin^2\alpha, \tag{2.5}$$

where K_1 is the volume uniaxial anisotropy constant (in J/m^3) and α is the angle between the magnetization and the easy axis.

Interfacial magnetic anisotropy (E_s) in ferromagnetic thin films is the anisotropy generated at the interfaces due to the broken translational symmetry. It was first predicted by Louis Néel [39] that at an interface or a surface, the environment an atom sees is different from that of the bulk and hence interfacial or surface anisotropy is enhanced in thin films and negligible in bulk materials. The surface anisotropy energy can be described as [40],

$$E_\mathrm{s} = \frac{K_\mathrm{s}}{t} sin^2\theta, \tag{2.6}$$

where K_s is the surface anisotropy constant (in J/m^3), t is the thickness of the ferromagnet and θ is the angle between the magnetization and film normal. It may be noted that K_s has contributions from two interfaces. Such a contribution can bring the easy axis of magnetization to out-of-plane (OOP), leading to perpendicular magnetic anisotropy (PMA). The effective magnetic anisotropy constant (K_eff) is thus expressed as [41],

$$K_\mathrm{eff} = K_1 + \frac{K_\mathrm{s}}{t} - \frac{\mu_0 M_\mathrm{s}^2}{2} \tag{2.7}$$

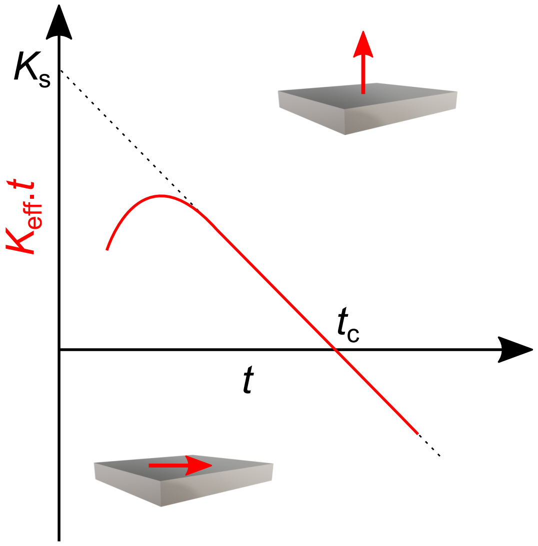

Figure 2.2: A schematic plot of the variation of $K_\mathrm{eff}.t$ as a function of the thickness of a ferromagnet showing the spin reorientation transition between PMA and in-plane anisotropy (IPA) at the critical thickness t_c and the surface anisotropy constant K_s.

If the interface anisotropy is large enough such that $K_\mathrm{eff}>0$, the system promotes an OOP easy axis, giving rise to PMA. From eq. 2.7, it is possible to calculate a critical ferromagnet thickness (t_c) above which the magnetization lies in the sample plane. In addition, for ultra-thin ferromagnetic films without texturing [41], the shape anisotropy dominates the volume contribution to the anisotropy and hence, from a plot of the variation of $K_{\mathrm{eff}}.t$ as a function of the thickness of a ferromagnet, t_{c} and K_{s} can be calculated as shown in Figure 2.2.

Zeeman energy (E_{Zeeman}) is the energy associated with aligning the magnetization of a system along the direction of an applied magnetic field (H). It is expressed as,

$$E_{\mathrm{Zeeman}} = -\mu_0 M_{\mathrm{s}} \boldsymbol{m}.H, \tag{2.8}$$

where $\boldsymbol{m}$ is the reduced magnetization vector ($\boldsymbol{M}/\boldsymbol{M}_{\mathrm{s}}$).

2.2 . Dzyaloshinskii-Moriya interaction

The Dzyaloshinskii-Moriya interaction (DMI) is an antisymmetric exchange interaction between localized spins that arises due to the spin-orbit coupling in magnetic systems lacking structural inversion symmetry [42]. The DMI energy between two neighboring spins $\vec{S_1}$ and $\vec{S_2}$ is given by

$$\mathcal{H}_{\mathrm{DMI}} = -\vec{D}\,.\,[\vec{S_1}\,\mathrm{x}\,\vec{S_2}], \tag{2.9}$$

where $\vec{D}$ is the DMI vector that depends on the crystal symmetry and spin-orbit coupling [43]. DMI favors an orthogonal alignment between $\vec{S_1}$ and $\vec{S_2}$ with a handedness or chirality that is determined by the direction of $\vec{D}$ unlike Heisenberg exchange interaction that favors collinear arrangement. The DMI is one of the key elements that stabilizes chiral magnetic structures such as Néel domain walls and skyrmions [44], which is of great importance for the development of spintronics devices such as racetrack memory.

The DMI was first reported by Igor Dzyaloshinsky in 1958 to explain the observation of a non-zero, weak ferromagnetism in antiferromagnetic α-Fe_2O_3 in which the interaction was linked to the crystal symmetry and magnetic configuration [45]. Two years later, Tôru Moriya explained the interaction by taking into account the spin-orbit coupling in crystals without inversion symmetry [43]. The DMI can exist in bulk non-centrosymmetric crystals such as MnSi [46] and FeGe [47] in which the interaction originates in the bulk and is known as bulk-DMI. In addition, the DMI can also arise in thin film heterostructures such as heavy metal/ferromagnet/(metal oxide or heavy metal). In such structures, DMI originates at the interfaces between heavy metal/ferromagnet [48] and/or ferromagnet/metal oxide [49], where inversion symmetry is absent and is referred to as interfacial-DMI.

2.3 . Magneto-ionics in a nutshell

Magneto-ionics in essence is a route of voltage control of magnetism, where the changes in magnetic properties are achieved by ionic modulation of magnetic interfaces. In this technique, an ionic conductor is placed adjacent to a magnetic material, which under an external voltage, supports ion migration and/or electrochemical reactions that affect the magnetic material. Solid ionic conductors are typically gate dielectrics such as GdO_x [38], HfO_2 [35] and ZrO_2 [50]. In an electrochemical cell, ions move in a liquid electrolyte solution such as KOH [51] and LiOH [52]. Figure 2.3 shows a magneto-ionic device illustrating the migration of ions under a voltage and the changes in saturation magnetization and coercivity that can be induced by magneto-ionics [53].

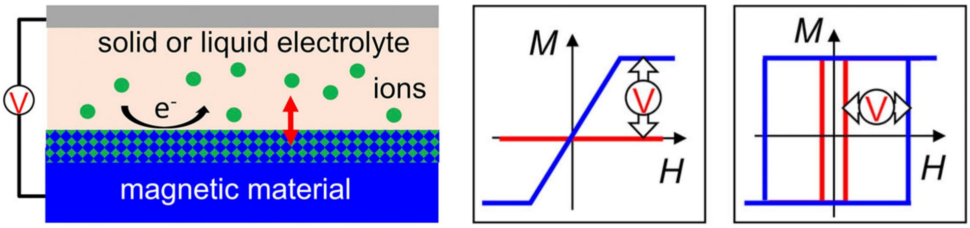

Figure 2.3: Schematic view of a magneto-ionic structure showing voltage-induced migration of ions in the electrolyte (left) leading to changes in the saturation magnetization (middle) and coercivity (right) of the magnetic material. Adapted from [53].

In order to migrate ions, solid-state ionic conductors must withstand applied voltages with minimal leakage current and must have a breakdown voltage above the threshold for ion migration. Leakage currents in solid electrolytes can be a limiting factor, They can be minimized, but requires controlled growth techniques and atmosphere [54] and an optimized device geometry with relatively small gate areas, patterned using micro/nanofabrication [55]. Liquid electrolyte gating is ruled by the electrochemical potentials of the chemical modifications that want to be induced, independently of the gated area. This facilitates the fabrication of the devices and provides a highly controllable way to characterize magneto-ionic effects to unravel the more fundamental aspects of the chemistry involved. In this thesis, a third approach has been used: a combination of a solid ionic conductor and an ionic liquid (IL). In this approach, a solid ionic conductor is used for ion mobility and an IL for generating high electric fields in which the ions in the IL do not participate in the magneto-ionic effects. Such an approach provides a better platform for characterizing the electric field effects before it can be transformed to a fully solid-state device. In the following, a detailed description of ionic liquids is introduced.

2.4 . Ionic liquid

An ionic liquid (IL) is a room-temperature molten salt consisting of anions and cations. ILs are ion conductors and electrically insulating and are used for high electrostatic charge carrier doping. High electric fields can be set up at the interface between an IL and and two electrodes on either side due to the ionic accumulation at both interfaces. A device geometry illustrating an IL under a positive voltage is shown in Figure 2.4. The device represents a planar capacitor with the capacitance given by $C = A\epsilon/d$, where A is the surface area covered by IL, ϵ is the dielectric permittivity of IL, and d is the distance between the ions and the counter charges in the electrode at the interface. d is determined by the size of the ions, which is estimated to be of the order of 1 nm [56], allowing for ultra-high capacitances and high electric fields up to 10 MV/cm [56] at the interfaces and the two layers of opposite charges are known as electric double layer (EDL).

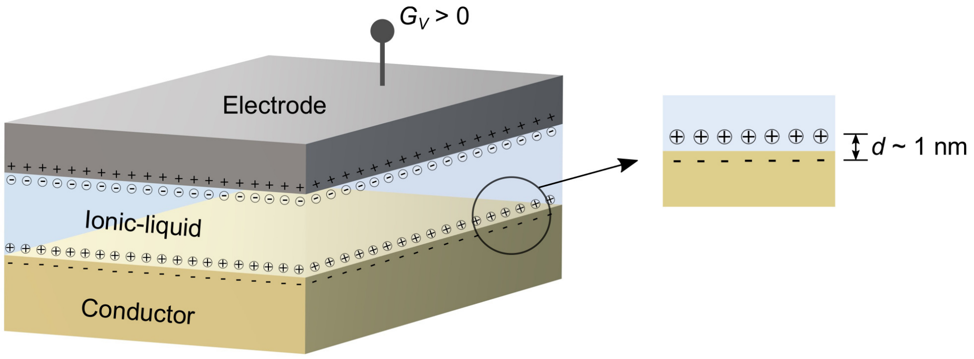

Figure 2.4: Schematic view of a device with an IL under a positive gate voltage (G_V>0) showing the rearrangement of cations and anions of the IL.

The specific capcitance of various ILs has been reported in the literature and the values fall in the range of 3-170 μF/cm^2 [56, 57] at low frequencies, which is four orders of magnitude higher than SiO_2. It should be noted that the EDL represented in Figure 2.4 depicts the basic operation of an IL and should not be confused with the real structure of an IL-EDL. In concentrated electrolytes, the first layer of ions delivers excess counter charge than the charge on the surface of the electrode, leading to what is known as overscreening [58]. This triggers the formation of a second layer of oppositely charged ions in order to screen the first layer, which often tends to overscreen, leading to the formation of multiple layers until electroneutrality is achieved. The overscreening structures typically form at low voltages and becomes smaller at high voltages by forming an additional layer of counter charges, often referred to as crowding [58]. A schematic representation of overscreening and crowding is shown in Figure 2.5.

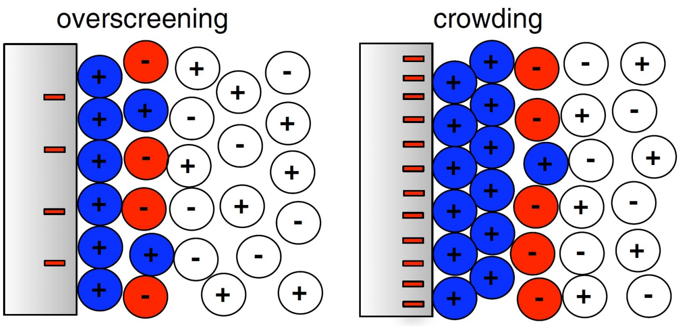

Figure 2.5: Structure of the ionic liquid electric double layer (in color) showing overscreening at moderate voltage and crowding at high voltage. Adapted from [59].

The operating voltage of an IL is determined by its electrochemical window and is typically around 5 V [60]. A remarkably high capacitance together with low toxicity, wide temperature and voltage window, and negligible volatility have made ILs a key tool in various applications in the fields of energy storage, spintronics, pharmaceuticals, biotechnology, sustainable energy, petrochemicals, and nuclear science [61]. Figure 2.6 shows the different classes of ILs based on their composition, namely aprotic, protic and zwitterionic, each with a specific application.

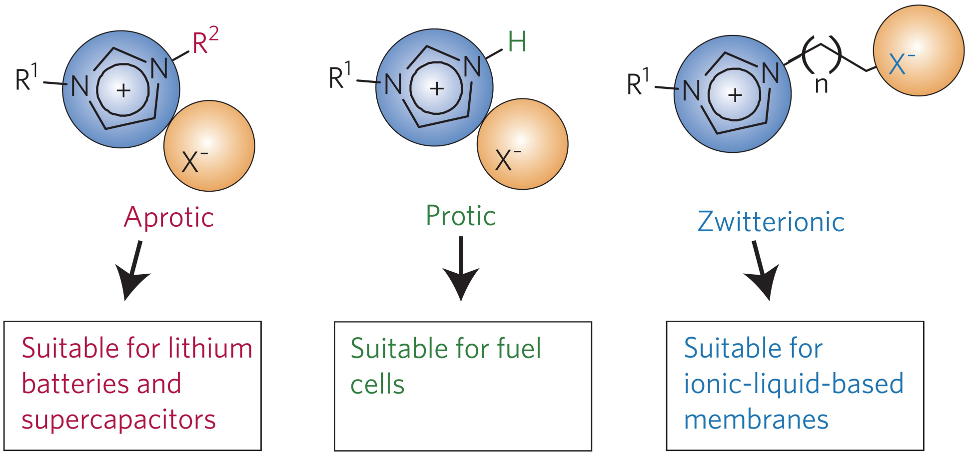

Figure 2.6: Various classes of ionic liquids based on their composition with a suitable application for each. 'R' is a non proton substituent. Adapted from [60].

2.4.1 . Structure and properties of ionic liquids

Ionic liquids are essentially composed of organic cations and anions of an average size of approximately 2 nm that are bound together by weak electrostatic interactions. The poor coordination between the ions allows a certain degree of movement that is accountable for the liquid state of ILs down to a temperature of approximately 220 K [62]. The possibility of introducing functionality on both anions and cations and their combinations theoretically enables 10^{18} different ILs [62] and the most commonly used ILs contain N-heterocyclic cations, for instance imidazolium salts. Figure 2.7 shows some of the common anions and cations used for ILs. It is worth mentioning that the melting point, viscosity, solubility, thermal and electrochemical stability, and liquid range of ILs can be tuned by tailoring a functional IL, for instance, by changing the substituents at the nitrogen atoms of the N-heterocyclic cations or by changing the type of anions.

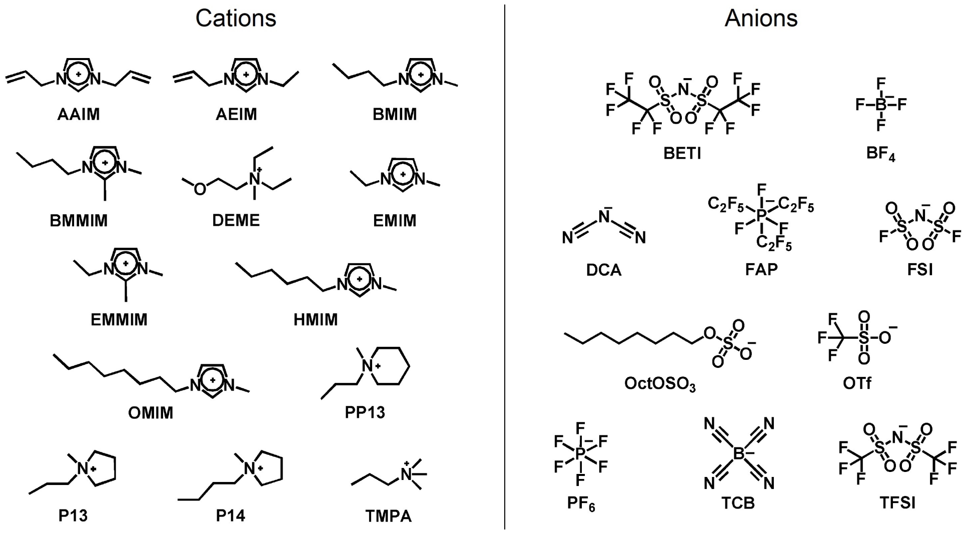

Figure 2.7: Molecular structures of the cations and anions of some of the common ionic liquids. Adapted from [63].

2.4.2 . [EMI][TFSI]

The IL used in this thesis to apply electric fields to manipulate magnetic properties is 1-Ethyl-3-methylimidazolium bis(trifluoromethylsulfonyl)imide, represented as [EMI][TFSI] or [EMIm][TFSI], in which the cation is $[\mathrm{EMI}]^+$ with a size of 0.156 nm^3 and the anion is $[\mathrm{TFSI}]^-$ with a size of 0.232 nm^3 [64]. It is worth mentioning that [EMI][TFSI] is just a means of gating and is not a source of ions that manipulate the magnetic properties via oxidation or reduction. The structural formula of [EMI][TFSI] is shown in Figure 2.8a. [EMI][TFSI] is a transparent IL with a density of 1.53 $\mathrm{g/cm}^3$ that has a freezing point of -16°C, and is thermally stable up to 400 °C [65]. The electrochemical window of [EMI][TFSI] has been reported to be larger than 4 V [66, 67] and the specific capacitance of [EMI][TFSI] reaches 11.4 $\mu\mathrm{F/cm}^2$ at 0.1 Hz, which decreases with increasing frequency [68] as shown in Figure 2.8b.

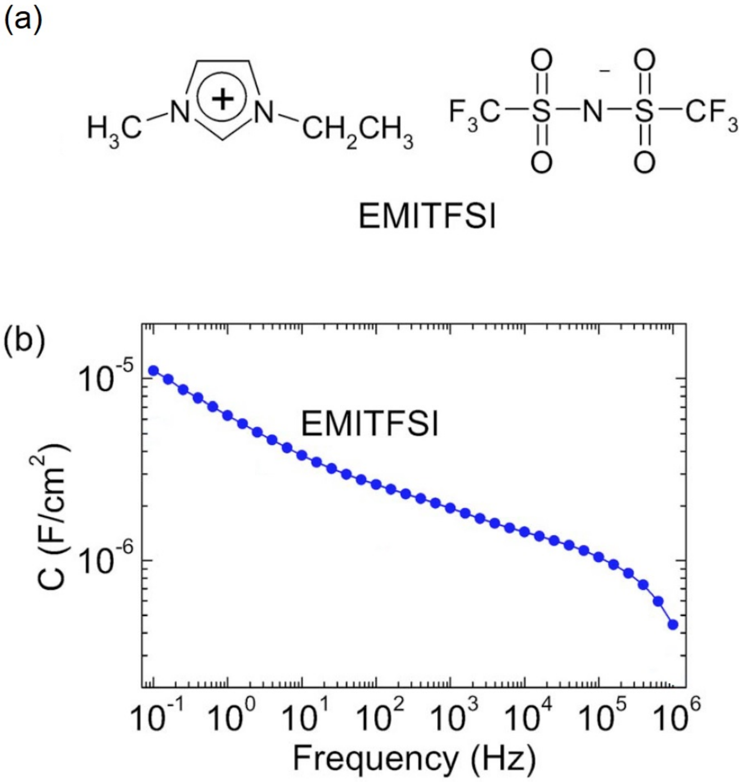

Figure 2.8: (a) Molecular structure of [EMI][TFSI], and (b) Capacitance of [EMI][TFSI] as a function of frequency measured using ac impedance technique. Adapted from [68].

2.5 . State of the art

As described in chapter 1, the interfacial magnetic anisotropy (IMA) plays a significant role in the development of spintronics devices. To manipulate IMA is to manipulate physical and chemical properties of nanoscale materials. It has been reported that the charge-based voltage control of magnetism can modify magnetic anisotropy with an efficiency in the range of 30-100 fJ/Vm [29,33,69]. However, for cache and main-memory applications, VCMA coefficients in the range of 200-500 fJ/Vm and 500-2000 fJ/Vm are sought, respectively [70]. Thanks to magneto-ionics, changes of magnetic anisotropy energy of up to 0.75 erg/cm^2 [38] with an efficiency of 11.6 pJ/Vm [55] has been demonstrated. In addition, magnetic properties such as saturation magnetization [38,55], coercivity [38,71], anisotropy [38], Dzyaloshinskii-Moriya interaction (DMI) [35], exchange bias [52,72,73], domain wall velocity [35,74], and Curie temperature [75] have been effectively controlled using magneto-ionics. In the following, some of the major advances in the field of magneto-ionics are outlined.

2.5.1 . Domain wall trap and interfacial magnetic anisotropy

One of the first examples of magneto-ionic control of magnetism is the demonstration of domain wall traps in Ta/Pt/Co/GdO$_x$ [36] as shown in Figure 2.9. In this system, a negative gate voltage was shown to change the coercivity in a non-volatile manner in the gated region. Since the electrode edge is the triple phase boundary where O_2 gas, Au (electron conducting phase) and O^{2-} ions from ion-conducting GdO$_x$ meet, under a negative gate voltage applied to the Au electrode, O^{2-} from GdO$_x$ migrate toward Co layer and and oxidize Co. This leads to a significant reduction in the magnetic energy density that is confined to a short length scale near the electrode perimeter trapping domain wall motion. With domain wall traps, non-volatile memory prototypes can be developed in which domain wall traps can facilitate electrical bit selection [36].

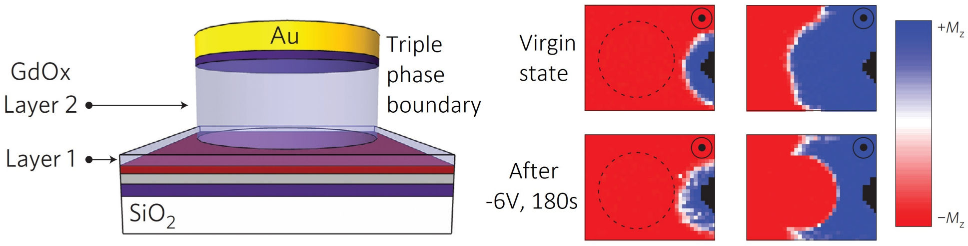

Figure 2.9: Schematic view of a Ta/Pt/Co/GdO$_x$ structure (left). MOKE maps showing the expansion of a domain under a driving field of 170 Oe in the virgin state and the blocking of domain expansion at the electrode edge after applying a gate voltage of -6V for 180s (right). Adapted from [36].

2.5.2 . Magneto-ionic modulation of Dzyaloshinskii-Moriya interaction

As described in chapter 1, spintronics devices based on domain wall motion have a great potential, for instance, 3D racetrack memories [76] could enable a high storage density device. The Dzyaloshinskii-Moriya interaction (DMI) is one of the key elements that can stabilize chiral magnetic structures such as Néel domain walls and skyrmions [44]. Hence, tuning DMI and domain wall dynamics in an energy-efficient and non-volatile manner is of great significance.

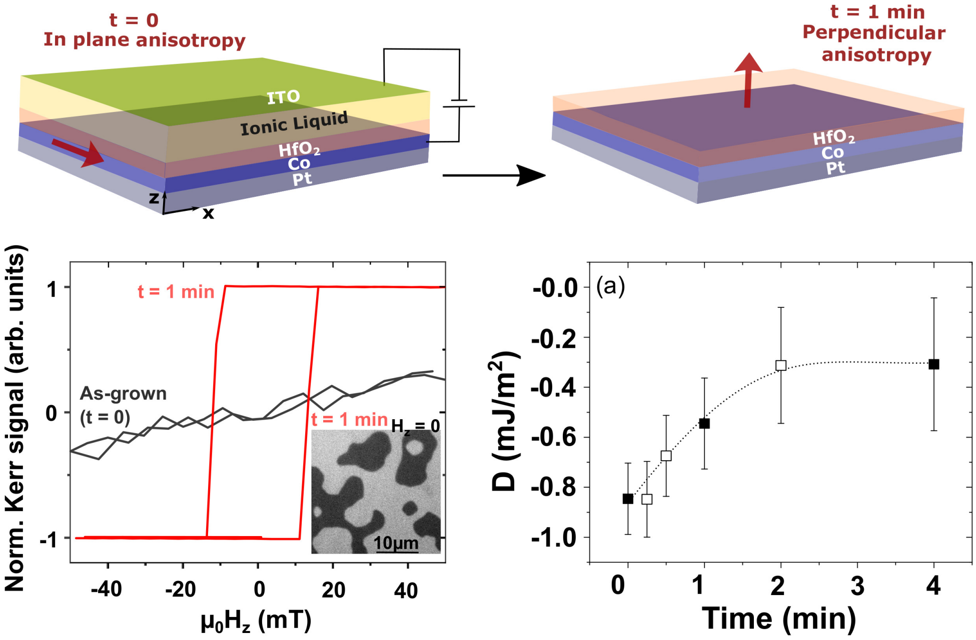

Figure 2.10: A schematic view of the ionic liquid-gated Pt/Co/HfO_2 structure showing a spin reorientation transition from in-plane magnetization easy axis to out-of-plane after applying a gate voltage of -3V for 60 s (on the top) and the corresponding MOKE hysteresis loops (bottom left). DMI constant D as a function of the gating time for a gate voltage of -3 V, showing a non-volatile reduction (bottom right). Adapted from [35].

In 2019, a study conducted on Pt/Co/HfO_2 [35] system with ionic liquid gating revealed large, nonvolatile changes in DMI that was also accompanied by a change in anisotropy from in-plane to PMA. As shown in Figure 2.10, an applied gate voltage of -3V decreases the value of DMI constant with the gate duration initially and plateaus out in the end, corresponding to a change of about 2.9 times the intial value. The proposed mechanism for such a change was the electric field-induced migration of oxygen species from HfO_2 and the subsequent decoupling between Pt and Co layers.

2.5.3 . Magneto-ionic reversal of skyrmion and domain wall chirality

Magnetic skyrmions are topological non-collinear spin textures that can be pictured as local whirlings of magnetization [46, 77, 78]. The size of skyrmions can be as small as a few nanometers and can behave like a particle that can be created, moved and annihilated [79]. In particular, it has been demonstrated that the current-driven motion of skyrmions only requires current densities that are five orders of magnitude lower than that required for domain wall motion [80]. This makes them a suitable candidate for the development of ultra-low energy spintronics devices such as the skyrmion racetrack memory [81, 82]. The dynamics of a skyrmion is determined by its chirality, clockwise (CW) or counterclockwise (CCW), and hence tailoring chirality is of great importance. Recently, in a Ta/FeCoB/TaO$_x$ system with ZrO$_2$ oxygen ion reservoir, a gate voltage-induced oxidation/reduction demonstrated reversal of skyrmion chirality; CW to CCW or CCW to CW. In addition, the authors also demonstrated a reversible control of domain wall chirality in a labyrinthine magnetic state [44]. This reversal in chirality was attributed to the gate voltage-induced inversion of the interfacial DMI sign as a negative interfacial DMI would stabilize a CW skyrmion and a positive interfacial DMI would stabilize a CCW skyrmion. An illustration of the device structure and skyrmionic motion under an in-plane current density is shown in Figure 2.11.

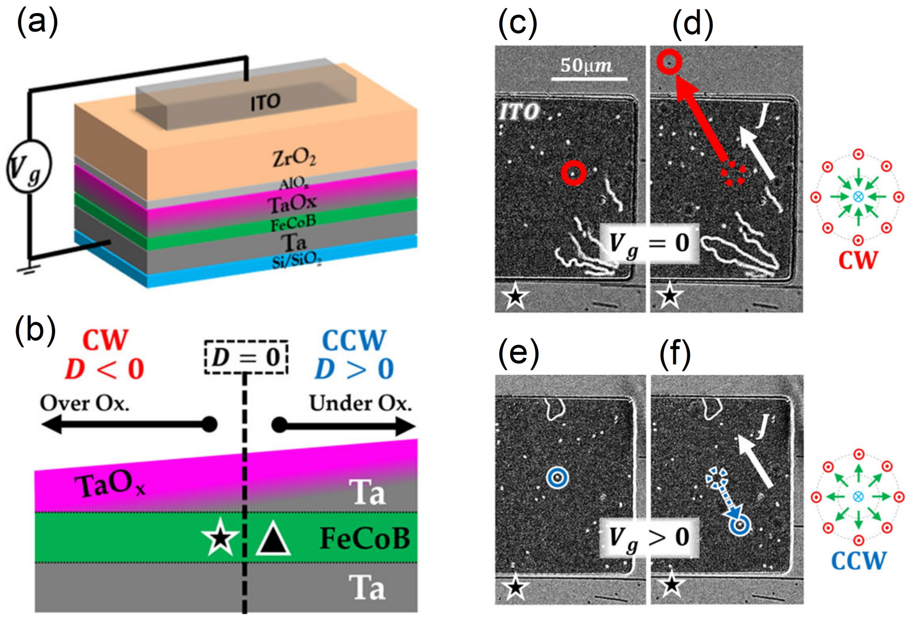

Figure 2.11: A schematic view of the Ta/FeCoB/TaO$_x$/ZrO$_2$/ITO device structure (a) showing a change in the chirality and DMI constant with the oxidation gradient of Ta wedge on FeCoB (b). Polar MOKE microscope images of current induced motion and direction of a skyrmion for an in-plane current density J 5 x 10^9 A/m^2 before applying a gate voltage (c), (d) and after applying a gate voltage of +3.5 V (e), (f) showing a reversal in the direction of skyrmion motion. Adapted from [44].

2.5.4 . Magneto-ionic control of ferrimagnetism

Ferrimagnets are magnetic materials with magnetic sublattice moments aligned antiparallel, resulting in a finite magnetization [83]. The magnetization of a ferrimagnet can be changed by varying the temperature or chemical composition, and in some cases, zero net magnetization state (also known as compensation state) can be achieved [84]. Compensated ferrimagnets are an interesting class of magnets as they combine the advantages of both ferromagnets and antiferromagnets [83]. With ferrimagnets, fast spin dynamics [85–87], ultra-fast optical switching [88], and room temperature-stable skyrmions [85] have been demonstrated. In addition, ferrimagnets can allow for 180° switching due to the differences in magnetic sublattice moments, making them interesting for technological applications.

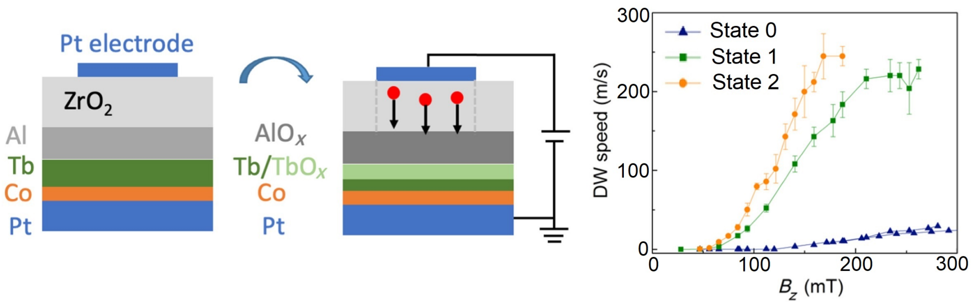

Figure 2.12: A schematic view of the Pt/Co/Tb/Al/ZrO_2/Pt structure showing a negative gate voltage-induced oxidation of Al and Tb (left). Domain wall velocity as a function of out-of-plane field for the virgin sample (state 0), samples after applying -8 V for 430 s (state 1) and -10 V for 600 s (state 2) (right). Adapted from [74].

In a recent study, magneto-ionic effects in a Pt/Co/Tb/AlO_x ferrimagnetic stack with ZrO_2 oxygen ion reservoir showed a large reversible variation in domain wall velocity from 10 m/s in the as-grown state to 250 m/s after gating [74]. Co/Tb is a ferrimagnetic structure as the magnetic moment acquired in Tb is antiparallel to Co, causing a reduction in the effective magnetization. Hence, the proposed mechanism for such a large change in domain velocity was the significant changes in magnetization, anistropy and DMI caused by the voltage-induced oxidation of Tb. A schematic of the structure of the device and the domain wall velocity before and after applying a gate voltage is shown in Figure 2.12.

2.5.5 . Magneto-ionic control of synthetic antiferromagnets

A synthetic antiferromagnet (SAF) is a multilayered-structure of two ferromagnets adjacent to a non-magnetic metallic spacer that are antiferromagnetically coupled via Ruderman-Kittel-Kasuya-Yosida (RKKY) interaction [89,90]. SAFs are an important class of magnetic structures that are used in magnetic sensors [91], MRAMs [92], and nano-oscillators [93]. In addition, with SAFs, an efficient and fast domain wall motion that can exceed 750 m/s have been demonstrated [94], making them an interesting candidate for racetrack memories.

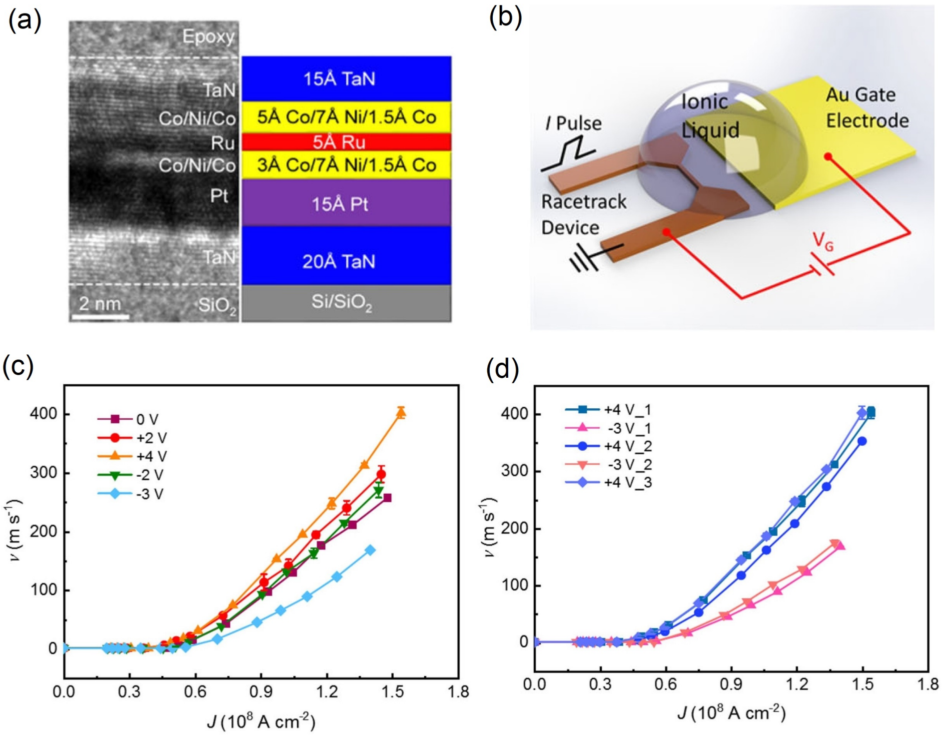

Figure 2.13: (a) Cross-sectional transmission electron micrograph and a schematic view of the TaN/Pt/Co/Ni/Co/Ru/Co/Ni/Co/TaN structure and (b) the device geometry with ionic liquid gating. Domain wall velocity as a function of current density (J) pulses (c) for different gate voltages and (d) showing reversible modulation of domain wall velocity by changing the gate voltage between -3 V and +4 V for 30 minutes each. Adapted from [95].

In a recent study on TaN/Pt/Co/Ni/Co/Ru/Co/Ni/Co/TaN SAF [95], where the FMs Co/Ni/Co are antiferromagnetically coupled through Ru, nonvolatile, reversible changes in current-induced domain wall velocities by several hundred m/s has been demonstrated using ionic liquid gating. In SAF structures, current-induced domain wall motion is predominantly mediated by a novel torque, known as exchange coupling torque, generated by the antiferromagnetic exchange coupling field. The strength of the exchange coupling torque is about an order of magnitude larger than the torque induced by the DMI field in ferromagnetic structures [94,96] and is directly proportional to the strength of the antiferromagnetic exchange coupling between the two magnetic layers. Hence, the large changes in domain wall velocity observed in [95] were attributed to large (over 95%) oxidation of the top magnetic layer via gate voltages that effectively converted the SAF structure to a FM structure largely reducing the exchange coupling torque. A schematic structure of the stack and device, and the changes in domain wall velocities induced by gate voltages are shown in Figure 2.13.

2.5.6 . Magneto-ionic control of spin-orbit torque

As introduced in chapter 1, MRAMs based on spin-orbit torque (SOT) have a great potential as they offer high speed switching and endurance by separating write and read paths. In a heavy metal (HM)/ferromagnet (FM) structure, when a charge current is passed through the HM layer, a spin accumulation at the HM/FM interface is generated by spin Hall effect in the bulk of the HM or/and at the interface by Rashba effect [97, 98]. The direction of spin accumulation determines the direction of switching in an SOT-MRAM, skyrmion motion, and domain wall motion. Hence, it is of great importance to be able to control the direction and amount of spin accumulation to design SOT devices. With the progress in magneto-ionics, voltage induced migration of oxygen ions in a Pt/Co/GdOx system has reported a reversible, non-volatile changes in both the amount and the direction of the current-induced spin accumulation [99] for SOT. The observed changes were attributed to the voltage-induced oxidation/reduction of the Pt/Co interface that modifies the strength and polarity of the Rashba SOT, which is opposite to that of SHE-based SOT, favoring the change in SOT polarity [99]. A schematic of the stack showing the changes in spin accumulation direction and a plot of longitudinal SOT effective field (H_L) under gate voltages are shown in Figure 2.14.

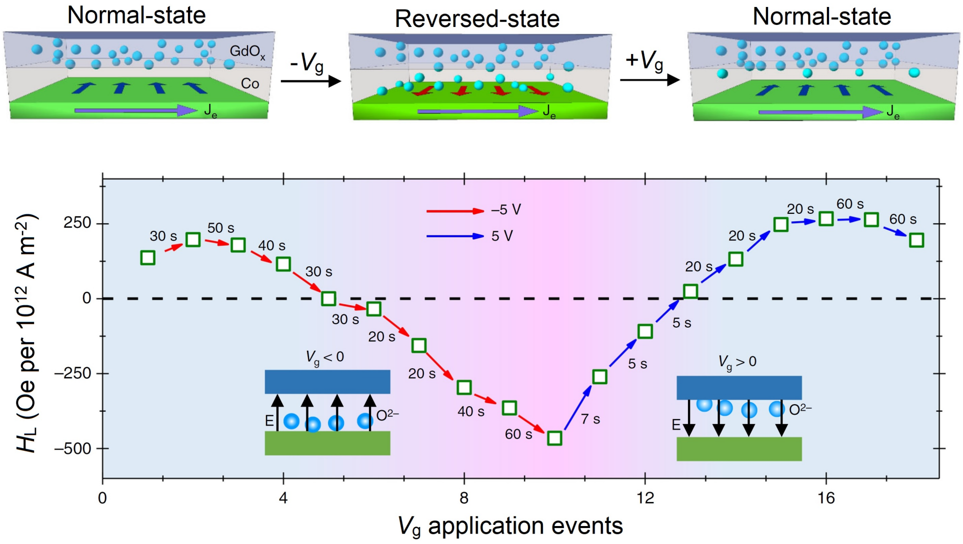

Figure 2.14: A schematic view of a Pt/Co/GdO$_\mathrm{x}$ structure showing a negative gate (-V_g) voltage-induced migration of oxygen ions toward Co causing a reversal of the spin accumulation direction, which, after applying a positive gate (+V_g) recovers the initial state as the oxygen ions migrate away from Co (on the top). Evolution of the longitudinal SOT effective field (H_L) demonstrating the SOT sign reversal from the intial state (normal-state) after applying a negative gate voltage of -5 V for different durations and recovery of the normal-state after applying a positive gate voltage of +5 V for different durations. Adapted from [99].

2.5.7 . Magneto-ionics with different types of ions

It may be noted that the above studies make use of oxygen ion in solid-state devices; however, with the advances in solid and liquid gating, magneto-ionic effects, in addition to oxygen ions, using hydrogen [50, 100], lithium [101–103], fluoride [104], and nitrogen [105] ions have been reported. In the following, magneto-ionics using different types of ions is outlined.

Hydrogen ions

A proton-based route [50, 100] has been developed in solid-state heterostructures, which has demonstrated a switch speed between PMA and in-plane magnetic anisotropy of down to 1 ms [50] for more than 1000 cycles at room temperature, which is significantly faster than in oxygen-based magneto-ionics [35, 38, 71]. In these systems, protons are generated by hydrolysis of atmospheric H_2O at the top electrode and are driven toward the ferromagnet through a solid-oxide electrolyte by applying a gate voltage. The first proton-induced magneto-ionic effects were demonstrated in a Ta/Pt/Co/GdO_x/Au heterostructure [100]. A schematic of the device and the electrochemical reactions are shown in Figure 2.15.

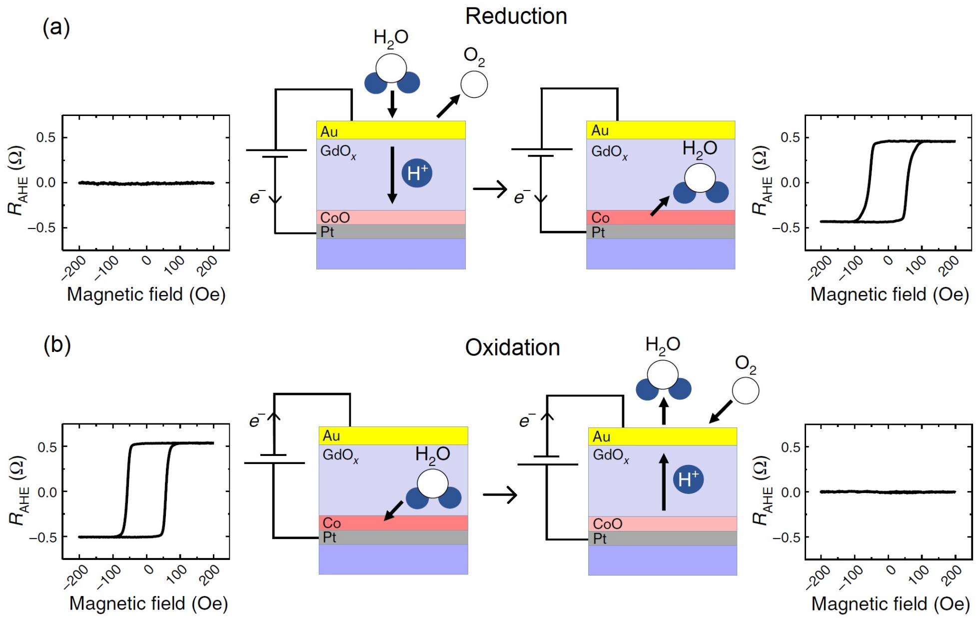

$$\text{Anode (Au)}: \quad 2H_2O \rightarrow 4H^+ + O_2 + 4e^-$$

$$\text{Cathode (Pt)}: \quad 4H^+ + 2Co^{2+} + 2O^{2-} + 4e^- \rightarrow 2H_2O + 2Co$$

Figure 2.15: (a) A schematic view of the reduction process of CoO at the Co/GdO_x interface in Pt/Co/GdO_x/Au structure to Co showing the electrolysis of H_2O and migration of H^+ under a positive gate voltage with the corresponding AHE hysteresis loops. (b) Oxidation of Co to CoO showing the formation of H_2O under a negative gate voltage and the corresponding AHE hysteresis loops, and the electrochemical reactions involved at the anode (Au) and cathode (Pt). Adapted from [100].

As described in section 2.5.4, ferrimagnets can allow for 180° switching that are of great interest in developing spintronics devices. However, an energy-efficient 180° magnetization switching in ferrimagnets is one of the key challenges. Recently, in a GdCo ferrimagnetic alloy, voltage-induced hydrogen loading/ unloading showed a change in the compensation temperature greater than 100 K, allowing for a reversible toggle between Gd or Co dominant sublattices (dominant magnetization) [106]. In addition, using appropriate biasing layers (exchange-biasing NiO layer or stray field biasing layer-L1$_0$-FePd with bulk PMA), the authors also demonstrated a 180° reversal of either the the Néel vector or the net magnetization without external magnetic fields. The proposed mechanism for this result was the weakening of antiferromagnetic exchange coupling upon hydrogenation, causing a reduction in the magnetization of Gd more than that of Co. Figure 2.16 shows a transmission electron microscopy image of the stack and the hysteresis loops of the stack showing the change in ferrimagnetic ordering and the compensation temperature before and after gating.

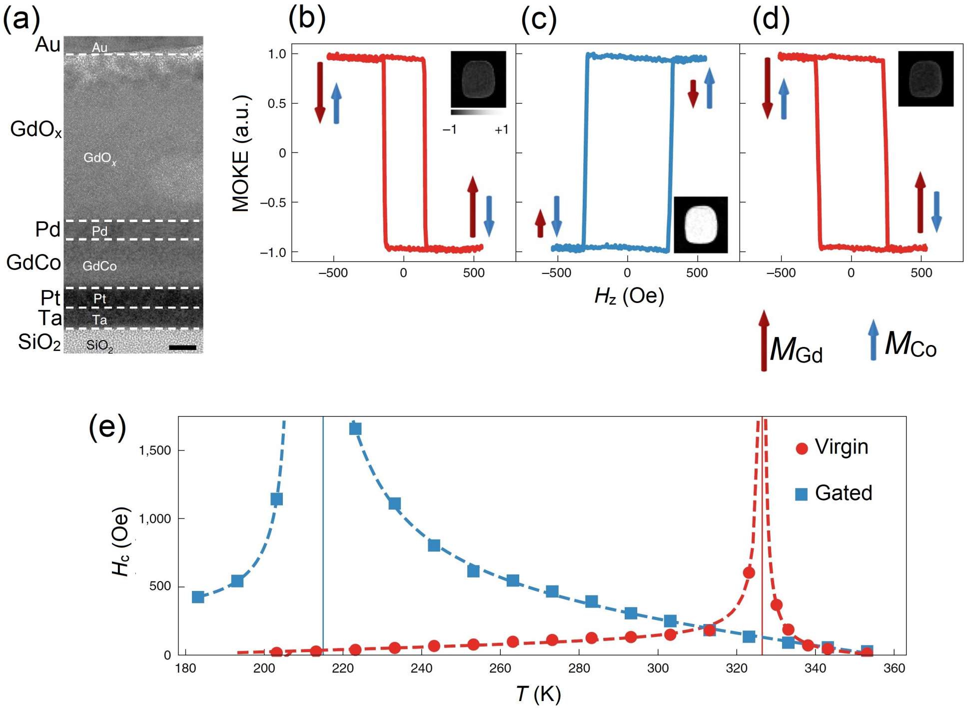

Figure 2.16: (a) Cross-sectional transmission electron micrograph of the Ta/Pt/GdCo/Pd/GdO$_x$/Au stack. MOKE hysteresis loops of the device: (b) virgin state, (c) after applying a gate voltage of +2.5 V for 180 s (d) and subsequent application of -0.5 V for 30 s. The arrows indicate the ferrimagnetic alignment of the Gd (red) and Co (blue) magnetization. (f) Coercivity as a function of temperature before and after applying a gate voltage of +2.5 V for 180 s showing a change in compensation temperature induced by hydrogen gating. Adapted from [106].

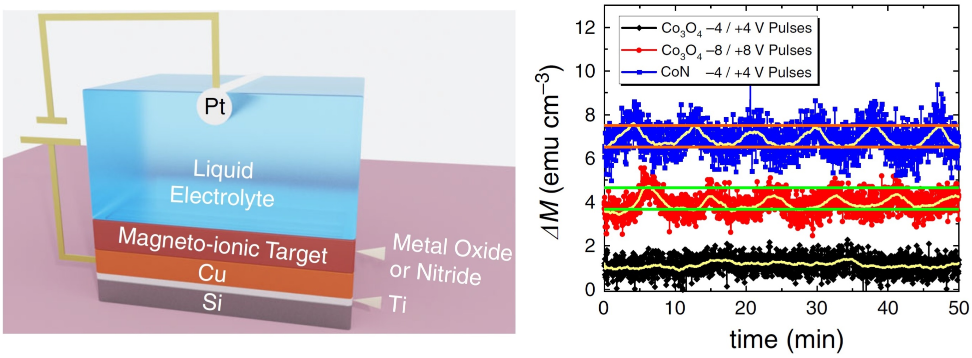

Figure 2.17: Schematic view of the sample structure showing the electrolytic gating of Co_3O_4 (on the left). Magneto-ionic cycling of the magnetization of Co_3O_4 film (black and red curves) with -4 V/+4 V and -8 V/+8 V, and CoN film (blue curve) with -4 V/+4 V. The duration of the gate voltages per cycle is 8.5 minutes. Adapted from [105].

Nitrogen ions

Magneto-ionic effects using nitrogen ions was first reported in a CoN system [105]. In this study, a magneto-ionic performance comparison between an oxygen-driven system and a nitrogen-driven system using a liquid electrolyte gate at room temperature is reported. The films used were relatively-thick (85 nm) films of Co_3O_4 for oxygen and CoN for nitrogen ions. The authors showed a reversible change in saturation magnetization (M_S) of 1 emu/cc in both systems and show that a gate voltage of ± 4 V for 4.1 minutes is required for CoN, whereas a gate voltage of ± 8 V for 6.2 minutes is required for Co_3O_4. This disparity between the magneto-ionic performances of CoN and Co_3O_4 has been attributed to the lower electronegativity and activation energy for ion diffusion of nitrogen compared to oxygen. A schematic of the device and reversible cycles of Co_3O_4 and CoN is shown in Figure 2.17.

Lithium and fluoride ions

Magneto-ionics using lithium and fluoride ions has paved a new route to integrate rechargeable batteries and magnetism in addition to large changes in magnetic properties [101–104]. With lithium ions, an ON/OFF switching of ferromagnetism with antiferromagnetic hematite (αFe_2O_3) and paramagnetic iron selenide ($FeSe_2$) using a liquid electrolyte gate, and a reversible change of 27% in the M_s of CoFeB [103] in a solid electrolyte system have been reported. In addition, lithiation/delithiation process in a magneto-ionic cathode in a lithium-ion battery has demonstrated a fast and reliable in-built sensor that can monitor the state of charge [102]. Moreover, with fluoride ion (de)intercalation, a reversible change in magnetization of 67% in $La_{2-2x}Sr_{1+2x}Mn_2O_7$ with a low operating voltage of <1 V in an all-solid-state system [104] has been reported. Figure 2.18 shows the ferromagnetic switching of antiferromagnetic hematite, αFe_2O_3 to ferromagnetic Fe, reversible conversion to FeO in the subsequent voltage cycles and the corre-

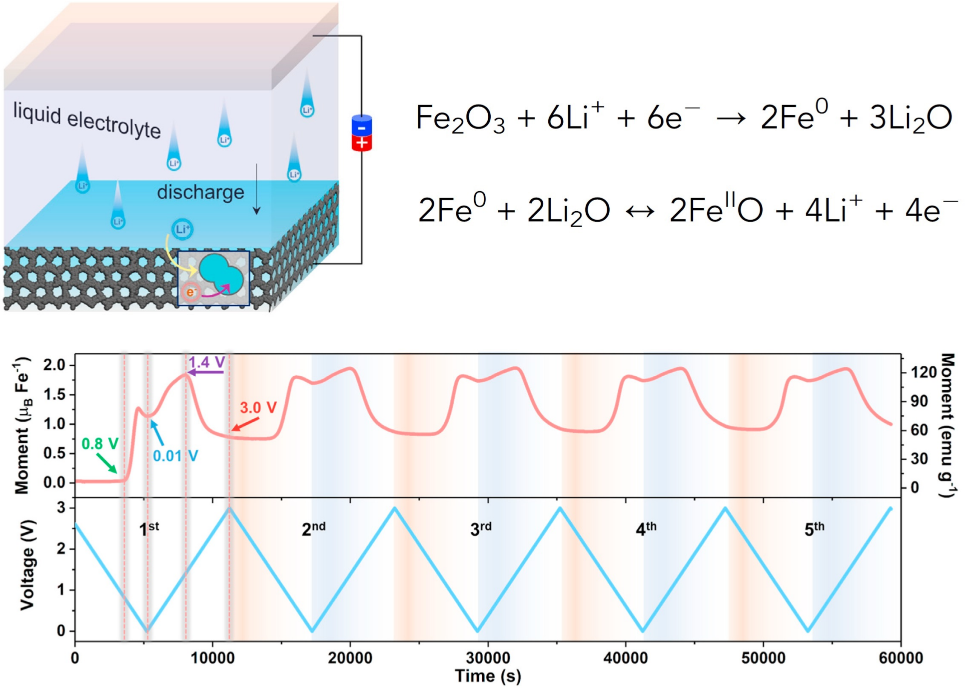

$$Fe_2O_3 + 6Li^+ + 6e^- \rightarrow 2Fe^0 + 3Li_2O$$

$$2Fe^0 + 2Li_2O \leftrightarrow 2Fe^{II}O + 4Li^+ + 4e^-$$

Figure 2.18: A schematic view of the α-Fe_2O_3 electrochemical cell showing the migration of lithium ions (Li^+) under a gate voltage with the corresponding reduction/oxidation electrochemical reactions (on the top). The reversible cycling of the magnetic moment and the corresponding gate voltage and duration (on the bottom). Adapted from [101].

sponding electrochemical reactions with lithium ions.

3 - METHODOLOGY

In this chapter, the different methods that were used to obtain the results presented in this thesis are discussed. The chapter begins with an introduction on the sample preparation techniques that include magnetron sputtering and, X-ray diffraction (XRD). In the second part, the measurement methods are presented: anomalous Hall effect, magneto-optical Kerr effect (MOKE), vibrating sample magnetometry (VSM), Brillouin light-scattering spectroscopy, and X-ray photoelectron spectroscopy (XPS).

3.1 . Sample preparation

3.1.1 . Magnetron sputtering

The samples used in this thesis are thin films grown by magnetron sputter deposition. Sputtering is a physical vapor deposition method in which an inert gas (in this case, argon (Ar)) is ionised by high voltage and then is accelerated toward the target material, causing an ejection of atoms from the target material that subsequently condenses on a substrate to form a thin film. The deposition is performed in an ultra-high vacuum chamber with a typical base pressure of 10^{-8} mbar to prevent contamination. A schematic overview of the sputtering process is shown in Figure 3.1. First, a clean substrate (in this case, Si/SiO_2) is loaded into the load-lock and is then transferred into the sputter chamber. To start the process, Ar gas is flowed in the sputter chamber, which raises the pressure to 10^{-2} mbar. Subsequently, a high voltage is applied (power equivalent of 100-950 W, depending on the target) between the target (cathode) and an anode ring. The high voltage ionizes Ar gas into Ar^+ ions that are accelerated toward the target kept at a negative voltage. When the Ar^+ ions bombard the target, momentum is transferred from the high energy Ar^+ ions to the target, causing the ejection of the target atoms that subsequently adhere to the substrate to form a film. To increase the sputter rate, the cathode voltage and the working pressure of Ar may be increased, but this causes large heat generation. Therefore, to keep high sputter rates and to reduce high voltage, magnetron sputtering is used in which a strong magnet that can withstand high temperatures is placed behind the target. The stray field of the magnet confines the secondary electrons produced from the bombardment of the target with Ar^+ ions near the target surface that enhances the ionization of Ar, allowing for the process to be carried out at lower working pressures and voltages.

Magnetron sputtering can be powered by several types of power supplies such as

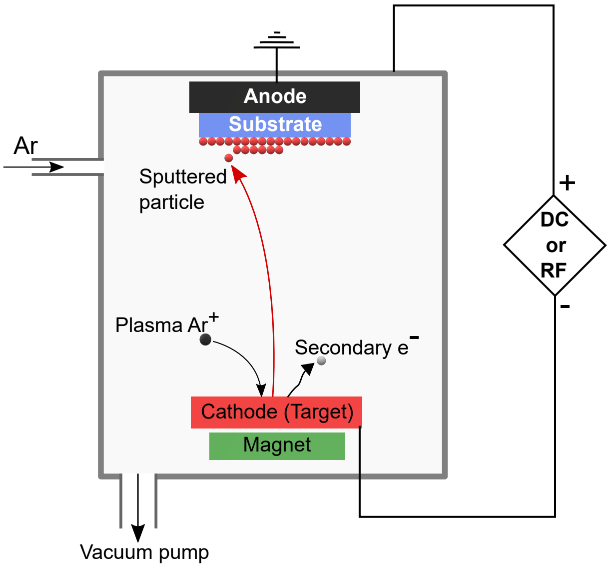

Figure 3.1: Schematic view of the magnetron sputtering process showing the bombardment of Ar^+ with the target and the subsequent deposition of the target atoms on the substrate.

direct current (DC), radio frequency (RF), pulsed DC, mid frequency AC (MFAC), and high power impulse magnetron sputtering (HiPIMS). In this thesis, DC and RF power sources are used. DC magnetron sputtering is used for depositing metals and RF sputtering is used for depositing oxides to prevent charge build-up on the oxide surfaces.

The thin films used in this thesis were magnetron sputtered and were deposited by Maria-Andromachi Syskaki at Singulus Technologies.

3.1.2 . X-ray diffraction

X-ray diffraction is a widely used technique to characterize the structural properties of a material. The technique is based on the interference between the X-rays and the crystallographic planes of a material separated by a distance comparable to the wavelength of the X-rays. X-ray diffraction in crystals was discovered by Max von Laue in 1912 [107].

When an incident X-ray hits the sample at an angle θ with respect to the involved crystallographic plane, it constructively interferes or diffracts if the following condition (known as Bragg's condition) is satisfied:

$$2dsin(\theta) = n\lambda, \tag{3.1}$$

where d is the interplanar distance of the involved crystallographic plane, n is the diffraction, and λ is the wavelength of the X-ray. XRD can be performed

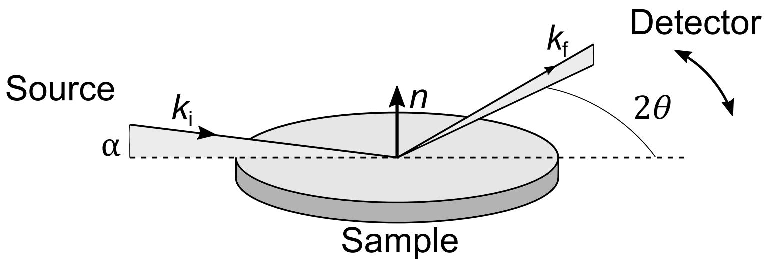

Figure 3.2: An illustration of the GIXRD geometry showing an incident X-ray with a wavevector k_i, which scatters into k_f on the sample surface with the surface normal n and the motion of the detector.

in different geometries such as Bragg-Brentano (θ-2θ), grazing incidence and ϕ scans. The XRD patterns presented in this thesis were performed in the non-coplanar grazing incidence X-ray diffraction (GIXRD) geometry. This geometry reduces the penetration depth of the X-rays, preventing strong signals from the substrate and improves the signal-to-noise ratio for thin films. In GIXRD, the X-ray source and the sample are fixed such that the incident beam hits the sample at a very low incidence angle α (0.4° in our case) and the detector moves at an in-plane angle 2θ to collect the diffracted beams. A schematic of the GIXRD geometry showing the diffraction of an incident X-ray is illustrated in Figure 3.2.

The XRD measurements presented in this thesis were performed at C2N with the help of Ludovic Largeau. The measurements were obtained using a SmartLab diffractometer (Rigaku) using a scintillation point detector. The diffractometer was equipped with a Cu rotating anode at 45kV and 200 mA, a five circle goniometer, and a double tilt sample holder.

3.2 . Measurement methods

3.2.1 . Anomalous Hall effect

The anomalous Hall effect (AHE) is a magneto-transport method and one of the main experimental methods used in this thesis to measure the magnetic hysteresis loops of ferromagnetic thin films. In the ordinary Hall effect, an accumulation of charges or a potential difference (Hall voltage) is generated in a nonmagnetic conductor transverse to an electric current and applied magnetic field due to the Lorentz force. However, there is no net spin accumulation as the number of spin up and spin down cancel each other. The anomalous Hall effect on the other hand is the result of spin-dependent deflection of electrons in a magnetic conducting material that generates both a spin accumulation and a Hall voltage. In the case of an out-of-plane magnetized film in an external magnetic field H_z, the measured Hall voltage V_{H} can be expressed as

$$V_{\mathrm{H}} = R_{\mathrm{OHE}} I \mu_0 H_z + R_{\mathrm{AHE}} I \mu_0 M_z, \tag{3.2}$$

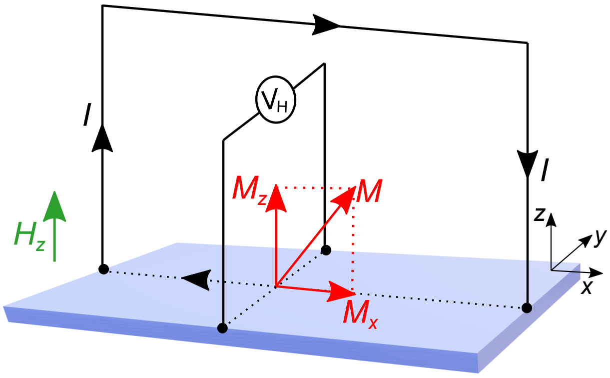

Figure 3.3: Schematic view of the AHE measurement system.

where R_{OHE} and R_{AHE} are the ordinary Hall coefficient and anomalous Hall coefficient, respectively. In magnetic materials, R_{AHE} is usually much larger than R_{OHE}. The first term on the right hand side of the equation represents the ordinary Hall voltage that scales with the out-of-plane component of the applied magnetic field. The second term corresponds to the anomalous Hall voltage that scales with the out-of-plane component of the magnetization M_z. A schematic view of the AHE measurement system is shown in Figure 3.3.

The anomalous Hall effect is a quantum phenomenon that originates from quantum coherent band mixing effects by the external electric field and the disorder potential [108]. The microscopic origin of the AHE is still not fully comprehended. The current understanding of the AHE includes three distinct contributions: intrinsic, skew-scattering, and side-jump contributions. An illustration of these contributions is shown in Figure 3.4. For a detailed review and understanding of the AHE, the reader is referred to Ref. [108].

3.2.2 . Magneto-optical Kerr effect

Magneto-optical effects refer to the phenomena in which when an electromagnetic wave interacts with a magnetic medium, its properties are altered. One of the common magneto-optical effects is the Faraday effect, discovered by Michael Faraday in 1845 [109]. In the Faraday effect, when a linearly polarized light propagates through a transparent medium placed in a magnetic field aligned along the direction of the propagation, the polarization axis of the light rotates. Similar to the Faraday effect, when a linearly polarized light reflects from a magnetic material, the polarization axis rotates and gains a certain ellipticity. This effect is known as the magneto-optical Kerr effect, or MOKE, discovered in 1877 by John Kerr [110].

Linearly polarized light is a linear combination of left and right circularly polar-

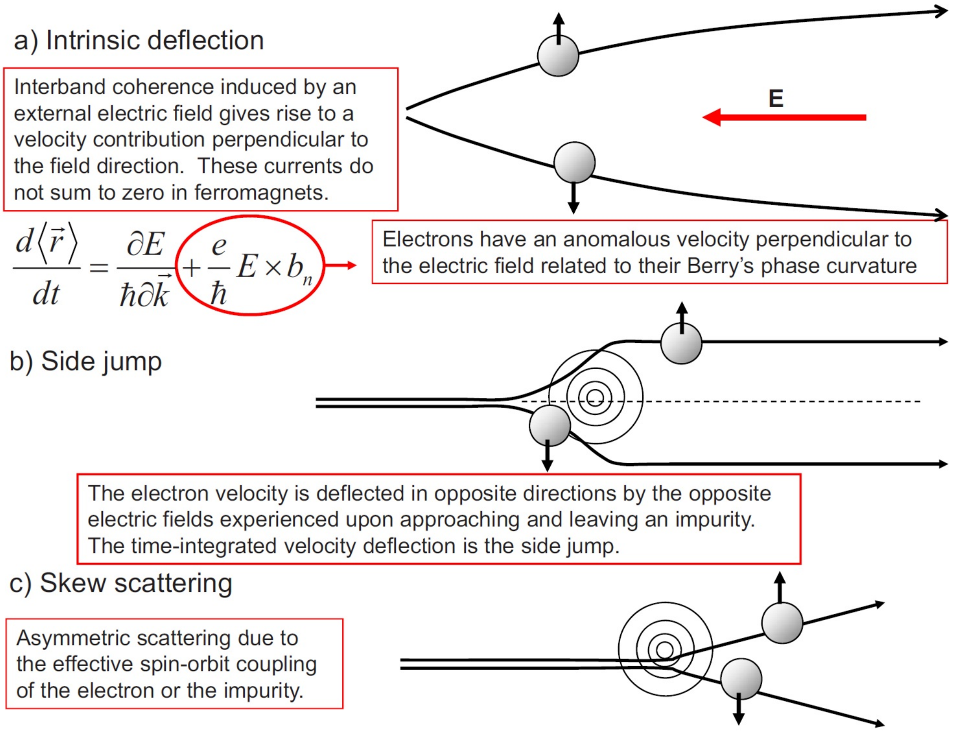

Figure 3.4: An illustration of the three main contributions of the AHE: (a) Intrinsic, (b) Side-jump, and (c) Skew-scattering (adapted from [108]).

ized light and these two modes must be in phase relative to each other. When the velocity of each mode in a medium depends on the direction of propagation, the medium is called anisotropic and the corresponding dielectric constant becomes a 3 x 3 tensor. The dielectric tensor ($\bar{\epsilon}$) can be symmetric, antisymmetric or a combination of both. If the values in the symmetric part of the tensor are identical, the medium is isotropic. For a magnetic sample with spontaneous magnetization M, the dielectric tensor is [111]:

$$\bar{\epsilon} = \epsilon \begin{bmatrix} 1 & iQ_z & -iQ_y \\ -iQ_z & 1 & iQ_x \\ iQ_y & -iQ_x & 1 \end{bmatrix}, \tag{3.3}$$

where $N = \sqrt{\epsilon}$ is the refractive index of the nonmagnetized medium, and Q is the Voigt magneto-optical parameter that is proportional to the magnetization M of the medium. When a linearly polarized light enters the medium, typically a penetration depth of 10-20 nm for metals, the left and right circularly polarized modes experience different refractive indices [112] n, $n = N(1 \pm Q.\vec{k})$. Since left and right circularly polarized modes have different refractive indices, they propagate at different velocities given by:

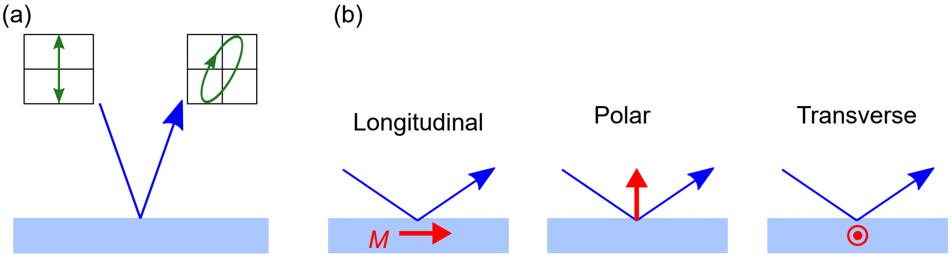

Figure 3.5: (a) Illustration of the magneto-optical Kerr effect (MOKE) showing a rotation of the polarization axis and a change in the ellipticity of the incident linearly polarized light after reflection. (b) Different MOKE configurations: Longitudinal, Polar, and Transverse.

$$c = \frac{1}{\sqrt{\mu_r \epsilon_r}} c_0 = \frac{c_0}{n}, \tag{3.4}$$

where c, and c_0 are the speeds of light in the medium and vacuum, respectively and μ_r is the relative permeability. When the light is reflected from the surface of the medium, the two modes that are at different velocities and phase shift recombine resulting in a rotation of the polarization axis with respect to the incoming light and a change in the ellipticity. The rotation of polarization axis is called Kerr rotation θ and the change in ellipticity is Kerr ellipticity ϕ.

There are three major configurations of MOKE: longitudinal, polar and transverse, which are shown in Figure 3.5. The different configurations are defined by the orientation of the magnetization with respect to the surface of the sample and the plane of incidence of the light. In the longitudinal configuration, the magnetization is aligned parallel to both the sample surface and the plane of incidence. In the polar configuration, the magnetization is perpendicular to the sample surface and parallel to the plane of incidence, and in the transverse configuration, the magnetization is parallel to the sample surface and perpendicular to the plane of incidence. The magnetic hysteresis loops presented in this thesis was generated using a Kerr microscope in the polar MOKE configuration, which is discussed in the following section.

3.2.3 . Kerr microscopy

A Kerr microscope is an optical microscope that uses the MOKE, making it sensitive to the Kerr rotation or ellipticity of the sample to obtain an image with magneto-optical contrast. Kerr microscopy is a powerful tool and can be used for studying magnetization dynamics on a timescale of approximately 100 ms. A schematic view of the Kerr microscope with the path of light propagating toward the sample and the reflected path of light for the image-formation is shown in Figure 3.6. A red light-emitting diode (LED) with 630 nm wavelength light source was used to illuminate the sample. The light is guided through the apertures and a

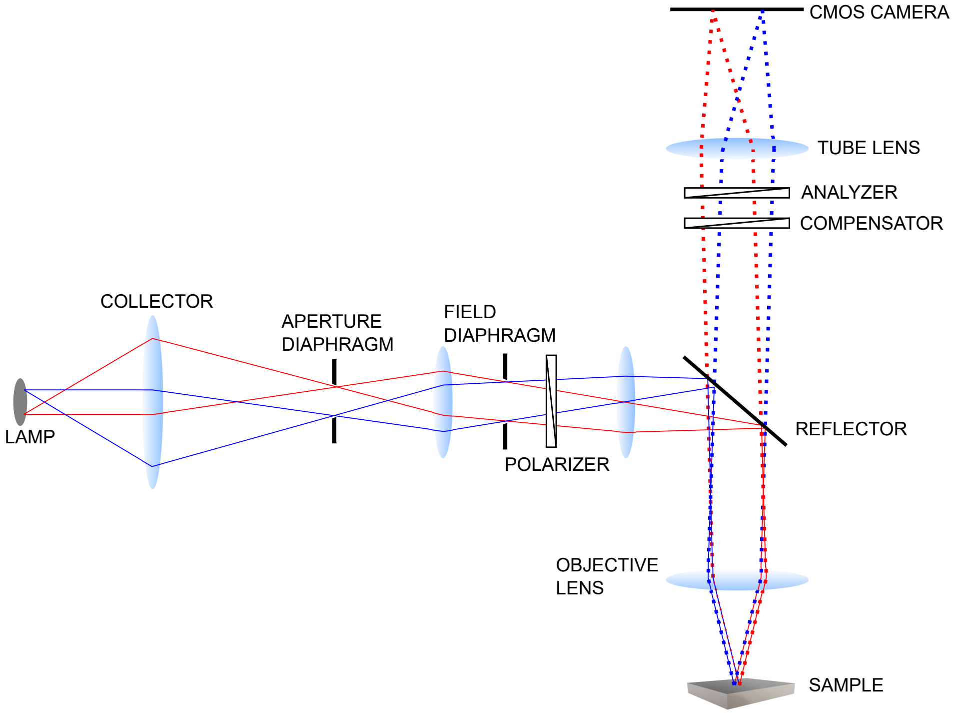

Figure 3.6: A schematic of the Kerr microscope showing the path of light propagating toward the sample (solid blue and red lines) and the image-forming lightpath (dotted blue and red lines).

polarizer and is focused on the sample by the objective lens. The light incident on the sample is perpendicular to the sample surface, making it sensitive to the out-of-plane magnetization component of the magnetization. The light then reflects from the sample surface and is passed through the analyzer, which is nearly crossed with the polarizer to attenuate the polarization state of the original incident light. A compensator allows to optimize the magnetic signal, which is convenient when the ellipticity is larger than the Kerr roatation. The intensity of the light that depends on the magnetization is measured by a CMOS camera.

The magnetic hysteresis loops presented in this thesis were generated by analyzing the grey scale images with magneto-optical contrast obtained using the camera. The images at saturation magnetic fields are either bright or dark, corresponding to the alignment of magnetic domains, and are normalized as ±1. The images of the intermediate magnetic states are either a combination of dark and bright regions (for square hystereses) or shades of grey and are normalized as the ratio between dark and bright regions or the level of darkness or brightness of the image. A hysteresis loop of W/CoFeB/HfO_2 annealed at 390°C for 1 hour demonstrating the grey scale corresponding to the magneto-optical contrast of domains aligned up or down is shown in Figure 3.7.

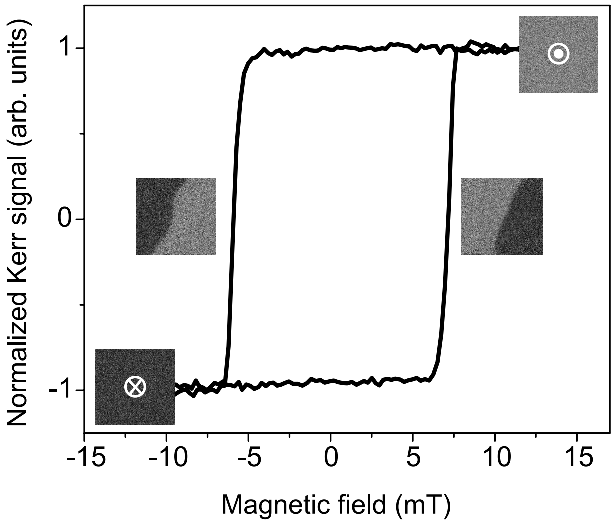

Figure 3.7: A magnetic hysteresis loop of W/CoFeB/HfO_2 annealed at 390°C for 1 hour showing the magneto-optical contrast of magnetic domains aligned up or down at different magnetic fields.

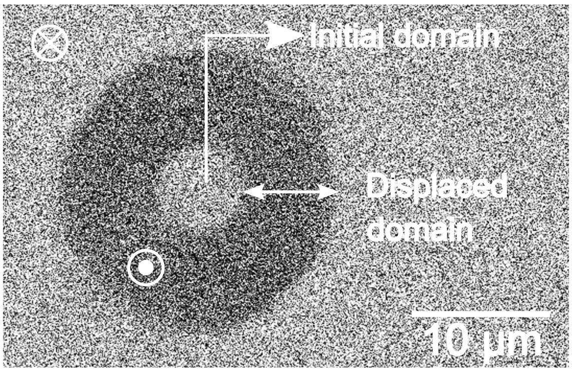

Figure 3.8: Expansion of a bubble domain in W/CoFeB/HfO_2 annealed at 390°C for 1 hour under an out-of-plane magnetic field pulse of 88 mT for 250 ns.

Kerr microscopy was also used to measure the domain wall velocity and determine the effective Dzyaloshinskii-Moriya interaction field ($\mu_0 H_{\mathrm{DMI}}$). To measure the domain wall velocity, the samples were first saturated in the out-of-plane direction and then a micro-coil was placed on the sample surface. A current pulse was sent to the micro-coil using a pulse generator such that an out-of-plane magnetic field in the direction opposite to the saturation of the sample nucleates bubble domains. The initial image is then subtracted followed by expanding the bubble domains by applying magnetic pulses of fixed pulse width. The domain wall velocity is calculated as the expansion of the bubble domain over the duration of the pulse. An illustration of the bubble expansion to calculate the domain wall velocity is shown in Figure 3.8.

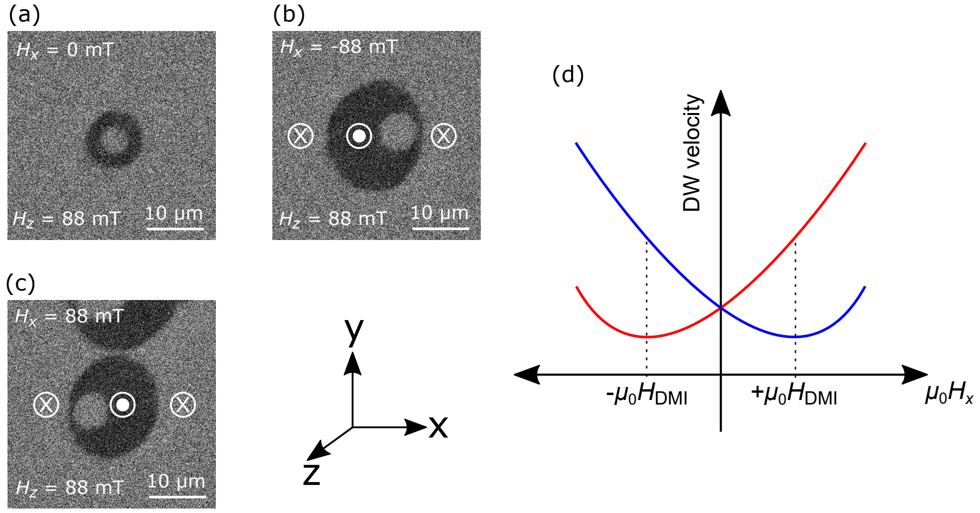

Figure 3.9: Differential Kerr images showing the asymmetric bubble expansion in W/CoFeB/HfO$_2$ annealed at 390°C for 1 hour under an in-plane magnetic field ($\mu_0 H_x$) (a) $\mu_0 H_x$=0 mT (b) $\mu_0 H_x$=-88 mT, and (c) $\mu_0 H_x$=88 mT. The DW displacements are obtained by applying an out-of-plane magnetic field pulse of 88 mT for 100 ns while $\mu_0 H_x$ is on (d) A corresponding schematic plot of left (blue line) and right (red line) domain wall (DW) velocities as a function of in-plane field ($\mu_0 H_x$) showing the effective Dzyaloshinskii-Moriya interaction field $\mu_0 H_{\mathrm{DMI}}$. The chirality of the domain wall in this case is right-handed.

The bubble expansion method can also be used to determine the chirality and strength of DMI [113, 114] in the presence of an in-plane magnetic field. In systems where DMI stabilizes Néel domain walls, an effective field $\mu_0 H_{\mathrm{DMI}}$ is present at the domain wall that either points outward or inward depending on the chirality. Hence, under the application of a continuous in-plane field $\mu_0 H_x$ (x-direction), the bubble domain expands asymmetrically with different velocities under an out-of-plane field pulse. In particular, the velocity of the domain wall on the left or right of the bubble domain can be either slow or fast when the effective field experienced by the domain wall is $\mu_0 H_x$ - $\mu_0 H_{\mathrm{DMI}}$ or $\mu_0 H_x + \mu_0 H_{\mathrm{DMI}}$, respectively. Hence, when the applied $\mu_0 H_x$ compensates $\mu_0 H_{\mathrm{DMI}}$, or in other words, H_x - $H_{\mathrm{DMI}} = 0$ or $H_x + H_{\mathrm{DMI}} = 0$, the domain wall velocity becomes minimum and the value of $\mu_0 H_{\mathrm{DMI}}$ is obtained. An illustration of the asymmetric bubble expansion technique showing different expansions of a bubble domain under an out-of-plane field pulse in the presence of continuous in-plane fields is shown in Figure 3.9.

With $\mu_0 H_{\mathrm{DMI}}$, the DMI constant can be extracted as,

$$\mu_0 H_{\mathrm{DMI}} = \frac{D}{M_s \Delta}, \tag{3.5}$$

where $\Delta = \sqrt{A/K_{\mathrm{eff}}}$ is the domain wall width and A is the exchange stiffness constant. The chirality of the domain wall can be determined from the direction of the magnetization of the initial bubble domain and the direction of expansion in the presence of a continuous in-plane field. For instance, the chirality of the domain wall shown in Figure 3.9 is right-handed as the expansion of the out-of-plane (toward reader) bubble domain in the presence of positive $\mu_0 H_x$ expands the right side of the bubble.

The Kerr microscopy measurements presented in this thesis were mainly performed at C2N and partly at Institut Néel, Université Grenoble Alpes, for the domain wall measurements at higher magnetic fields, with the help of Cristina Balan and Stefania Pizzini.

3.2.4 . Vibrating sample magnetometry

Vibrating sample magnetometry (VSM) is a commonly used magnetometry technique to measure the magnetic moment of a sample. VSM was invented and first reported in 1959 by Simon Foner [115].

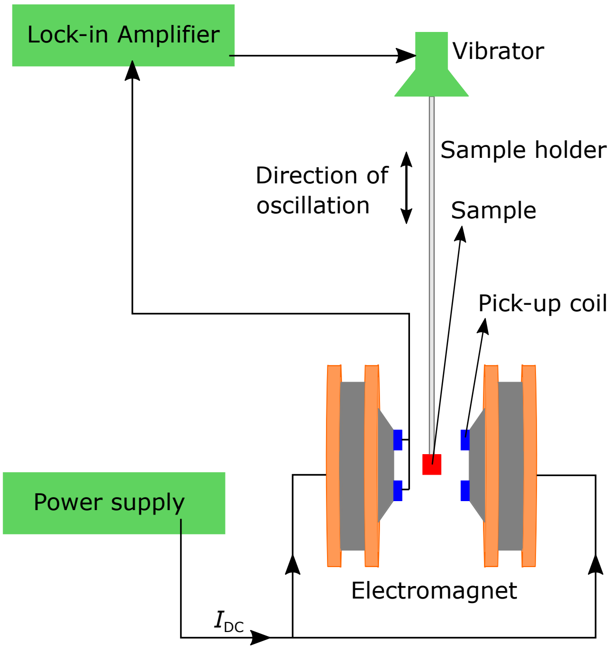

Figure 3.10: A schematic of a vibrating sample magnetometer with the different components showing the vibration of the sample (red) close to the pick-up coils (blue) in an applied magnetic field.

VSM works on the principle of Faraday's law of electromagnetic induction, which states that the rate of change of the magnetic flux (Φ) through a circuit generates an electromotive force (V_{emf}) in the circuit, described as:

$$V_{\text{emf}} = -N\frac{d\Phi}{dt}, \tag{3.6}$$

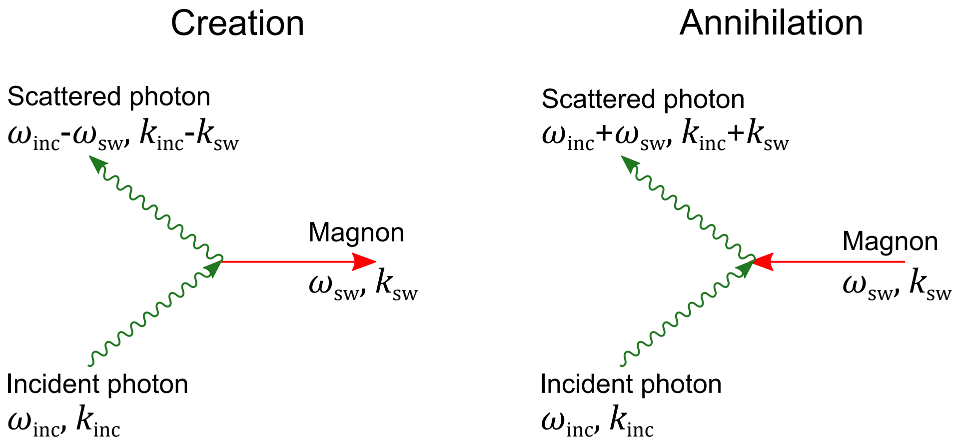

Figure 3.11: A schematic of the inelastic photon-magnon scattering process showing the creation (on the left) and annihilation (on the right) of a magnon.

where N is the number of loops in the circuit. In a VSM, the sample is placed in a magnetic field generated by the electromagnets and vibrated close to a pair of pick-up coils. The vibration of the sample causes a magnetic flux change in the pick-up coils that induces a voltage/current, which is proportional to the magnetic moment (Eq. 3.6) of the sample. The magnetic moment of the sample as a function of the applied magnetic field was then obtained using a lock-in technique to generate the magnetic hysteresis loops and extract the spontaneous magnetization M_s. A schematic of the VSM is shown in Figure 3.10.

The VSM measurements presented in this thesis were mainly performed at CEA, CNRS, Service de Physique de l'Etat Condensé (SPEC), with the help of Subhajit Roy, Tanvi Bhatnagar-Schoeffmann, and Aurélie Solignac and partly at Technical University of Cluj-Napoca, by Mihai Gabor.

3.2.5 . Brillouin light-scattering spectroscopy

Brillouin light-scattering (BLS) spectroscopy is an optical spectroscopy technique used to study the magnetization dynamics in the GHz frequency range. BLS is named after the French physicist Léon Nicolas Brillouin, who predicted the interaction of light with thermally generated acoustic vibrations in 1922 [116], and is one of the most important tools used today to measure the magnetic properties such as anisotropy, damping and DMI.

The working principle of BLS is based on the interaction of the photons of an incident light with the oscillations in a sample. These oscillations can be acoustic (phonons), dielectric (polarons) or magnetic/spin waves (magnons). In this thesis, BLS was used to study the magnetic properties, which is based on the inelastic scattering of a photon by a magnon. A schematic of the photon-magnon (spin wave) scattering process is shown in Figure 3.11. When an incident photon of angular frequency $\omega_{\rm inc}$ and wavevector $k_{\rm inc}$ interacts with the sample, the scattered photon can either create or annihilate a magnon of angular frequency $\omega_{\rm sw}$ and wavevector $k_{\rm sw}$. In the process of creation of a magnon, the scattered photon has a reduced angular frequency $\omega_{\rm inc}$-$\omega_{\rm sw}$ and wavevector $k_{\rm inc}$-$k_{\rm sw}$, and in the process of annihilation of a magnon, the scattered photon has an increased angular frequency $\omega_{\rm inc}+\omega_{\rm sw}$ and wavevector $k_{\rm inc}+k_{\rm sw}$ due to the conservation of energy and momentum. The associated energy of each process can be described as:

$$\hbar\omega_{\rm sc} = \hbar(\omega_{\rm inc} \pm \omega_{\rm sw}), \tag{3.7}$$

$$\hbar k_{\rm sc} = \hbar(k_{\rm inc} \pm k_{\rm sw}), \tag{3.8}$$

where $\hbar$ is the reduced Planck's constant and $\omega_{\rm sc}$ and $k_{\rm sc}$ are the angular frequency and wavevector of the scattered photon, respectively. In other words, the process is called Stokes process when a magnon is created and anti-Stokes process when a magnon is annihilated by an incident photon. The frequencies associated with Stokes and anti-Stokes processes can be described as:

$$F_{\rm Stokes} = F_{\rm inc} - F_{\rm sw}, \tag{3.9}$$

$$F_{\rm anti-Stokes} = F_{\rm inc} + F_{\rm sw}, \tag{3.10}$$

BLS was implemented in the Damon-Eshbach geometry to extract the magnetic properties presented in this thesis. In the Damon-Eshbach geometry, the magnetization of the sample is parallel to the sample surface and the spin waves with opposite chiralities (clockwise or anticlockwise) propagate opposite to each other and perpendicular to the direction of the magnetization. To set the magnetization of the samples in-plane, sufficiently large in-plane magnetic fields were applied. A green laser beam of wavelength 532 nm that has a narrow bandwidth and large coherence length ($>$ 100 m) was then focused on the sample with a spot size of approximately 50 μm after guiding through mirrors and lenses. The scattered light from the sample was then guided and passed through an analyzer that suppresses noise and reduces phonon contribution for magnetic properties measurements before entering a tandem Fabry-Pérot interferometer. The scattered light after passing through a 2 X 3-pass Fabry-Pérot (FP) interferometers in series was captured by an avalanche photodiode and analyzed. A schematic of the BLS spectroscopy is shown in Figure 3.12.

The frequency range of the BLS is set by the FP interferometers and is between 3 and 300 GHz for the setup used in this thesis, and the frequency resolution is set by the finesse or the reflectivity of the mirrors in the FP interferometers. The frequency range used in this thesis is 20 GHz with a precision of 0.1 GHz. In order to suppress the contribution from the transmission orders of the scattered light other than the main order, the two FP interferometers were placed in tandem with an angle α and the distance between the mirrors of FP1 to L1 and FP2 to L2 such

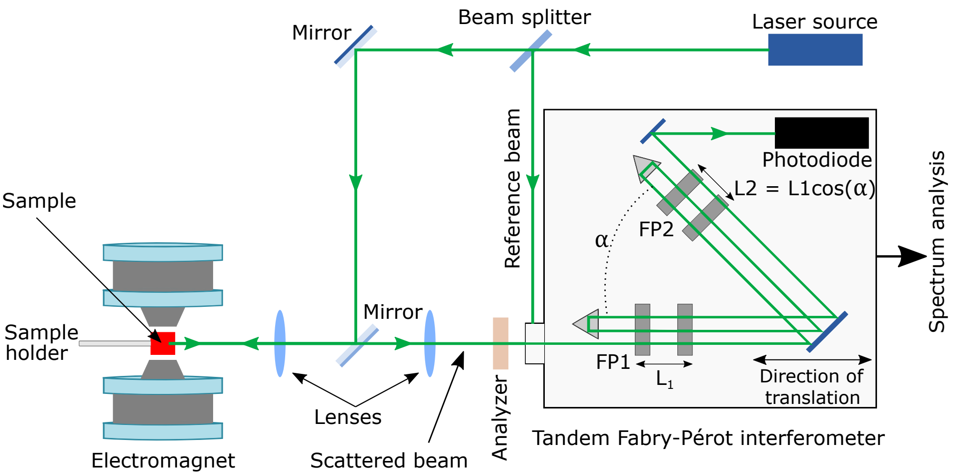

Figure 3.12: A schematic view of the Brillouin light-scattering spectrometer showing the propagation of a green laser beam toward the sample and after scattering, the beam is passed through the tandem Fabry-Pérot interferometer for the analysis.

that L2=L1cos(α) as shown in Figure 3.12. The layout of the setup also allows for changing the wavevector (thus frequency) by changing the angle of incidence θ (up to 60°) of the laser with the sample surface normal. The alignment of the sample with respect to the incident laser beam and the propagation of the spin waves in the Damon-Eshbach geometry is shown in Figure 3.13. The analyzed BLS spectrum is thus a signal of number of photons corresponding to the number of inelastic scattering events as a function of the frequency.

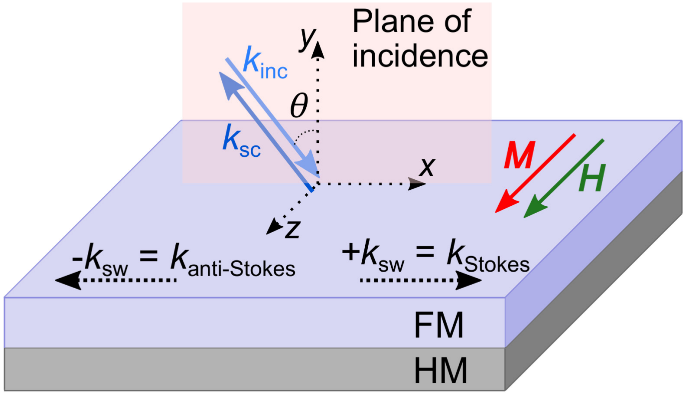

Figure 3.13: An illustration of the alignment of the sample with respect to the incident laser beam (k_{inc}) and the propagation of the spin waves (k_{sw}) in the Damon-Eshbach geometry.

The nonreciprocity of the spin waves of opposite wavevectors caused by the DMI is evaluated as a frequency shift between the Stokes and anti-Stokes frequency peaks [117]:

$$\Delta F = F_{\mathrm{Stokes}} - F_{\mathrm{anti-Stokes}} = \frac{2\gamma}{\pi M_{\mathrm{s}}} D_{\mathrm{eff}} k_{\mathrm{sw}} = \frac{2\gamma}{\pi M_{\mathrm{s}}} \frac{D_{\mathrm{s}}}{t_{\mathrm{FM}}} k_{\mathrm{sw}}, \tag{3.11}$$

where γ is the gyromagnetic ratio, D_{eff} is the effective DMI constant, M_{s} is the saturation magnetization, k_{sw} is the spin wave vector given by $4\pi\sin(\theta)/\lambda$, D_{s} is the surface DMI constant, and t_{FM} is the thickness of the ferromagnetic layer. Thus, the slope of a plot of the frequency shift ΔF as a function of k_{sw} (3.11) can be used to determine the DMI constant.

In addition to the DMI measurements, BLS was also used to measure the effective anisotropy M_{eff} and the effective damping parameter α_{eff}. To measure M_{eff}, Eq. 3.12 was used in which the applied in-plane magnetic field was varied for a fixed k_{sw}.

$$F_{\mathrm{avg}} = \frac{\gamma}{2\pi}\sqrt{(H + Jk_{\mathrm{sw}}^2 + P(k_{\mathrm{sw}}t_{\mathrm{FM}})4\pi M_{\mathrm{s}})(H + Jk_{\mathrm{sw}}^2 - P(k_{\mathrm{sw}}t_{\mathrm{FM}})4\pi M_{\mathrm{s}} + 4\pi M_{\mathrm{eff}})}, \tag{3.12}$$

where

$$F_{\mathrm{avg}} = \frac{F_{\mathrm{Stokes}} + F_{\mathrm{anti-Stokes}}}{2}, \tag{3.13}$$

$$J = \frac{2A}{M_{\mathrm{s}}}, \tag{3.14}$$

$$P(k_{\mathrm{sw}}t_{\mathrm{FM}}) = 1 - \frac{1 - e^{-(k_{\mathrm{sw}}t_{\mathrm{FM}})}}{k_{\mathrm{sw}}t_{\mathrm{FM}}} \tag{3.15}$$

F_{avg} is the average of the Stokes and anti-Stokes frequency peaks used to cancel the effects of DMI, and A is the exchange constant. To extract the effective damping parameter α_{eff}, the slope of a plot of the average of full width half maxima of Stokes and anti-Stokes frequency peaks (δF) as a function of the applied magnetic field, given by Eq. 3.16, was used:

$$\delta F = 2\alpha_{\mathrm{eff}}\frac{\gamma}{2\pi}H + \delta F_0, \tag{3.16}$$

where δF_0 is the extrinsic contribution to the linewidth.

The BLS measurements presented in thesis were performed at Laboratoire des Sciences des Procédés et des Matériaux (LSPM), Université Sorbonne Paris Nord, with the help of Djoudi Ourdani, Mohamed Belmeguenai and Yves Roussigné. The BLS peaks were fitted using a Lorentzian function.

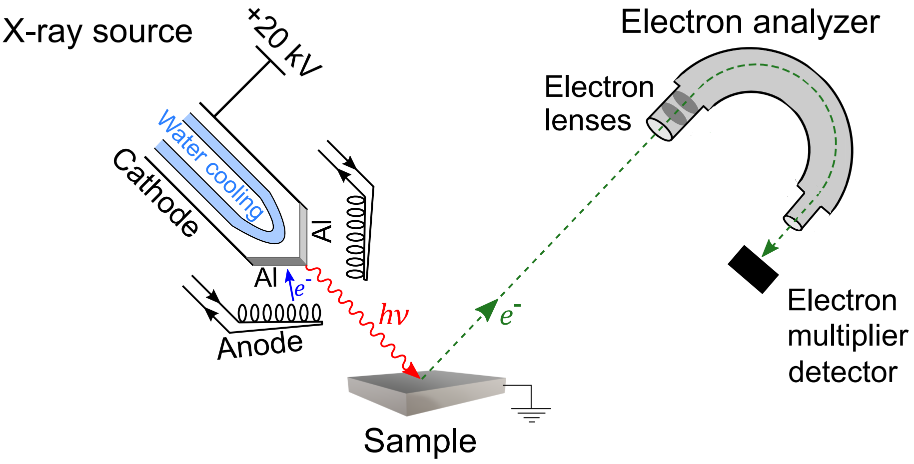

Figure 3.14: A schematic of a X-ray photoelectron spectroscopy setup showing an incident X-ray photon exciting an electron from the sample that is passed through a hemispherical analyzer and collected by a detector.

3.2.6 . X-ray photoelectron spectroscopy

X-ray photoelectron spectroscopy (XPS) is a surface-sensitive spectroscopic technique used to identify the elements and their chemical states. XPS is based on the photoelectric effect discovered by H. R. Hertz in 1887 [118], and was developed later to surface analysis in the mid 1960s by K. Siegbahn [119].

The basic principle of XPS relies on the photoelectric process. When a material is irradiated with X-rays from an X-ray source (Al Kα at 1486.6 eV or Mg Kα at 1253.6 eV), the absorption of an incident photon results in the emission of an electron from the material with a characteristic kinetic energy, which is linked to the binding energy of the corresponding core levels, and is described as:

$$E_K = h\nu - E_B - \phi \tag{3.17}$$

where E_K is the kinetic energy, h is the Planck's constant, ν is the frequency of the incident photon, E_B is the binding energy, and ϕ is the work function of the material. The work function, which is a correction factor for the instrument and the incident photon energy are known and the kinetic energy is measured by the analyzer. The binding energy can thus be calculated. A schematic of the XPS setup is shown in Figure 3.14.

The XPS measurements presented in thesis were performed at IMM-CNR, Unit of Agrate Brianza, by Alessio Lamperti. XPS was performed using a PHI ESCA 5600 (PHI Electronics) apparatus equipped with a monochromatic Al Kα X-ray source of energy 1486.6 eV and a hemispherical analyzer with pass energy equal to 57.80 eV and an energy resolution of 0.125 eV. The XPS peaks were fitted using pseudo Voigt functions and a Shirley + linear background.

4 - MAGNETO-IONICS IN Ta/CoFeB/HfO$_2$: MULTIPLE MAGNETO-IONIC REGIMES

In this chapter, we show that a gate voltage drives, in a nonvolatile way, the magnetic anisotropy of Ta/CoFeB/HfO$_2$ stack from an underoxidized state exhibiting in-plane anisotropy (IPA) to an optimum oxidation level resulting in perpendicular anisotropy (PMA) and further into an overoxidized state with IPA. The IPA $\rightarrow$ PMA regime is found to be significantly faster than the PMA $\rightarrow$ IPA regime, and only the latter shows full reversibility under the same gate voltages. The effective damping parameter also shows a marked dependence with gate voltage in the IPA $\rightarrow$ PMA regime, going from 0.029 to 0.012, and only a modest increase to 0.014 in the PMA $\rightarrow$ IPA regime. The existence of two magneto-ionic regimes has been linked to a difference in the chemical environment of the anchoring points of oxygen species added to underoxidized or overoxidized layers. These results show that multiple magneto-ionic regimes can exist in a single device and that their characterization is of great importance for the design of high performance spintronics devices.

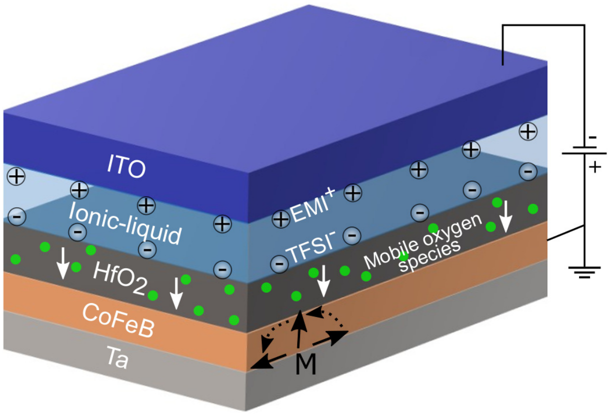

Figure 4.1: Graphic representation of the magneto-ionic stack used in this chapter. The gate voltage induces the motion of oxygen species in HfO$_2$.

4.1 . Sample structure and characterization

The magnetic materials used in this study are amorphous Ta (5nm)/Co$_{20}$Fe$_{60}$B$_{20}$ (1nm)/HfO$_2$ (3nm) films grown by magnetron sputtering, all samples investigated here were cut from the same wafer. The ionic liquid (IL) [EMI][TFSI] (1-Ethyl-3-methylimidazolium bis(trifluoromethanesulfonyl)imide) was added to the surface of the film to incorporate the IL gate. A counter electrode, a glass substrate coated with a 100 nm thick indium tin oxide (ITO) layer is subsequently placed on top of the IL. The size of the E-field biased area is of about 0.25 cm^2. Samples were stored in air and at room temperature before conducting the gating experiments if not indicated otherwise. The hysteresis loops have been measured by anomalous Hall effect using a bias current of 400 μA. All magnetic states presented here are non volatile, all measurements were conducted after switching off the gate voltage. A graphic representation of the device geometry is presented in Figure 4.1.

4.2 . Regimes I and II

In the initial state, before exposure to the gate voltage, the magnetic layers are underoxidized, exhibiting in-plane magnetic anisotropy (IPA). Under the action of a negative gate voltage applied to the top ITO electrode a first regime (I) is identified, in which IPA transitions into PMA, followed by a second regime (II) where further oxidation drives PMA into IPA. This entire anisotropy evolution is presented in Figure 4.2 with the corresponding cumulative biasing times for each case, these values correspond to the accumulated time of all previous operations. The gate voltage G_V=-2 V was applied for a total, accumulated time of t=1295 s. It is well known that thin magnetic films can exhibit a window of oxidation levels at the interface with an oxide which promotes PMA, while under/over oxidation will result in IPA [120]. Oxygen species are also known to migrate from the HfO_2 toward the CoFeB layer under gate voltages, as reported for other HfO_2 based devices [35, 121], therefore oxygen migration is thought to be at the heart of the effects observed here.

Figure 4.3 (a) shows the time dependence of the out-of-plane remanence percentage, where 100% corresponds to the Hall voltage at zero applied magnetic field in the PMA state, for the entire anisotropy range, going from the initial underoxidized IPA state through regime I (positive slope), PMA (the point of highest remanence), and regime II (negative slope) to finish in an overoxidized IPA state. As-grown samples have been investigated under three different constant gate voltages of G_V=-2.3 V (circles), G_V=-2 V (squares), and G_V=-1.7 V (triangles). The speed of the entire process critically increases for higher gate voltages, responding to a stronger driving force for ionic motion. For all applied gate voltages, the magneto-ionic process in regime I is significantly faster than in regime II. This difference in the time evolution as a function of gate voltage between regime I and II could be linked to a difference in the chemical environment, and thus of anchoring, of the oxygen species interacting with the CoFeB layer in regimes I and II. In regime I, the energy barrier associated with adding oxygen species to the underoxidized CoFeB interface may be lower than in regime II, where oxygen species have to be added to an already optimally oxidized CoFeB interface.

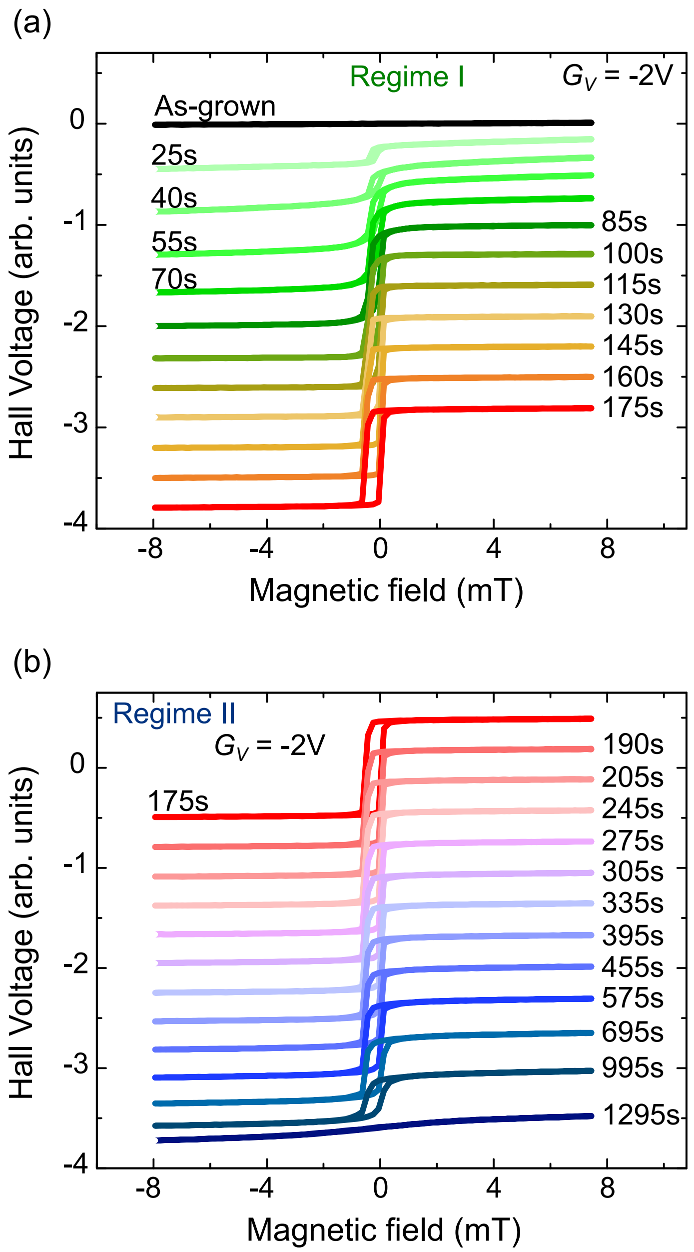

Figure 4.2: A progressive oxidation is induced upon exposure to a gate voltage G_V=-2 V. Different exposure times *t* drive an-grown system from IPA through regime I into PMA (a) and back to IPA through regime II (b).

Measurements were also conducted using underoxidized samples that were annealed before applying a gate voltage of -2 V, these measurements are presented in Figure 4.3 (b). An underoxidized sample was annealed at 180 °C (open squares) for one hour to reduce trapped H_2O molecules in the HfO_2 layer [122, 123] without inducing the crystallization of the CoFeB. Under G_V=-2 V, the speed of the ionic process in both regimes I and II was critically reduced, while still showing the same

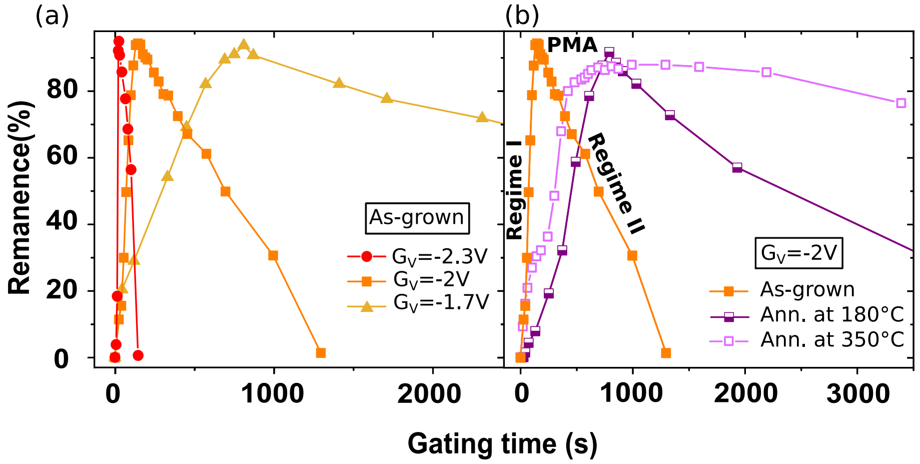

Figure 4.3: Remanence as a function of gating time in (a) as-grown samples under G$_V$=-2.3 V (circles), G$_V$=-2 V (squares), and G$_V$=-1.7 V (triangles). (b) Samples annealed at 180 °C (half open squares) and 350 °C (open squares) under G$_V$=-2 V.

difference previously discussed between regimes I and II. This has been linked to a contribution to the mobile oxygen species coming from air humidity, a feature observed in ionic systems based on hydrogen mobility [100]. A sample annealed at 350 °C (half open squares) for one hour was also investigated under G$_V$=-2 V. These annealing conditions are known to induce the formation of crystallized grains in CoFeB/MgO stacks, where the MgO layer acts as a crystallization template [124, 125]. In CoFeB/HfO$_2$, a similar behaviour could be expected, where the formation of crystalline grains would have an impact in ionic mobility. Figure 4.3 shows that this is indeed the case, regime I is slower than in the as-grown sample while regime II is significantly slower with respect to all other samples investigated. As mentioned earlier, the chemical environment of the mobile oxygen species at their anchoring points in the CoFeB layer is likely to be nonequivalent in regimes I and II. An already slower regime II further reducing its speed in crystallized samples may be an indication that ions in this regime do not only occupy binding sites at the already oxygen rich interface but that they could also penetrate into the layer. In this context, the crystalline structure of the CoFeB grains could hinder the diffusion of ions inside the layer with respect to the amorphous case, significantly reducing the speed and efficiency of the incorporation of oxygen species.

Regimes I and II do not only show two distinct speeds of the magneto-ionic process but they also show different reversibility behaviors. The reversibility of the effects of a gate voltage of -2 V has been tested with positive gate voltages going up to +4 V in regimes I and II of as-grown samples. Higher voltages have not been applied due to the electrochemical limitations of the ionic liquid [56]. The effects of the application of +4 V for 10 minutes and up to one hour to a magnetic state close to PMA in regime I are shown in Figure 4.4 (a), where only minor changes

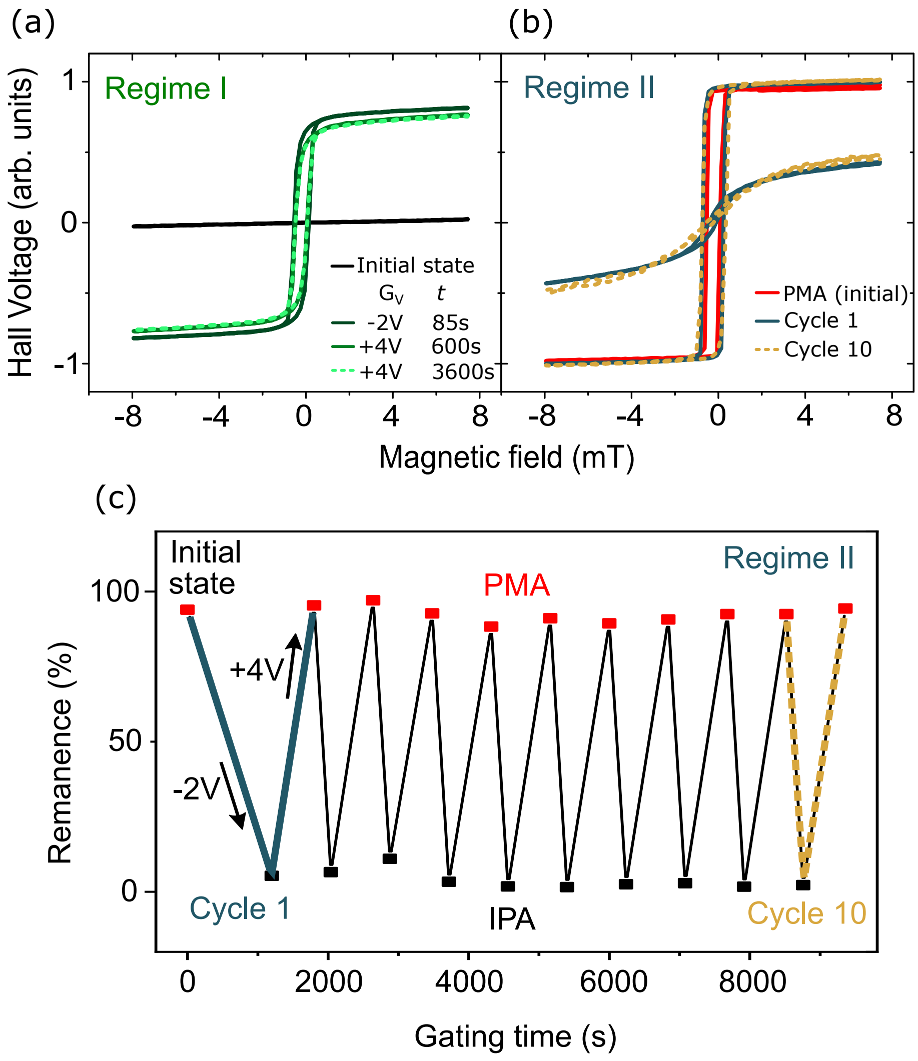

Figure 4.4: (a) Suppressed reversibility of the IPA → PMA transition under G_V=+4 V in regime I. (b) Hysteresis loops for the reversible PMA → IPA cycles 1 (solid line) and 10 (dotted line) in regime II. (c) Remanence as a function of the reversibility cycle number in regime II.

are induced in the magnetic state. The same effect is found for other intermediate states in regime I and also for the fully perpendicular state, positive gate voltages up to +4 V and long exposure times can not induce a recovery of the initial under oxidized state. Regime II shows an entirely different behaviour; a fully reversible transition between IPA and PMA can be observed. Figure 4.4(b) shows the Hall voltage hysteresis loops corresponding to reversibility cycles number 1 and 10, while Figure 4.4(c) shows the remanence variation of the entire series. The ten cycles show a switching of the remanence between nearly 0 % (IPA) and 100 % (PMA) under gate voltages of -2 V and +4V, respectively. It is interesting to notice that in the first cycle, the PMA → IPA transition is induced by the application of -2 V for 1200 s, while for all subsequent cycles a shorter time of 240 s is required for this transition to occur. For the IPA $\rightarrow$ PMA transition an exposure time of 600 s has been found to be sufficient for all cycles. This shows that the magneto-ionic process most likely undergoes a first 'activation' phase in which the first diffusion of ions involves an additional energy barrier. This could be related to the energy cost of a first detachment of the ions from their original anchoring points as well as to the formation of ionic conduction channels in the CoFeB layer, after which the ions can be moved reversibly by using significantly lower exposure times.

Regime I is therefore showing a relatively faster dynamics than in regime II under G$_V$=-2 V and a highly suppressed reversibility at G$_V$=+4 V, while in regime II, a slower dynamics and full reversibility are observed. This may be linked to a high degree of stability of the final position of the ions within regime I, which would create a high energy barrier for the inverse process, suppressing reversibility under a gate voltage of +4 V. In regime II, although the energy barrier remains asymmetric between the PMA $\rightarrow$ IPA and PMA$\leftarrow$IPA transitions, a gate voltage of +4 V is sufficient to revert the effects of a gate voltage of -2 V. This could be linked to a weaker anchoring of the mobile oxygen species in regime II.

4.3 . Effective damping parameter

In this section, we will discuss the impact of magneto-ionics on the effective damping parameter α_{eff}. A series of samples exposed to gate voltages -2 V and -1.5 V has been investigated by Brillouin light scattering (BLS) in the Damon-Eshbach geometry after removal of the IL gate. The in-plane magnetic field dependence of the average frequency of the Stokes and anti-Stokes spin-wave frequencies was measured at a wavenumber k=8.08 μm^{-1}. Figure 4.5(a) shows this dependence for the as-grown sample (black circles) and for samples exposed to G$_V$=-2 V for 45 s (underoxidized, green circles), 360 s (PMA, red circles) and 2700 s (overoxidized, cyan circles). A theoretical modelling of this dependence has been performed according to [117] resulting in the fitting lines shown in Figure 4.5(a). From this fitting, the values of the effective magnetisation $M_{\text{eff}} = M_{\text{s}} - H_k$ have been obtained, where M_{s} and H_k are the saturation magnetisation and the anisotropy field, respectively. Figure 4.5(b) shows the corresponding plots of the average of full width half maxima of Stokes and anti-Stokes frequency peaks (δF) as a function of the magnetic field applied in the plane of the sample and the corresponding fitting lines to: $\delta F = 2\alpha_{\text{eff}}(\gamma/2\pi)H + \delta F_0$, where α_{eff} can be extracted from the slope. The dependence of α_{eff} on exposure time to a gate voltage of -2 V (black squares) and -1.5 V (yellow squares) is presented in Figure 4.5(c), where the inset shows also the dependence on $\mu_0 M_{\text{eff}}$.

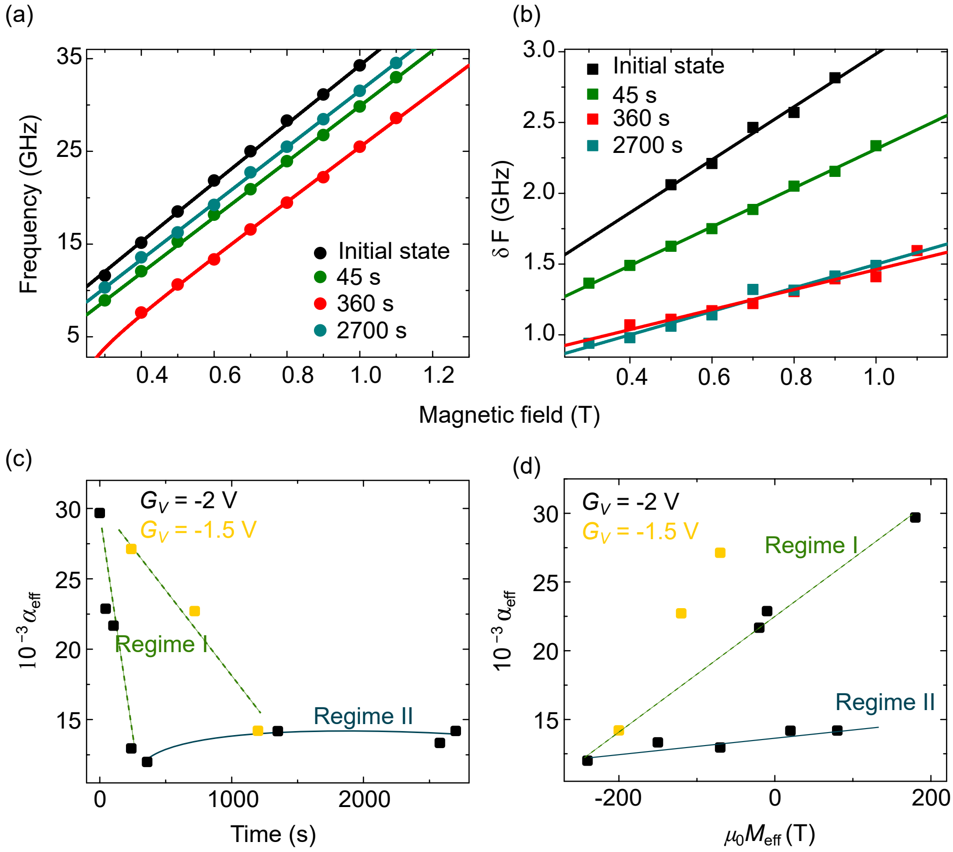

Figure 4.5: (a) BLS average frequency and (b) full width half maxima as a function of magnetic field for an as-grown (black circles) sample, and for samples exposed to G_V=-2 V for 45 s (green circles), 360 s (red circles) and 2700 s (cyan circles), and the corresponding fitting lines. α_{eff} dependence on exposure time (c), and $\mu_0 M_{\text{eff}}$ (d) to G_V=-2 V (black squares) and G_V=-1.5 V (yellow squares). Lines are a guide to the eye.

In regime I, the value of α_{eff} rapidly decreases from 0.029 for the as-grown sample to 0.012 for the PMA state. As shown earlier, the change from G_V=-2 V to G_V=-1.5 V critically decreases the speed of the process. In regime II, a relatively small increase in α_{eff} to 0.014 is observed, however, it does not show to have a marked dependence on the exposure time. This difference between regimes I and II is also expressed in the α_{eff} vs. $\mu_0 M_{\text{eff}}$ dependence, where a monotonic decrease is seen in regime I, in contrast with the much less pronounced increase seen for regime II in a similar $\mu_0 M_{\text{eff}}$ range.

It is important to mention that the values of α_{eff} obtained from the slopes of the data points in Figure 4.5(b) contain not only the intrinsic contribution from the Gilbert damping parameter but also an extrinsic contribution. This extrinsic contribution can be associated with a variety of sources including spin pumping [126–128], due to the proximity with a heavy metal with high spin-orbit coupling, two-magnon scattering [129] or the existence of sample inhomogeneities such as a distribution of anisotropy values across the sample [130, 131]. The extrinsic contribution can add a relatively small factor to the value of the Gilbert damping or in more extreme cases it can dominate the δF vs H dependence resulting in the loss of linearity [130, 131].

The damping parameter in CoFeB has been shown to depend on the oxidation level at the interface. In CoFeB/Gd/MgO stacks, the thin Gd layer serving as an oxygen sink has been shown to modulate the level of oxidation of an overoxidized CoFeB. In this system, α_{eff} shows a non-monotonic dependence on the thickness of the Gd layer where a minimum is reached for 0.6 nm [132]. However, this has been linked mostly to changes in the degree of homogeneity and quality of the interface. As mentioned, the proximity and quality of the interface with a high spin orbit coupling material has been shown to induce a spin-pumping contribution to the effective damping which shows as an inverse proportionality between α_{eff} and the thickness of the magnetic film [133, 134]. This additional damping contribution has been quantified for Ta by comparing symmetric MgO/CoFeB/MgO and Ta/CoFeB/Ta stacks to asymmetric Ta/CoFeB/MgO, where the Ta contribution dominates over the MgO contribution [135]. This has also been shown in the case of Hf/CoFeB/MgO stacks, which show for a CoFeB thickness of 1.08 nm, α_{eff} values that are higher than in MgO/CoFeB/MgO stacks by about a factor of five [136].

Taking into account these considerations, it can be concluded that in the present case the underoxidized samples could have a significantly larger contact surface with Hf in $\mathrm{HfO_2}$ than in the optimally oxidised case. A progression in regime I toward PMA could therefore decrease the contact surface with Hf and significantly reduce the associated spin pumping contribution to α_{eff}. Interestingly, the changes in α_{eff} are minor in regime II, which supports the idea mentioned earlier that in this regime oxygen species may migrate mostly into the layer rather than binding at the already optimally oxidized interface reached after regime I. This is considered as the main contribution to the observed variations in α_{eff}, however, a reordering of the interface structure throughout regime I is also a likely scenario. A sharper interface may be reached at the end of regime I, also leading to the highest PMA state, which could also play a role in the observed reduction of α_{eff}.

4.4 . Discussion

The proposed magneto-ionic mechanisms involved in regimes I and II are depicted in Figure 4.6. For $\mathrm{G}_V < 0$, mobile oxygen species inside $\mathrm{HfO_2}$, represented as green dots, migrate toward the CoFeB layer and after G_V is switched off (b), they remain bound to the CoFeB, achieving an optimum surface coverage and

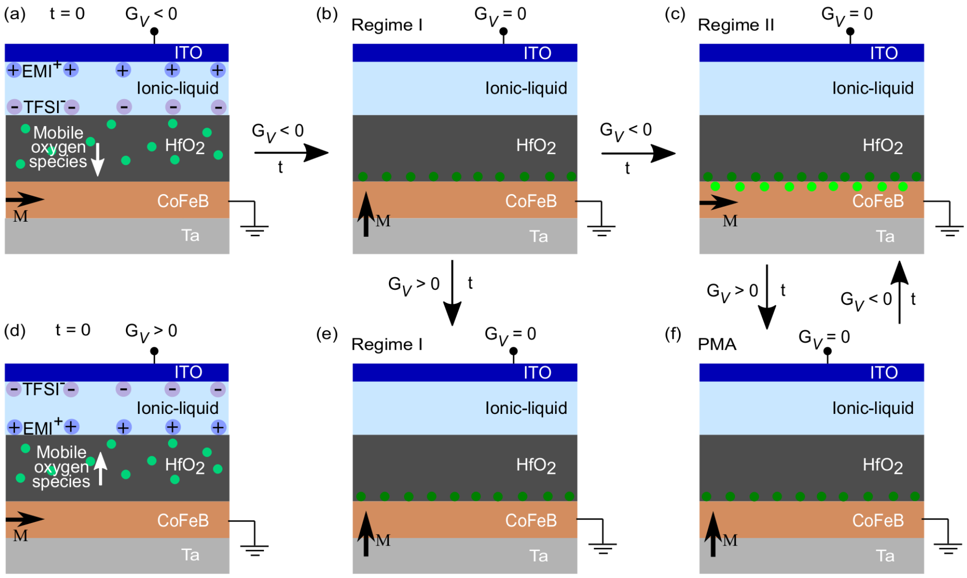

Figure 4.6: Proposed magneto-ionic mechanisms for regimes I and II. (a) For $G_V < 0$ oxygen species migrate toward the CoFeB layer achieving an optimum surface coverage and PMA at the end of regime I (b). If $G_V < 0$ continues to be applied, oxygen species will continue to be incorporated into the CoFeB layer in regime II (c) resulting in IPA. Under $G_V > 0$ mobile oxygen species can migrate back to the top electrode (d). For the same applied G_V, there is no reversibility in regime I ((b) and (e)), while full reversibility is achieved in regime II ((c) and (f)).

completing the IPA → PMA transition at the end of regime I. If $G_V < 0$ continues to be applied, the magneto-ionic mechanism will move into regime II. After the voltage is switched off (c), the incorporated oxygen species will contribute to the PMA → IPA transition. As the starting point of regime II is an optimally oxidized CoFeB surface, oxygen species incorporated in regime II will be less likely to bind at the same binding sites available in regime I and can potentially penetrate further into the layer (light green dots).

Under high enough positive gate voltages, mobile oxygen species are expected to migrate back to the top electrode (d). However, for the same applied $G_V > 0$, reversibility is highly suppressed for oxygen species incorporated in regime I ((b) and (e)), while full reversibility is achieved in regime II ((c) and (f)). This discrepancy in the degree of reversibility of regimes I and II is attributed to the differences in the binding sites, and the associated anchoring strength, of the oxygen species incorporated in each regime. The difference in chemical environment for these two types of binding sites is proposed as the origin of magneto-ionic regimes I and II.

A preferential occupation of a limited number of binding sites at the CoFeB/HfO_2 interface in regime I could also explain the observed larger impact of ionic migration on the value of α_{eff} with respect to regime II. As mentioned, the effects observed may be due to a decoupling of the CoFeB surface from the Hf atoms in HfO_2, mostly linked to ion incorporation at the surface of an underoxidized CoFeB rather than to ionic migration into the layer in regime II. This is valid in a scenario where ionic migration into the layer is limited to the vicinity of the CoFeB/HfO_2 interface and does not extend up to the Ta/CoFeB interface as seen in other systems where higher gate voltages are applied [35]. It could be anticipated that ionic migration up to the Ta/CoFeB interface could induce a significant decoupling from the Ta layer, an effect observed in Pt/Co reflected as a reduction of the DMI [35], resulting in a further reduction of α_{eff}. Another important indication supporting the proposed mechanism is found in the measurements done on crystallized samples. In this case, the time evolution of magnetic anisotropy under a negative gate voltage is strikingly reduced in regime II compared to regime I. This could be due to an increased difficulty of ionic diffusion into a crystallized CoFeB layer in regime II, compared to ionic incorporation at the surface in regime I.

Surface and bulk components to the magneto-ionic effect have already been introduced in the literature, in particular, in Pd/Co/GdO_x and Pt/Co/HfO_2 films, where ion migration deep down into the magnetic layer and beyond can cause partial or total irreversibility [35, 137]. As mentioned, in the present case the bulk component is thought to be limited only to the vicinity of the CoFeB/HfO_2 interface. The observed suppressed reversibility seen in regime I happens at low oxygen content, ruling out the anchoring of the oxygen species deep into the layer as a potential source of irreversibility. This is also well supported by the subsequent observation of regime II, exhibiting full reversibility, in the overoxidized state.

In this context, studies in the literature addressing the incorporation of oxygen species from the gas phase into crystalline Co and Fe systems provide an interesting perspective. In Co, the profile of the oxygen intake as a function of oxygen pressure has a distinct change in slope that is related to a two stage oxidation process. The first step involves the formation of CoO up to a defined surface coverage threshold, after which a higher oxygen and high temperature exposure leads to the formation of Co_3O_4 [138]. In Fe crystals, a similar behaviour has been observed at room temperature. The oxygen sticking coefficient as a function of surface coverage is seen to decrease drastically up to a coverage of 0.5, where an inflection point occurs followed by a less pronounced decrease. The initial phase of rapid decrease has been linked to the filling of preferential empty binding sites, while additional oxygen incorporation leads to the inflection point identified as the onset of oxide growth. The oxygen incorporation is proposed to entail a progression from initially adsorbed oxygen species to the nucleation and expansion of a two dimensional layer of FeO at the sticking coefficient inflection point, where it remains fairly constant until the completion of the FeO layer formation. Further oxygen incorporation happens in the presence of FeO, which is responsible for the observation of a reduction in the sticking coefficient after the inflection point. This last process ultimately leads to the formation of Fe_2O_3/ Fe_30_4 together with the appearance of a three dimensional oxide structure [139, 140].

In amorphous systems, the distinction between the well defined oxide phases present in crystalline systems could be less evident, however, a distinction between purely surface incorporation and a subsequent oxygen intake more extended into the magnetic layer could be evidenced. The films used in this study are Fe rich, with a composition of $Co_{20}Fe_{60}B_{20}$, where variations of the Fe content at the interface with an oxide have been shown to drive large PMA variations [141]. It is therefore worth considering a scenario where the formation of different Fe oxide types is at the origin of regimes I and II. Regime I is likely to reflect the initial oxygen adsorption and formation of FeO, which involves a change in valence from Fe^0 to Fe^{2+}. A significantly high energy barrier is therefore introduced for the inverse process which would largely suppress reversibility under a low energy stimulus. On the other hand, the full completion of a two dimensional FeO layer could well lead to an optimum and homogeneous oxidation at the interface, allowing for the highest PMA values observable in this system. As mentioned, further oxygen incorporation in the presence of FeO becomes less favourable, which is in line with the observed slower dynamics seen in regime II. The Fe_2O_3/ Fe_3O_4 oxide phase involves a mixture of Fe^{2+} and Fe^{3+} states, therefore it can be proposed that the path toward a $Fe^{2+} \rightarrow Fe^{3+}$ transition involves the progressive addition of oxygen species to the chemical environment of the Fe^{2+} centres. This phase is thought to describe regime II, where a relatively low energy barrier is involved in the inverse process due to the conservation of the Fe^{2+} valence state. An ultimate change to Fe^{3+} would also be expected to introduce a large energy barrier for the inverse process and hinder reversibility, as seen in regime I. This is well in line with the observed behaviour under G_V= -3 V (120 s exposure time), where the system enters an irreversible IPA overoxidized state.

4.5 . Conclusion

In conclusion, we have shown the existence of two distinct non-volatile magneto-ionic regimes in Ta/CoFeB/HfO_2 stacks where oxygen species migrate under negative/positive gate voltages toward/away from the CoFeB layer. This voltage driven ionic motion induces first an IPA $\rightarrow$ PMA transition in regime I, corresponding to a transition from an underoxidized to an optimally oxidized state. In regime II, a PMA $\rightarrow$ IPA transition occurs and it is correlated to a transition from an optimally oxidized to an overoxidized state. Regime I shows a much faster dynamics and highly suppressed reversibility for positive gate voltages with respect to regime II. In addition, it also shows a marked decrease of the effective damping parameter from 0.029 to 0.012 compared to the relatively small increase to 0.014 observed in regime II. The existence of regimes I and II is proposed to be the result of a difference in the binding strength of the migrated oxygen species, that can be correlated with different binding sites on the surface and inside the CoFeB layer, respectively. The results presented here reveal the complexity of magneto-ionics and the importance of a deep understanding of the ionic mechanisms involved in order to design robust and reliable devices for spintronics applications. This system could be easily transferred to a solid state device where the two regimes could be probed at higher gate voltages in order to re-evaluate reversibility and explore fast operation times. This will allow to choose an IPA to PMA transition, either in regime I or II, that best fits the requirements for practical applications and to design strategies to favour operation in one of the two magneto-ionic regimes.

5 - MAGNETO-IONICS IN W/CoFeB/HfO$_2$: THE EFFECTS OF POST-GROWTH ANNEALING

This chapter presents the magneto-ionic modulation of the DMI and PMA in W/CoFeB/HfO$_2$ stacks annealed at different temperatures and for varying annealing times. A large modulation of PMA and DMI is observed in systems annealed at 390°C and 350°C, whereas no response to voltage is observed in as-grown samples. A strong DMI is only observed in samples annealed at 390°C for 1 hour, while PMA is present for all annealing times at temperatures of 390°C and 350°C. Magnetic properties including domain wall velocity improve drastically with increasing annealing temperature and time, while the magneto-ionic reversibility is increasingly compromised. The changes in PMA and DMI induced by the gate voltages in the samples annealed at 390°C are permanent, while partial reversibility is only observed for samples annealed at 350°C for short times. This dependence of reversibility on post-grown annealing has been associated to the influence of crystallization on ion mobility. These results show that a compromise between enhancement of the magnetic properties and magneto-ionic performance could be needed in systems requiring annealing to develop PMA and DMI.

5.1 . Introduction

W/CoFeB-based systems are known to exhibit DMI and PMA, as well as a large spin Hall angle in the β-phase of W [142, 143], which makes them very attractive for spintronics applications. In these systems, post-growth annealing is systematically used to enhance DMI, and PMA,[18] which in W/CoFeB/MgO is associated with the crystallization of CoFeB [144]. In addition, oxygen incorporation into W/CoFeB/MgO has been used to enhance spin-orbit torques [145]. Therefore, the characterization of the magneto-ionic response using oxygen species in annealed W/CoFeB/HfO$_2$ stacks is of significant interest.

5.2 . Sample preparation, structural characterization and electric field gating

The magnetic stack W (4 nm)/Co$_{20}$Fe$_{60}$B$_{20}$ (1 nm)/HfO$_2$ (3 nm) used in this study was grown by magnetron sputtering. Metals (W (99.95% pure), Co$_{20}$Fe$_{60}$B$_{20}$ (99.9% pure)) were DC-sputtered and HfO$_2$ (99.9%) was RF-sputtered. Before the deposition of the film, a base pressure of 4 x 10^{-8} mbar was achieved. The deposition rate and the magnetron output power for W, Co$_{20}$Fe$_{60}$B$_{20}$, and HfO$_2$, were 0.017 nm/s and 100 W, 0.114 nm/s and 400 W, 0.129 nm/s and 950 W, respectively and the sputtering gas used was Ar. The films used in this study have a single layer uniformity of 2.48%. The samples after deposition were annealed under different conditions of temperature and time (see Table 1) in a vacuum chamber at 10^{-5} mbar.

Table 5.1: Annealing parameters of samples S1 to S4

Sample	Ramp-up duration (minutes)	Annealing temperature (°C)	Dwell time (minutes)
S1	17	350	60
S2	22	390	60
S3	140	350	0
S4	140	390	0

A set of samples were then annealed at 350°C and 390°C using either a temperature program with a 140 min ramp-up time and zero dwelling time at the target temperature, or a short ramp-up time (17 or 22 min) and a 60 min dwelling time at the target temperature. The annealing conditions corresponding to each of the different samples studied (S1, S2, S3, and S4) are summarised in Table 5.1 and Figure 5.1. All annealed samples in our study show PMA.

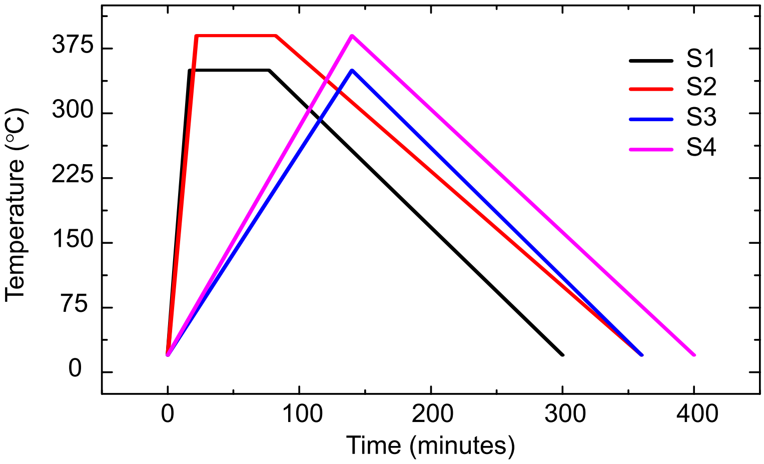

Figure 5.1: Annealing profiles of the samples S1, S2, S3, and S4.

Grazing incidence X-Ray diffraction was performed to collect the diffraction of the crystallographic planes normal to the sample surface. The XRD patterns of the as-grown and S2 samples are shown in Figure 5.2. The broad diffraction peak at 33°, and the peaks at 39.9° and 43.9°C in Figure 5.2 for the as-grown and annealed films correspond to amorphous HfO_2 [146] and to the 210 and 211 peaks

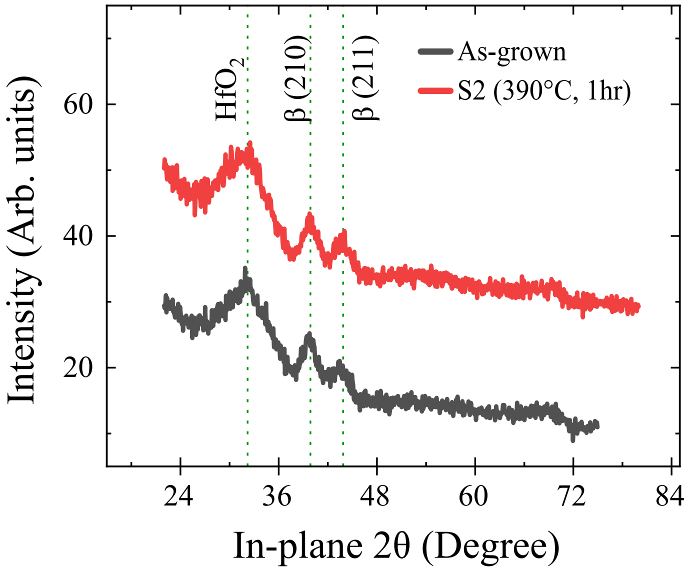

Figure 5.2: XRD patterns of an as-grown sample (black) and sample S2, annealed at 390°C for 1 hour (red).

of the β-phase of W [147], respectively, and confirm that the phases of HfO$_2$ and W remain the same before and after annealing. The peaks of CoFeB were not observed due to the detection limit of the diffractometer.

Electric fields were applied in devices with ionic-liquid gates. Gating was implemented by adding approximately 10 μL of ionic-liquid (IL) [EMI]$^+$[TFSI]$^-$ (1-Ethyl-3-methylimidazolium bis(trifluoromethanesulfonyl)imide) to the surface of the magnetic films. The dimensions of the films used for each device are 10 mm $\times$ 5 mm, the electric field was applied in the center covering an area of 5 mm $\times$ 5 mm. A glass substrate coated with a 100 nm thick indium tin oxide (ITO) layer was used as the top electrode to apply the gate voltages, while the magnetic film was connected to ground. ITO was connected to the voltage source by means of a silver wire glued to the ITO-coated glass plate with an electrically conductive epoxy adhesive. Experiments were performed at room temperature on samples cut from the same wafer and all magnetic states presented here are non-volatile. A schematic of the device is shown in Figure 5.3a.

5.3 . Results and Discussion

Figure 5.4 shows the magnetic hysteresis loops of the as-grown and S2 samples obtained using a polar MOKE. As-grown samples have an in-plane (IP) easy magnetization axis. PMA in CoFeB/oxide based heterostructures can arise due to the 2p-3d hybridization between orbitals from oxygen and the ferromagnet. This contri-

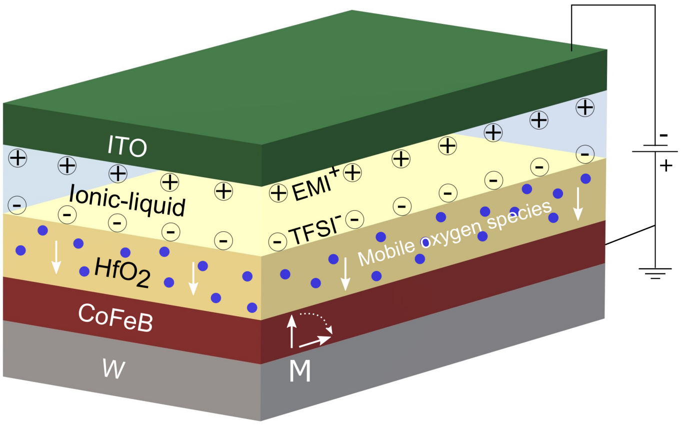

Figure 5.3: A schematic of the structure of the liquid gated device showing migration of oxygen species (blue dots) in HfO_2 under a gate voltage.

bution to PMA is dominant, for example, in the archetypal Ta/CoFeB/MgO stacks and in Pt/Co/AlOx systems [120] and can be exploited to induce PMA through magneto-ionic control of the oxidation level at the FM/Oxide interface [35, 148]. In the present case, neither positive (+4 V) nor negative gate voltages (-2.3 V, -2.5 V and -3 V) produced an out-of-plane (OOP) signature in pMOKE for as-grown samples, as shown in Figure 5.4a. In contrast, in other liquid-gated systems based on $Pt/Co/HfO_2$ and $Ta/CoFeB/HfO_2$, the underoxidized as-grown state shows PMA after application of similar negative voltages, due to the controlled oxidation of the FM/Oxide interface [35, 148]. It has been shown that a significant contribution

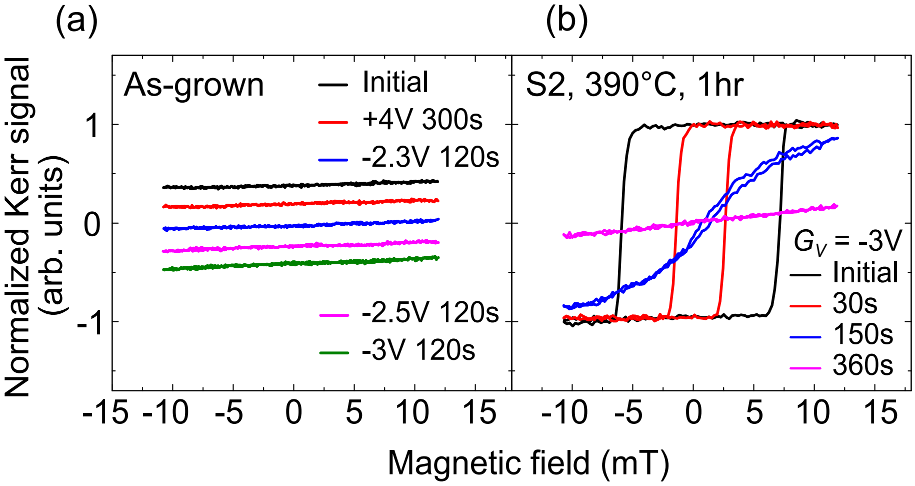

Figure 5.4: Polar MOKE hysteresis loops under an out-of-plane magnetic field of the (a) as-grown and (b) annealed S2 sample under gate voltages.

to PMA can also arise from the heavy-metal (HM)/FM interface which depends on factors such as the 5d-3d hybridization of the orbitals of the heavy metal and ferromagnet, interface intermixing and interface structure [142, 144, 149]. The contribution of the HM/FM interface to PMA has been found to be particularly important in W/CoFeB/MgO systems, including a significant dependence of PMA on the W crystalline phase [142]. In these systems there is also a need of thermal annealing at minimum temperatures close to 250°C to obtain PMA [142,149]. The importance of the W/CoFeB interface contribution to PMA, and its link to thermal annealing, is the base of our interpretation of the lack of magneto-ionic response in as-grown W/CoFeB/HfO_2. A gate-controlled oxidation at the CoFeB/HfO_2 interface alone does not induce PMA in our system, thermal annealing is still a necessary step. Hence, a series of samples were annealed at different conditions (see section 5.2) to induce PMA and study the magneto-ionic response. Once PMA is induced through annealing, a gate voltage-induced oxidation of CoFeB was shown to drive the easy axis from OOP to IP for the annealed samples. For instance, a gate voltage of -3 V applied to S2 (annealing at 390°C for 1 hour) was shown to progressively drive the magnetization from OOP to IP after a total exposure time of 360 s, as shown in Figure 5.4b. In the following, the magneto-ionic response in samples annealed under different conditions will be discussed, where PMA is present in the initial state, before the application of gate voltages.

5.3.1 . Dzyaloshinskii-Moriya interaction (DMI)

The evolution of the surface DMI (D_s) as a function of the gating time was calculated from the frequency asymmetry ΔF between the Stokes and anti-Stokes peaks obtained using Brillouin light scattering (BLS) spectroscopy measurements. Figure 5.5a shows the variations in ΔF as a function of the wave vector k for different gating times, where ΔF was obtained from the BLS spectra, as shown in Figure 5.5b and c for two cases. The DMI constant D, was extracted from the slope of ΔF as a function of k (see section 3.2.5) and D_s is represented as $D_\mathrm{s} = D \cdot t$, where t is the thickness of the CoFeB layer, respectively. The corresponding variations in $M_\mathrm{s} \cdot t$ are shown in Figure 5.5d, where M_s is the saturation magnetization. The positive sign of D_s in our system indicates a right-handed chirality, as reported in other W/CoFeB systems [142, 150]. As shown in Figure 5.5, D_s shows a sharp decrease from the 0.62 pJ/m measured before exposure to the gate voltage down to 0.06 pJ/m after a gating time of 135 s. After this point, no significant variations are observed for longer gating times. This gate-voltage-induced decrease in D_s corresponds to a variation by a factor of 10 that accompanies the SRT shown in Figure 5.4b. $M_\mathrm{s} \cdot t$ shows a similar profile, where the loss of magnetic moment could be attributed to the oxidation of Fe and Co, due to the migration of oxygen species. Ion migration is also at the origin of the decrease in DMI, since it could result in a decoupling between the W and CoFeB layers as already proposed for Pt/Co/HfO_2/IL devices [35].

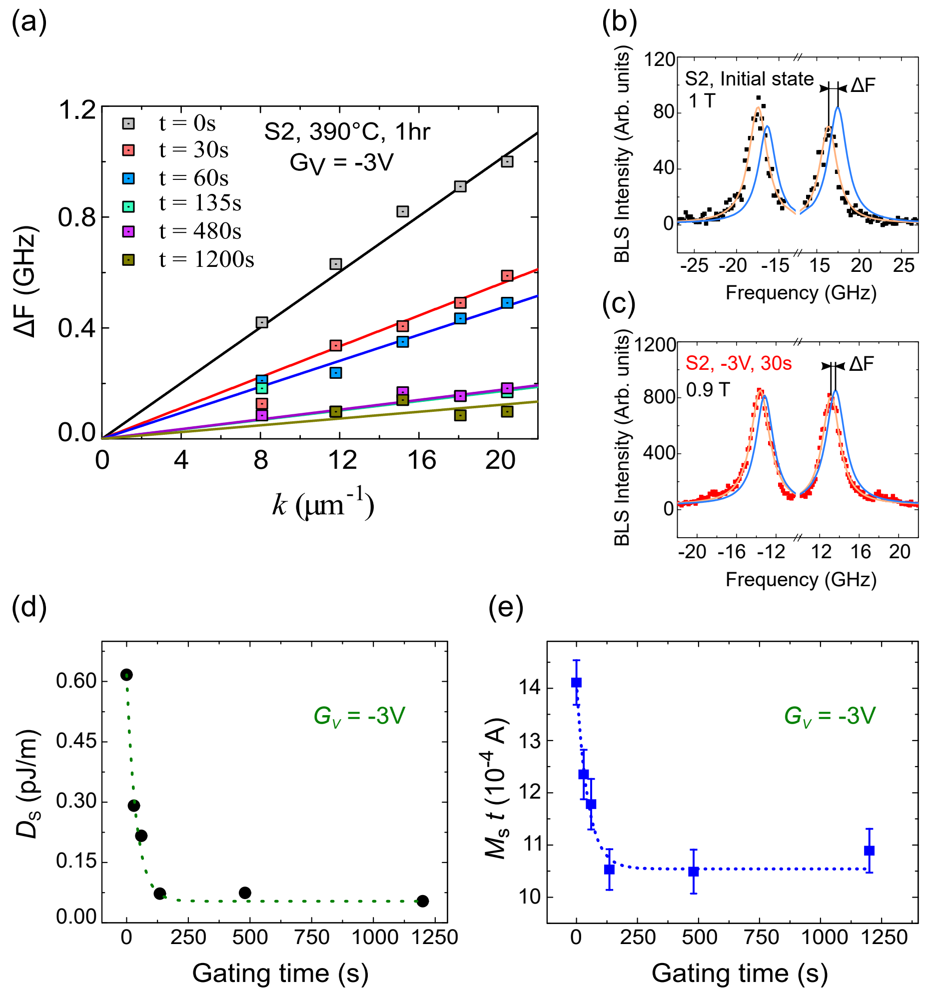

Figure 5.5: (a) Frequency asymmetry (ΔF) as a function of the wave vector (k) for S2 samples exposed to different durations of a gate voltage of -3 V. BLS spectra at k=20 μm^{-1} of S2 (b) in the initial state, and (c) after applying a gate voltage of -3 V for 30 s. (d) Surface DMI constant (D_s) and (e) $M_s \cdot t$ as a function of the gating time under a gate voltage G_V = -3 V for sample S2. The dotted lines are a guide to the eye.

5.3.2 . X-ray photoelectron spectroscopy (XPS)

In order to probe the changes in the chemical environment of the CoFeB/HfO$_2$ interface, XPS measurements were performed before and after annealing and after exposure to gate voltages. Figure 5.6 shows the XPS spectra of Fe 2p$_{3/2}$ and 2p$_{1/2}$, Co 2p$_{3/2}$ and 2p$_{1/2}$, and O 1s of as-grown, S2 and S2 exposed to -3V for 30 s and 480 s. As shown in Figures 5.6a and 5.6b, the Fe 2p and Co 2p peaks show no significant differences between the as-grown and S2 samples, confirming the metallic nature of Fe and Co before and after annealing, and therefore indicating that PMA in S2 does not originate from the oxidation of the CoFeB/HfO$_2$ interface, as discussed earlier. A similar scenario is observed for O 1s, where minor

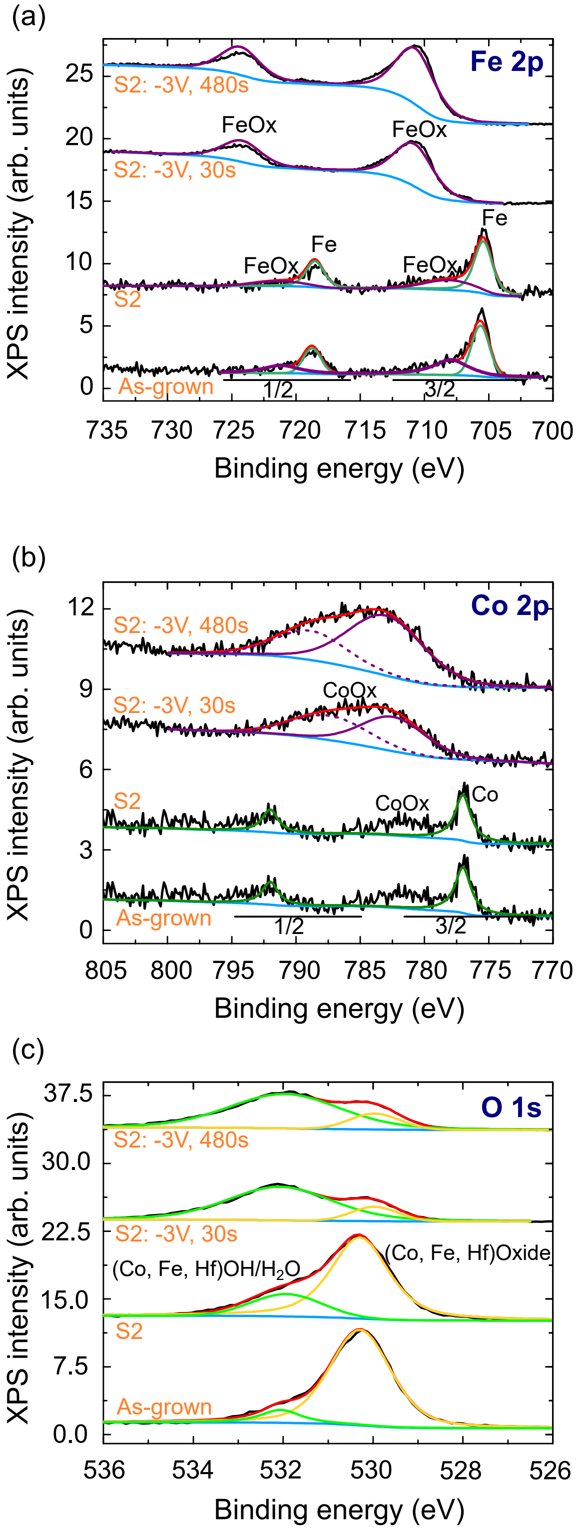

Figure 5.6: XPS spectra of (a) Fe $2p_{3/2}$ and $2p_{1/2}$, (b) Co $2p_{3/2}$ and $2p_{1/2}$, and (c) O 1s for as-grown samples, S2, and S2 exposed to -3V for 30s and 480s. Raw data (black), total fitting (red), fitting of each peak: light green and yellow for O 1s peaks; dark green for Co and Fe 2p, and purple (dashed and solid) for oxides of Fe and Co 2p.

changes are detected before and after annealing. This is well in line with the absence of PMA in the as-grown samples for the entire negative gate voltage range, as shown in Figure 5.4a, which supports a scenario where the properties of the HM/FM interface are key to inducing PMA in this system.

The 2p peaks of Fe and Co shift toward higher binding energies in S2 samples exposed to -3 V, indicating the transition of Fe and Co to higher valence states [35, 151]. In the case of Fe, the presence of Fe oxides such as Fe_2O_3 and Fe_3O_4 is well indicated by the XPS lines at binding energies in the vicinity of 710 eV and 724 eV [152], as shown in Figure 5.6a. Co also shows a strong signature of oxidation with XPS peaks appearing at 782 eV and 790 eV [153]. The XPS O 1s profile shown in Figure 5.6c for the as-grown sample and S2 contains a prominent broad peak near 530 eV and a less pronounced peak near 532 eV. The peak near 530 eV is compatible with the signature of oxygen in HfO_2, and both Fe and Co oxides [152–154]. The peak at higher binding energies becomes dominant after the application of the gate voltage, and can therefore be related to the mobile oxygen species that migrate under the action of the gate voltage. A possible scenario is that this signal corresponds to Fe and Co hydroxide species formed by combination with water molecules from the atmosphere, which have been reported to show XPS peaks near 531-532 eV [152, 153]. This signal can also contain a contribution of non-dissociated H_2O molecules [155].

5.3.3 . Magneto-ionic reversibility

Positive voltages up to +4 V do not produce any significant change in the magnetic state achieved after the application of -3 V in S2. Samples S1 (annealing at 350°C for 1 hr) and S4 (annealing at 390°C with zero dwell time) also show a similar magneto-ionic response as S2 where a negative voltage of -2.5 V irreversibly drives the magnetization from OOP to IP as shown in Figure 5.7. In contrast to pMOKE measurements, two distinct coercive fields are observed in the anomalous Hall effect (AHE) loops for sample S4 as shown in Figure 5.7c. This is because the electrical contacts made to measure the AHE voltage were placed outside the gated area (about 0.25 cm^2 in the center of a 1 x 0.5 cm^2 sample). The measurements have in this case a contribution not only from the gated area, but also from the as-grown materials close to the contacts as shown in the cartoon in Figure 5.7d. Only sample S3 (annealing at 350°C with zero dwell time) showed limited reversibility under positive voltages, as shown in Figure 5.8. This progressive suppression of reversibility is attributed to an increase of thermally induced crystallization in $W/CoFeB/HfO_2$ at higher annealing temperatures and longer annealing times, in analogy to what has been reported for W/CoFeB/MgO systems in the annealing temperature window between 300 and 400°C [156]. In addition, the gate voltage required to reorient the magnetization easy axis from OOP to IP in S3 is -2.3 V, a lower value compared to the -3 V necessary to observe an SRT in S2, for the same

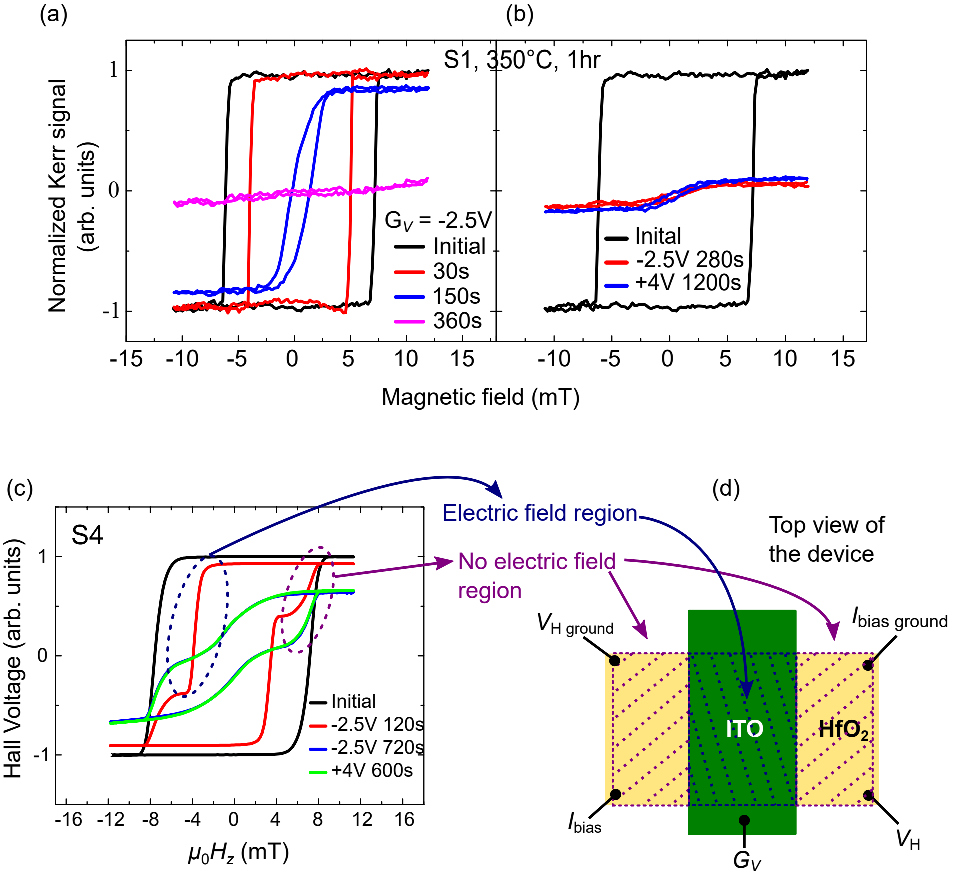

Figure 5.7: pMOKE hysteresis loops showing (a) the evolution of the magnetic anisotropy induced by a gate voltage of -2.5 V applied for different durations, and (b) the degree of reversibility after a gate voltage of +4 V was applied for 1200 s, for sample S1. (c) Anomalous Hall effect hysteresis loops showing the evolution of the magnetic anisotropy induced by a gate voltage of -2.5 V applied for different durations, and the degree of reversibility after a gate voltage of +4 V was applied for 600 s, for sample S4. (d) Top view of the device showing the four contacts used for measuring AHE and the region where the gate voltages were applied.

gating time. This also supports the hypothesis of a more favorable ionic diffusion in samples that are closer to an amorphous state, where ionic conduction channels are not limited to the grain boundaries, as could be expected in granular systems [137].

Although lower annealing temperatures could be explored to achieve full reversibility, the DMI in sample S3, has already been found to be significantly lower than that of S2. The frequency shift measured by BLS is negligible in this sample compared to the shift of about 1 GHz measured at $k = 20\ \mu\text{m}^{-1}$ in S2 as shown in Figure 5.9. This presents the need of a compromise between the magneto-ionic performance and the enhancement of the magnetic properties of the film. DMI is a key aspect in this compromise since it is of critical importance for the de-

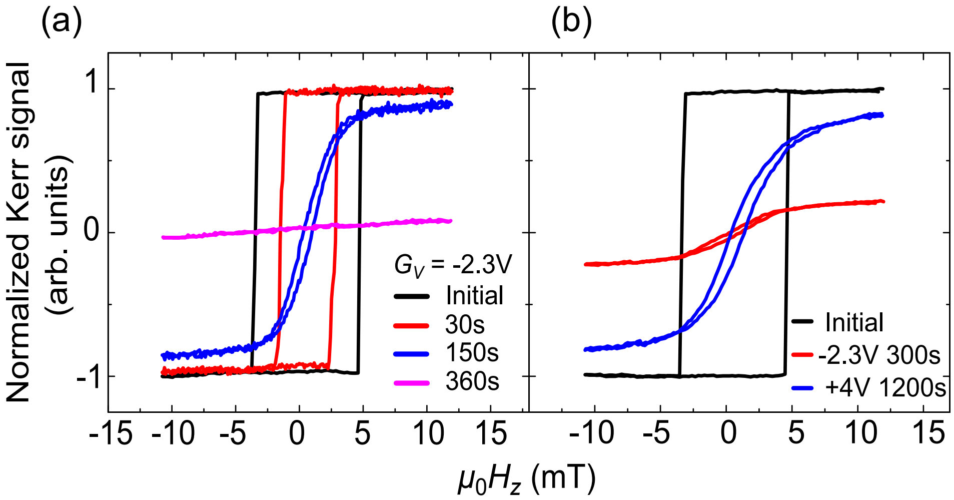

Figure 5.8: pMOKE hysteresis loops measured in sample S3 (350°C, zero dwell time) showing an SRT induced by the exposure to a gate voltage of -2.3 V for a) 360 s, and b) partial reversibility of the IP magnetized state after exposure to +4 V for 1200 s.

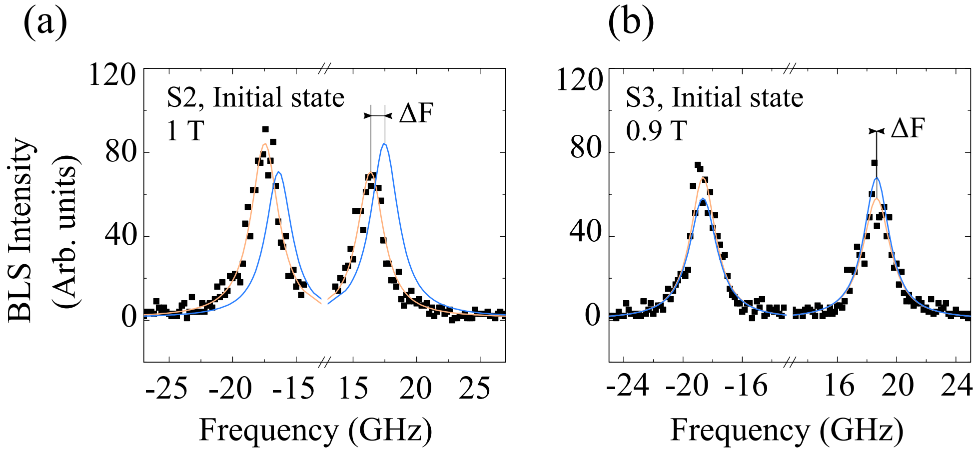

Figure 5.9: BLS spectra showing the frequency asymmetry ΔF of (a) S2, and (b) S3 in their initial states.

sign of materials hosting chiral magnetic structures such as skyrmions and chiral Néel domain walls. These chiral structures offer perspectives for applications in memory devices based on their current-induced motion in nano-devices. Controlling DMI can therefore be used to engineer the optimal DW structure (Bloch to Néel transition) for spin-torque driven domain wall motion [157], which is of high technological relevance.

5.3.4 . Domain wall motion and effective DMI field (H_{DMI})

Chiral Néel domain walls also allow for high magnetic-field-driven domain wall velocities in the flow regime that can scale with the ratio D/M_{s} [158, 159]. In the present case, a maximum velocity plateau is observed and its maximum velocity

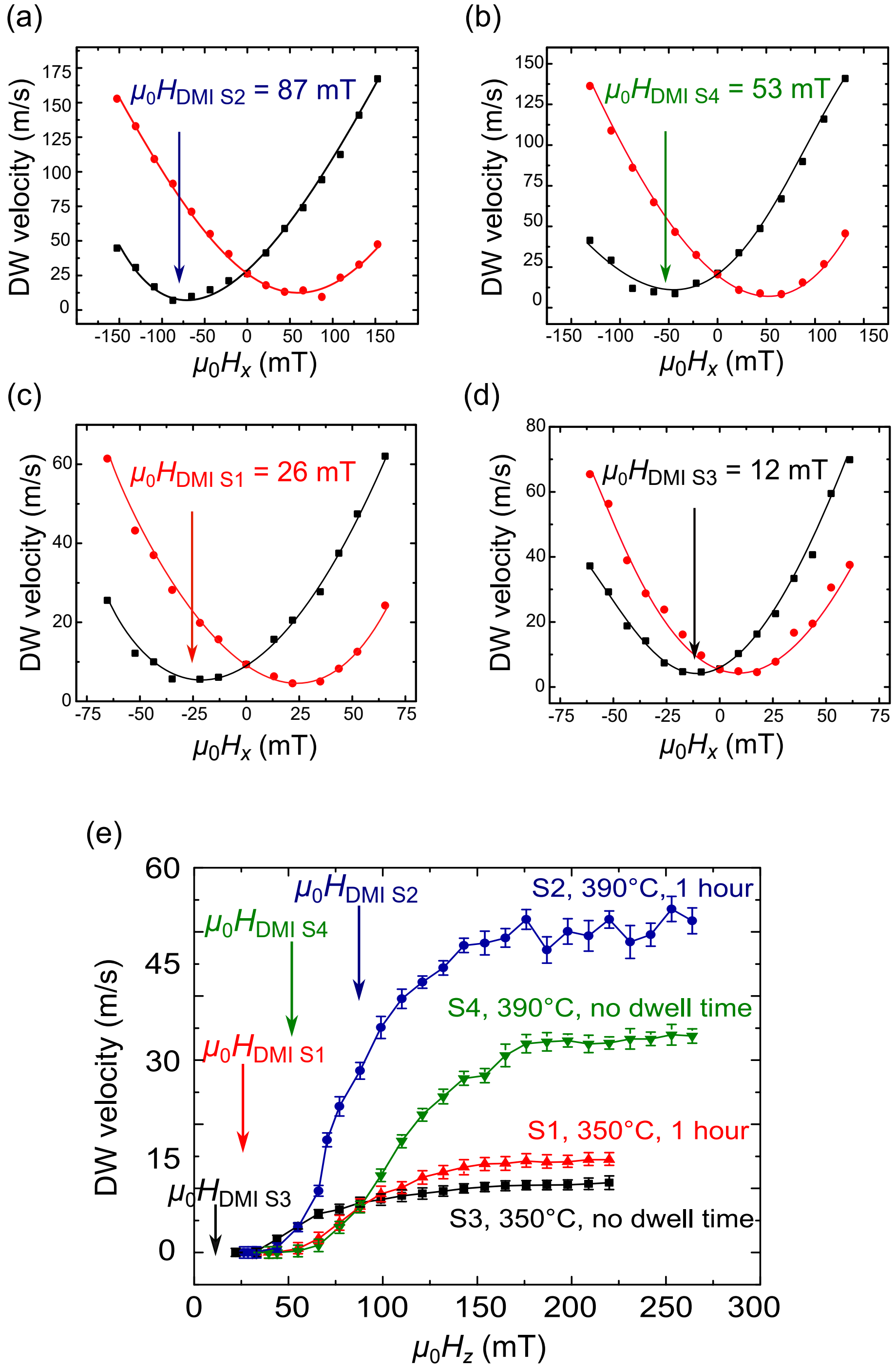

Figure 5.10: (a) Magnetic DW velocity measured under an out-of-plane magnetic field ($\mu_0 H_z$) for samples annealed at 350 and 390°C for 1 h (S1, S2, respectively) and zero dwell time (S3, S4, respectively). The error bars correspond to the standard error over ten measurements on different domains. (b)-(e) Magnetic DW velocity measured under in-plane magnetic fields ($\mu_0 H_x$). Right propagating DWs are shown in red circles and left propagating DWs are shown as black squares. The values of $\mu_0 H_{\mathrm{DMI}}$ are indicated for all samples. Lines correspond to second order polynomial fittings.

value increases with the temperature and the annealing time as shown in Figure 5e. However, a direct correlation between this maximum velocity plateau with the values of D/M_{s} is not straightforward. It has been shown that the velocity plateau that has a relation with D/M_{s} has a high-field limit close to the DMI field $\mu_0 H_{\mathrm{DMI}}$ [159, 160]. The $\mu_0 H_{\mathrm{DMI}}$ values have been measured by asymmetric bubble domain expansion under an in-plane magnetic field ($\mu_0 H_x$) with perpendicular field pulses $\mu_0 H_z$ of 66 mT, 99 mT, 121 mT and 88 mT, for S3, S1, S4 and S2, respectively, and are shown in Figure 5.10a-d. The velocity of right and left propagating DWs are shown as red circles and black squares, respectively. The values of $\mu_0 H_{\mathrm{DMI}}$ correspond to the field at which the minimum velocity is observed, and are 12 $\pm$ 0.5 , 26 $\pm$ 1.3 , 53 $\pm$ 2.6 , and 87 $\pm$ 4.3 mT for S3, S1, S4, and S2, respectively. When these values are confronted with the velocity plots in Figure 5.10a, it is observed that for all the samples studied, the maximum velocity plateau starts at magnetic fields higher than $\mu_0 H_{\mathrm{DMI}}$. Therefore, an analysis within the model described in refs. [159, 160] can not be performed. Although the increase in the maximum velocity plateau could still be qualitatively associated with the increase in the value of D, it should be considered in the context of a simultaneous increase in the crystallinity of the films. The changes in crystallinity and interface disorder can also play an important role in DW dynamics in CoFeB films that can not be accounted for by only considering the changes in magnetization, DMI, and perpendicular anisotropy [131, 161]. The interplay between the changes in DMI and crystallinity add a significant degree of complexity to the interpretation of the DW dynamics in this system, which calls for a dedicated study.

5.4 . Conclusion

In conclusion, we have demonstrated a non-volatile SRT from OOP to IP magnetization and a manipulation of DMI done by means of voltage-controlled ion migration in annealed β-W/CoFeB/HfO$_2$ samples. The disparity in reversibility for different annealing profiles and temperatures has been linked to a difference in the degree of crystallization in W/CoFeB that can greatly affect the density of ionic conduction channels and therefore, the mobility of ions. In addition, we also showed the influence of different annealing conditions on domain wall velocity. These results provide an insight into the magneto-ionic response of systems that require annealing to enhance their magnetic properties such as PMA and DMI and point at the need of a compromise between the enhancement of magnetic properties and the magneto-ionic reversibility. The large and permanent magneto-ionic effects seen in samples annealed at 390°C, exhibiting strong PMA and DMI, can be of interest even in the absence of reversibility. Magneto-ionics can provide in this case a simple post-growth means to fine tune magnetic properties in a local and non-volatile fashion. This could be employed, for example, to facilitate the nucleation of skyrmions [162] or to modulate the spin-orbit torque efficiency in β-W/CoFeB-based spintronics devices.

6 - MAGNETO-IONICS IN Pt/CoFeB/HfO$_2$: EVALUATING THE EFFECTS OF TIME EVOLUTION

In this chapter, the magneto-ionic behavior in Pt/Co$_{60}$Fe$_{20}$B$_{20}$/HfO$_2$ is presented. Similar to Ta/CoFeB/HfO$_2$, this system also shows two magneto-ionic regimes where both regimes I and II are reversible unlike the Ta-system that only showed reversibility in regime II. However, the stability of the nonvolatile magnetic states was found to be significantly different in regimes I and II. Magnetic states in regime I were found to be highly stable, with no significant loss of remanence in the hysteresis loops over several weeks after the gate voltage application. In contrast, the magnetic states in regime II (between OOP and IP) were found to evolve with time back to the OOP state within one day after the application of the gate voltage. In addition, the stability shows a significant dependence on the thickness of the HfO$_2$ layer in which thinner HfO$_2$ shows a substantial improvement in stability over thicker HfO$_2$. This disparity in the stability of the magneto-ionic states in regimes I and II could be attributed to the differences in the binding strength of the oxygen species at the interface and the atmospheric interactions with different thicknesses of HfO$_2$ where thicker HfO$_2$ could have more oxygen "deficient" sites that can intake more oxygen out of CoFeB than thinner HfO$_2$. These results show the importance of studying the link between the ionic mechanisms and the magneto-ionic state stability, in view of practical applications in spintronics.

6.1 . Introduction

The possibility to tune magnetic properties with ion migration is appealing as it allows for generating multiple non-volatile intermediate magnetic states which can be used to develop multi-state magnetic storage device concepts that are analogous to the multiple resistance states used to achieve high density storage in non-volatile resistive random access memory (RRAM) [53, 163, 164]. A key factor is the stability of each magneto-ionic state, as a change in the magnetic state can overlap or change the stored information. However, the time evolution of the magneto-ionic states after removing the gate voltage is largely overlooked in the literature. Only a few studies have shown that significant changes can occur over a timescale of a few seconds in magnetic anisotropy [165] and 2 hours in chirality reversal of skyrmions [44], which is of great importance for the design of robust spintronics devices based on magneto-ionics. Systems based on Pt and/or CoFeB are of great interest in spintronics community due to the strong spin-orbit coupling [166], DMI [167] and large anisotropy [168]; hence a HfO$_2$-based magneto-ionic system is investigated in this chapter.

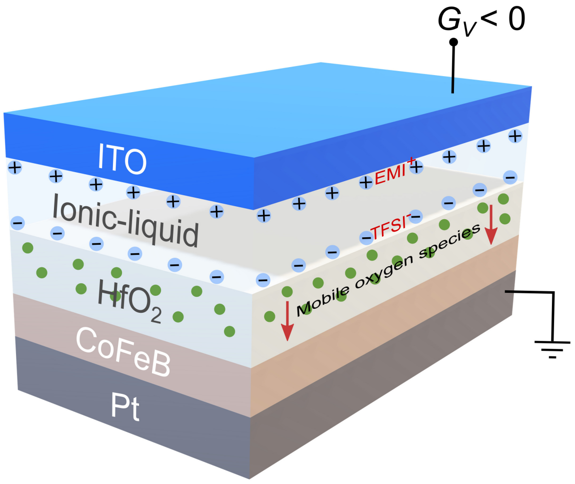

Figure 6.1: A schematic structure of the IL-gated Pt/CoFeB/HfO_2 device showing migration of oxygen species (green dots) in the HfO_2 layer toward the CoFeB layer under a negative gate voltage.

6.2 . Sample preparation and electric field gating

The magnetic stacks Pt (5 nm)/$Co_{60}Fe_{20}B_{20}$ (0.7 nm)/HfO_2 (y nm), where y = 1.5 and 3, used in this study were grown by magnetron sputtering. To implement a gate, approximately 10 μL of ionic liquid [EMI][TFSI] was added to the surface of the magnetic films of dimensions 1 x 0.5 cm^2 in the center covering an area of about 0.25 cm^2. A glass substrate coated with a 100 nm-thick ITO layer was then placed on top of the ionic liquid to use as the top electrode to apply the gate voltages while the magnetic films were grounded. ITO and the voltage source were connected by means of a silver wire, which was glued to an edge of the glass substrate contacting ITO via an electrically conductive epoxy adhesive. Experiments were performed at room temperature on samples cut from the same wafer. A schematic of the device is shown in Figure 6.1.

6.3 . Results: Pt (5 nm)/CoFeB (0.7 nm)/ HfO_2 (3 nm)

6.3.1 . Magneto-ionic regimes

The magnetic stacks in the as-grown state have an in-plane easy axis of magnetization. Under the application of a gate voltage of -3 V to the top ITO, the magnetization easy axis reorients from in-plane to out-of-plane, achieving PMA after 70 s, and longer gating times lead to a second reorientation of the easy axis from out-of-plane to in-plane. As mentioned earlier in this thesis, it is well known that a controlled oxidation/reduction of the ferromagnet/oxide interface can lead to a spin reorientation transition, from in-plane anisotropy to PMA or vice-versa, depending on the degree of oxidation. A similar mechanism is thought to be at play in the present case. Figure 6.2 shows a gradual evolution of the magnetic

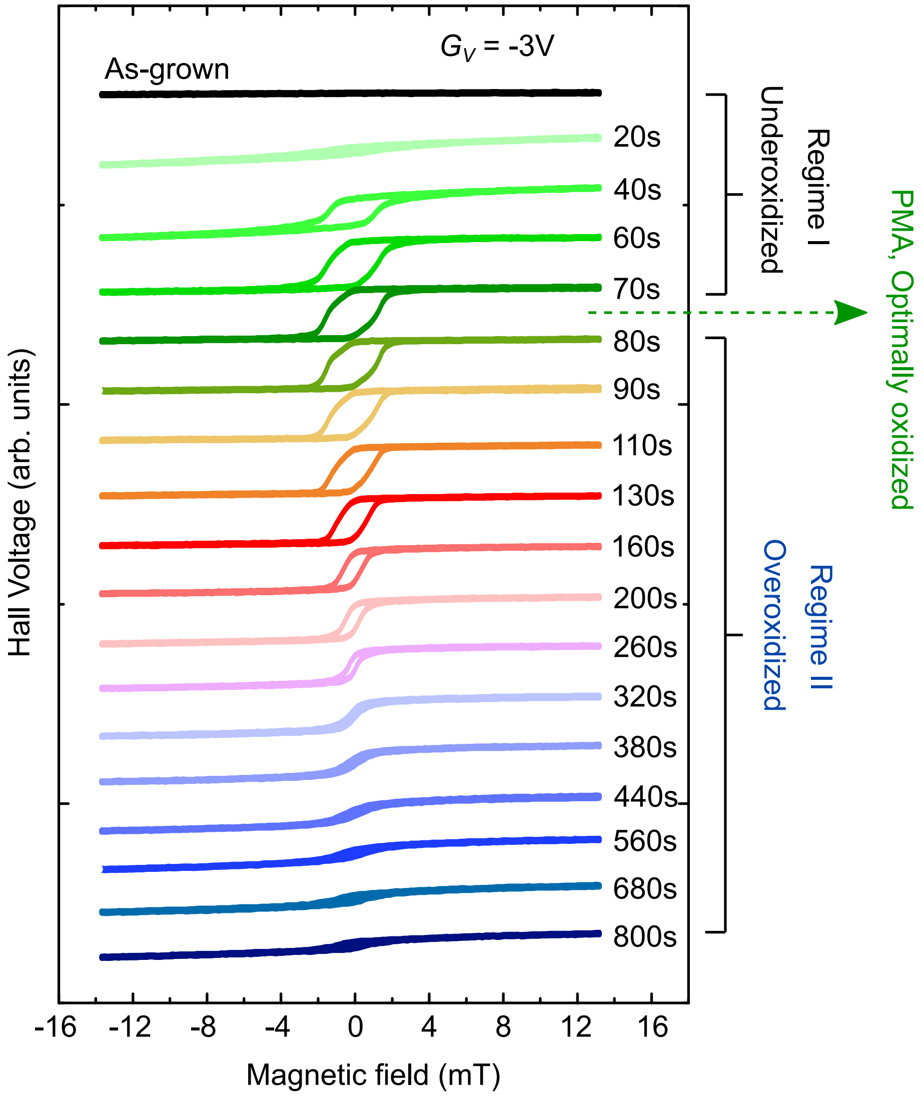

Figure 6.2: A gradual evolution of the magnetic anisotropy in response to a gate voltage of -3 V applied for different durations showing regimes I and II.

anisotropy of an underoxidized as-grown sample exhibiting in-plane anisotropy in response to a gate voltage of -3V applied for different durations. Similar to the Ta/CoFeB/HfO_2 [148] system presented earlier, two regimes, I and II, where a transformation from an underoxidized in-plane anisotropy to an optimally oxidized PMA (regime I) and PMA to an overoxidized in-plane anisotropy (regime II) have been identified in this system. The evolution of the magnetic anisotropy was also recorded at gate voltages of -2.8 V and -2.9 V in order to study the kinetics of regimes I and II. Figure 6.3 shows the modification of the out-of-plane remanence as a function of gating time for -2.8 V, -2.9 V and -3 V. The remanence of the as-grown sample rises under negative gate voltages until PMA corresponding to regime I, followed by a decrease toward an in-plane anisotropy state, corresponding to regime II, where the magneto-ionic process shows a significantly faster response in regime I than regime II. In addition, the speed of the entire process increases as the gate voltage is increased due to a stronger thrust on the mobile oxygen species in the HfO_2 layer. This disparity in the magneto-ionic rates in regimes I and II could be attributed to the difference in the chemical environment of CoFeB in regimes I and II, in which oxidation may be energetically more feasible in regime I than regime II due to the availability of more binding sites.

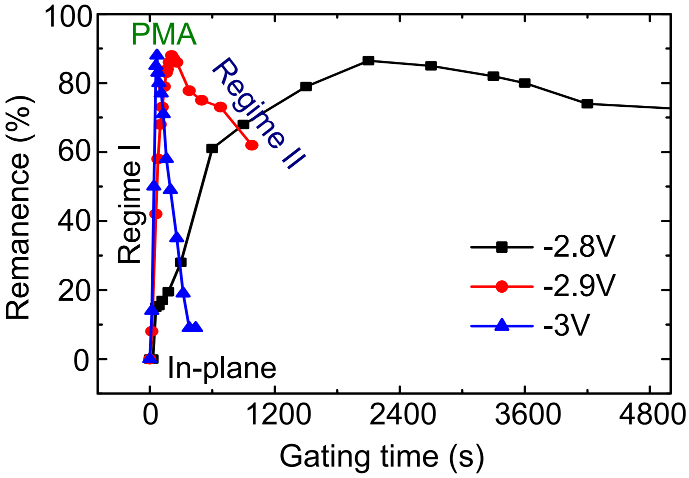

Figure 6.3: Remanence as a function of gating time for as-grown samples under gate voltages of -2.8 V (black squares), -2.9 V (red circles) and -3 V (blue triangles).

6.3.2 . Magneto-ionic reversibility

The magneto-ionic reversibility of the system in regimes I and II has been explored by applying positive gate voltages to as-grown samples exposed to -3 V for 60 s (regime I) and 800 s (regime II) as shown in Figure 6.4. A positive gate voltage of +3.5 V applied for 300 s to the magnetic state in regime II (Figure 6.4c) reverts back to a magnetic state in regime I close to the as-grown state (Figure 6.4d). It is worth mentioning that although similar magneto-ionic systems based on HfO_2 such as $Pt/Co/HfO_2$ [35], $Ta/Co_{20}Fe_{60}B_{20}/HfO_2$ [148] have reported a gate voltage-induced spin reorientation transition from underoxidized in-plane anisotropy to PMA, reversibility was largely suppressed in regime I. However, in the present system, an as-grown sample exposed to -3 V for 60 s (regime I) shows a significant reversibility after applying +3.5 s for 300 s as shown in Figure 6.4e and f. Hence, both regimes I and II are reversible with positive gate voltages. This disparity in reversibility between the current system and $Pt/Co/HfO_2$ [35] and

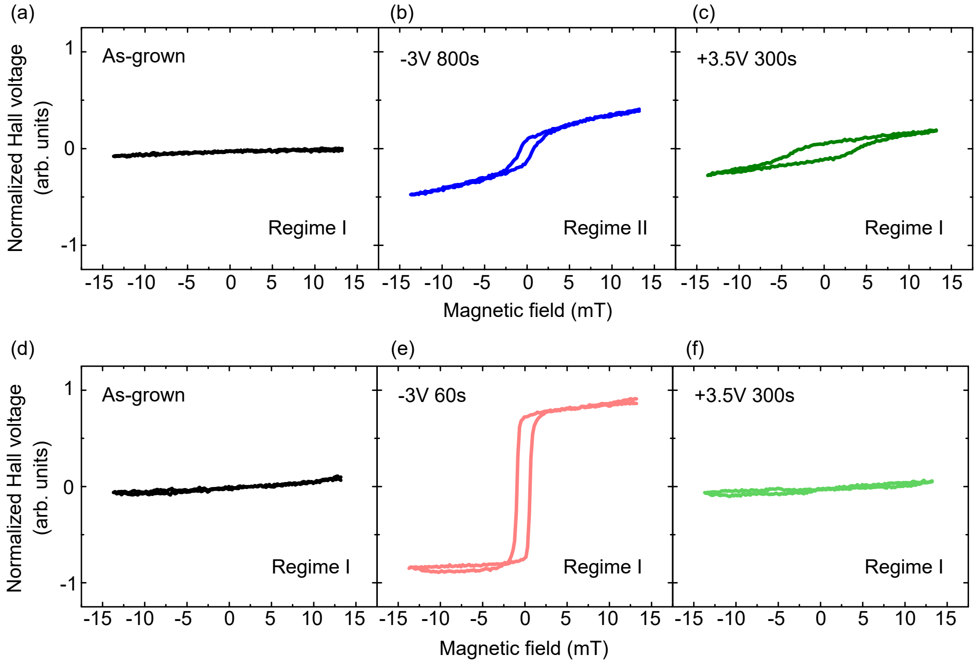

Figure 6.4: AHE hysteresis loops showing the reversibility of the system in regimes I and II. (a) An as-grown sample (b) overoxidized to regime II by applying a negative gate voltage of -3 V for 800 s (c) reverses back to regime I after applying a positive gate voltage of +3.5 V for 300 s. (d) An as-grown sample (e) oxidized within regime I by applying -3 V for 60 s (f) showing a significant recovery after applying +3.5 V for 300 s.

Ta/$Co_{20}Fe_{60}B_{20}$/HfO_2 [148] could be attributed to a weaker binding strength of the oxygen species at the CoFeB interface. Other factors such as the stoichiometry of the CoFeB layer, the thickness of the magnetic layer and the underlayer could also be important.

6.3.3 . Stability of the magneto-ionic states

The stability of the magnetic states in each regime was investigated by recording the hysteresis loops at an interval of one day for up to 35 days. Figure 6.5 shows the hysteresis loops of the samples studied in which as-grown samples were exposed to a gate voltage of -3 V for different times. As-grown samples exposed to -3 V for 20 s and 50 s were studied for the time evolution in regime I (Figure 6.5b and c), an as-grown sample exposed to -3 V for 120 s for PMA (Figure 6.5d), and as-grown samples exposed to -3 V for 180 s and 1320 s for regime II (Figure 6.5e and f). The samples after applying a gate voltage were then stored in atmosphere without the ionic liquid gate. Measurements performed on the samples directly after applying a gate voltage are denoted as Day 0, after one day as Day 1, and so on. As-grown samples used in this study were very stable with time and did not show any change over a period of a few months. Regime I also presents a similar case, where the gate voltage-induced oxidation only shows a marginal change in the magnetic states after 35 days as shown in Figure 6.5b and c. However, the stability of the magnetic states in regime II presents a different scenario, where both overoxidized samples were found to evolve with time. As shown in Figure 6.5e and f, the magnetic states evolve after removing the gate voltage, showing a noticeable change after 1 day, which continues toward a less overoxidized state for 7 days where it stabilizes for at least 27 days. The large evolution in regime II also demonstrates that the optimally oxidized PMA state is a very stable state. As shown in Figure 6.5d, the intial PMA achieved by -3 V applied for 120 s stabilizes a stronger PMA with time and for the sample in regime II achieved by applying -3 V for 180 s (Figure 6.5e), the final evolved stable state assumes a square hysteresis, but with a lower amplitude compared to the gate voltage-induced PMA. The better stability in regime I over regime II could be linked to a difference in the binding strength of the adsorbed oxygen on the CoFeB layer, similarly to what has been proposed for Ta/CoFeB/HfO_2 in previous chapters. While regime I in Ta/CoFeB/HfO_2 remained irreversible due to a potential strong binding of oxygen species, the same regime in Pt/CoFeB/HfO_2 is reversible but also very stable with time. For regime II, in Ta/CoFeB/HfO_2, a reversible behaviour was observed most

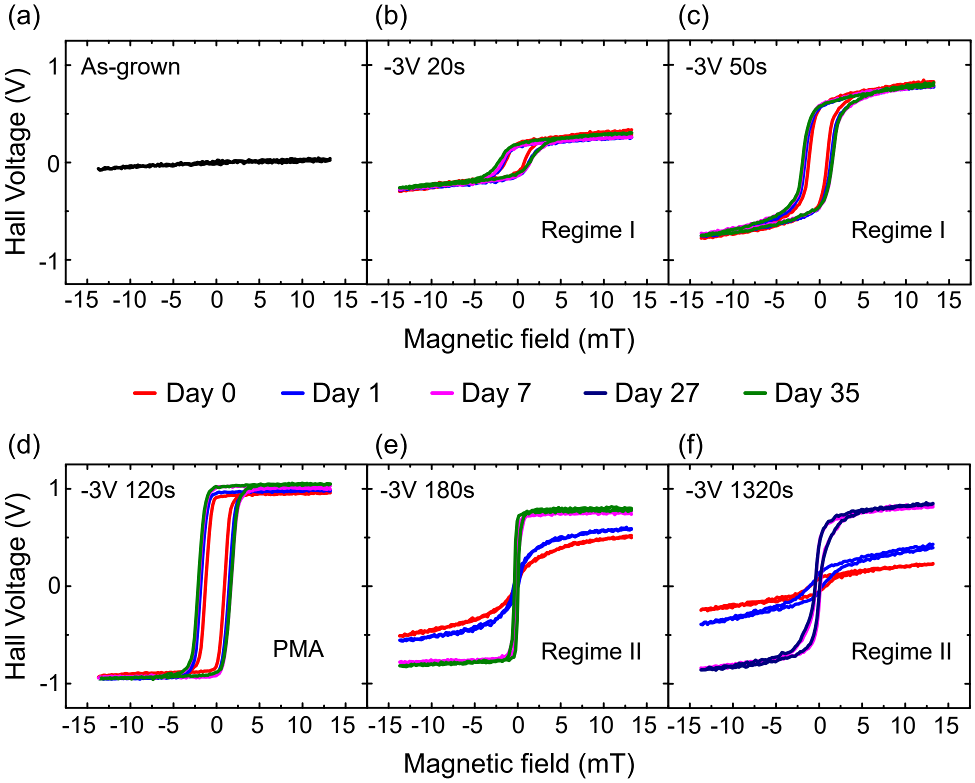

Figure 6.5: AHE hysteresis loops of an as-grown sample (a), and as-grown samples exposed to -3 V for (b) 20 s, (c) 50 s, (d) 120 s, (e) 180 s, and (f) 1320 s showing the time evolution of the magnetic states for up to 35 days.

likely due to a weaker binding of oxygen species, whereas Pt/CoFeB/HfO_2 shows reversibility, but is not stable with time. In addition, Ta/CoFeB/HfO_2 [148] and W/CoFeB/HfO_2 [169] also demonstrated a slower magneto-ionic response in samples immediately after annealing, which showed a faster response after storing the samples in the air for a few days due to the incorporation of mobile oxygen species from air humidity in the HfO_2 layer. Hence, the role of exchanging oxygen species between the stack and the atmosphere could also be very important for the time evolution of the magneto-ionic states. This contribution could be evaluated by reducing the thickness of HfO_2 keeping the other layers constant as thinner HfO_2 is more vulnerable to atmospheric oxidation of the CoFeB layer. In the following, the magneto-ionic behavior of Pt (5 nm)/CoFeB (0.7 nm) with a 1.5 nm-thick HfO_2 top layer is discussed.

6.4 . Results: Pt (5 nm)/CoFeB (0.7 nm)/ HfO_2 (1.5 nm)

6.4.1 . Magneto-ionic regimes and reversibility

The as-grown samples have an in-plane easy axis of magnetization, which, after applying -2 V for 30 s, transforms to out-of-plane, achieving a strong PMA after subsequent application of -2.2 V for 30 s. The PMA then transforms toward in-plane magnetic anisotropy with further application of a negative gate voltage of -2.5 V for 30 s, confirming the presence of regimes I and II as shown in Figure 6.6a-d. In addition, similar to the 3 nm-thick HfO_2 system, this system also shows reversibility in both regimes I and II. As shown in Figure 6.6d-f, the magnetic state achieved by applying -2.5 V for 30 s recovers to a magnetic state close to the optimally oxidized PMA in regime II after applying a positive gate voltage of +3 V for 30 s, which subsequently enters regime I by applying +3.1 V for 390 s. Figure 6.6g shows the reversibility of the system in regime I, where the as-grown state was driven from in-plane anisotropy to PMA by applying -2.1 V for 75 s and back to in-plane anisotropy by applying +3.2 V for 300 s. Figure 6.6h demonstrates such reversibility for 6 cycles. Hence, the 1.5 nm-thick HfO_2 system presents a similar magneto-ionic modulation of anisotropy as the 3 nm-thick HfO_2 system at lower gate voltages.

6.4.2 . X-ray photoelectron spectroscopy (XPS)

XPS measurements were performed to probe the chemical environment of the CoFeB/HfO_2 interface of the as-grown samples before and after exposure to gate voltages. Figure 6.7 shows the XPS spectra of Co $2p_{3/2}$ and $2p_{1/2}$ (Figure 6.7a), Fe $2p_{3/2}$ and $2p_{1/2}$ (Figure 6.7b) of an as-grown sample, an as-grown sample exposed to -2.1 V for 100 s exhibiting PMA (Figure 6.7c) and an as-grown sample reversed to an in-plane state from PMA by applying +3.3 V for 300 s (Figure 6.7d and e). As shown in Figure 6.7a, the as-grown state presents the signature of

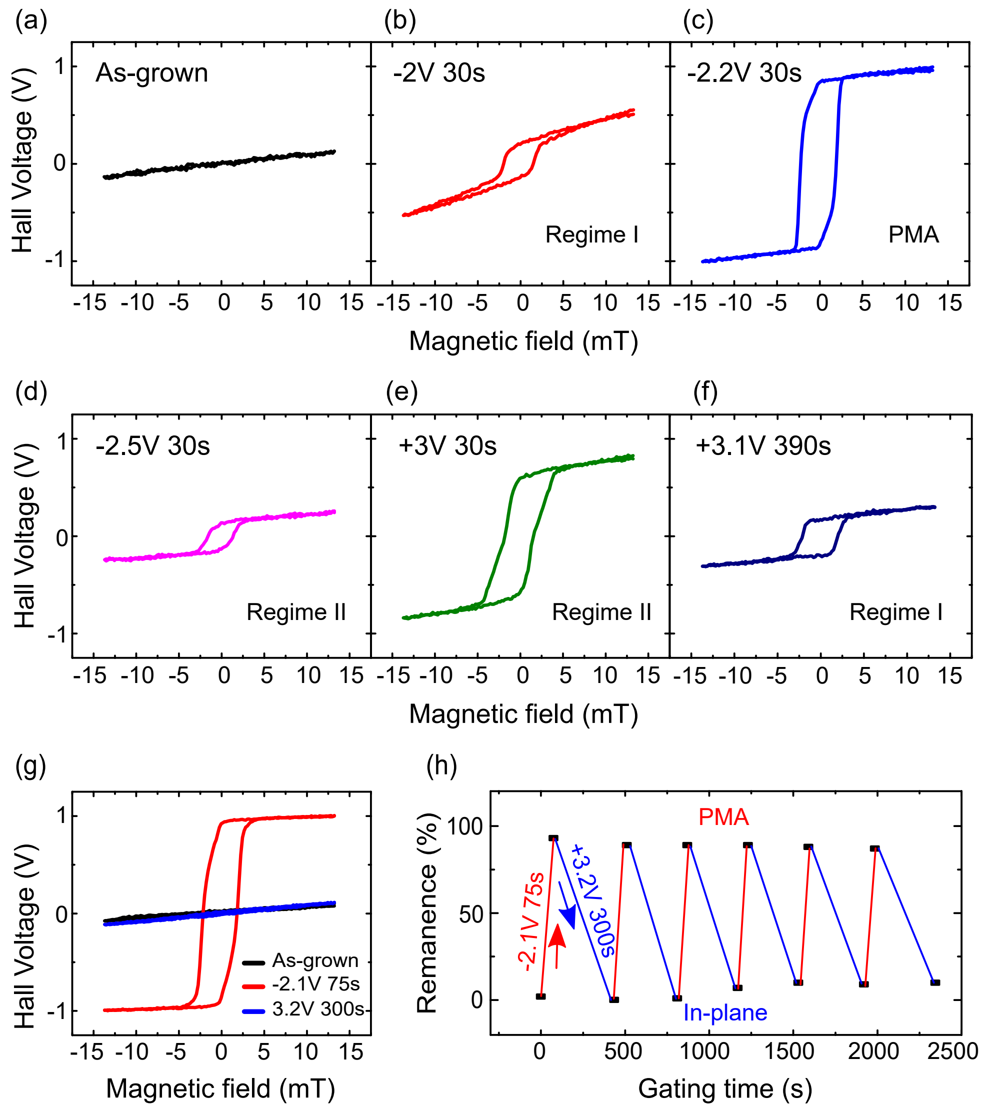

Figure 6.6: AHE hysteresis loops showing the reversibility in regimes I and II of an as-grown sample after applying sequential gate voltages. An as-grown sample (a) achieves PMA through regime I after applying -2 V for 30 s (b) and -2.2 V for 30 s (c), which enters regime II after applying -2.5 V for 30 s (d). Upon applying +3 V for 30 s, a partial reversibility occurs in regime II (e), which extends to regime I after applying +3.1 V for 390 s (f). (g) Reversibility in regime I: an as-grown sample (black line) achieves PMA after applying -2.1 V for 75 s (red line), which reverses back to a magnetic state close to the as-grown state upon applying +3.2 V for 300 s (blue line). (h) Remanence as a function of gating time demonstrating reversibility in regime I for 6 cycles.

metallic Co with a peak at 778 eV. Exposure to a negative gate voltage of -2.1 V for 100 s decreases the intensity of the metallic Co 2p peaks and develops higher binding energy peaks at 780 eV and 794 eV ($2p_{3/2}$), confirming oxidation of the

Co layer. In the case of Fe, the as-grown state shows a less pronounced metallic Fe peak and broad oxide peaks at higher binding energies of 710 eV and 724 eV ($2p_{3/2}$), which after applying -2.1 V for 100 s increases the intensity slightly due to gate voltage-induced oxidation. It may also be noted that a peak at 706 eV in Figure 6.7b arises after exposing to gate voltages. This peak corresponds to In $3p_{3/2}$, which arises due to the contamination from the ITO electrode after gating. Upon application of a positive gate voltage of +3.3 V for 300 s, the XPS profile of Co shows a reduction in the oxide peaks with a partial recovery of the metallic Co and the XPS profile of Fe shows a similar state as the grown state, confirming the observed reversible behavior of the system. It is worth mentioning that the Ta/CoFeB/HfO_2 and W/CoFeB/HfO_2 systems presented in the previous chapters consisted of a Fe-rich $Co_{20}Fe_{60}B_{20}$ where large gate voltage-induced changes were observed in the XPS profiles of Fe. In Pt/CoFeB/HfO_2, $Co_{60}Fe_{20}B_{20}$ is Co-rich, which shows large changes in the XPS profiles of Co and minimal changes in Fe

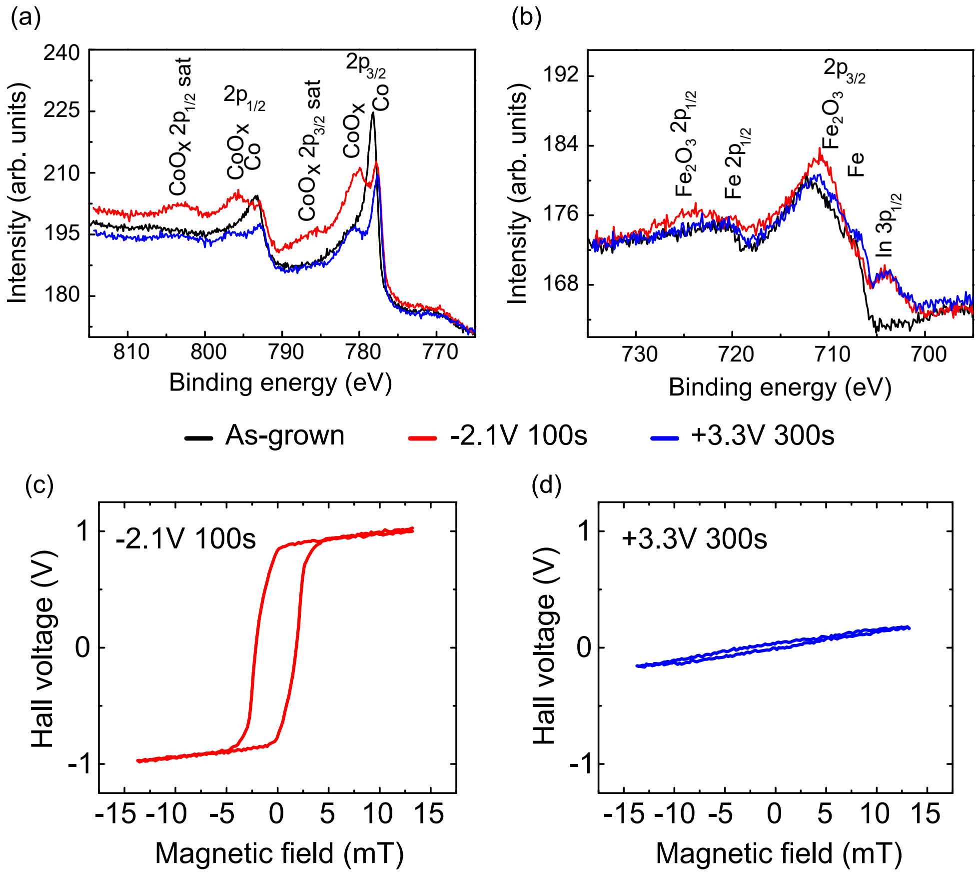

Figure 6.7: XPS spectra of (a) Co $2p_{3/2}$ and $2p_{1/2}$ and (b) Fe $2p_{3/2}$ and $2p_{1/2}$ of an as-grown sample (black), an as-grown sample exposed to -2.1 V for 100 s exhibiting PMA (red) and an as-grown sample reversed to in-plane state from PMA by applying +3.3 V for 300 s (blue). (c, d) The corresponding AHE hysteresis of the samples.

after gate voltage application indicating the very little contribution of Fe as shown in Figure 6.7b. This may be a factor that is important for the observed reversible behavior in regimes I and II in Pt/CoFeB/HfO_2 in contrast to only regime II in Ta/CoFeB/HfO_2.

6.4.3 . Stability of the magneto-ionic states

The stability of the magnetic states in each regime was studied by recording the hysteresis loops at an interval of one day for up to 21 days. Figure 6.8 shows the hysteresis loops of the samples studied in which as-grown samples were exposed to a gate voltage of -2.1 V for different times. As-grown samples exposed to -2.1 V for 25 s and 60 s were studied for the time evolution in regime I (Figure 6.8b and c), an as-grown sample exposed to -2.1 V for 100 s for PMA (Figure 6.8d), and as-grown samples exposed to -2.1 V for 460 s and 910 s for regime II (Figure 6.8e and f). The samples were prepared and stored the same way as the 3 nm-thick HfO_2 system. It is worth mentioning that the as-grown samples, despite the thickness of the HfO_2 layer, were very stable with time and did not show any change over a period of a few months. Regime I and PMA also presents a similar behavior, where the gate voltage-induced oxidation only induces minor differences in the

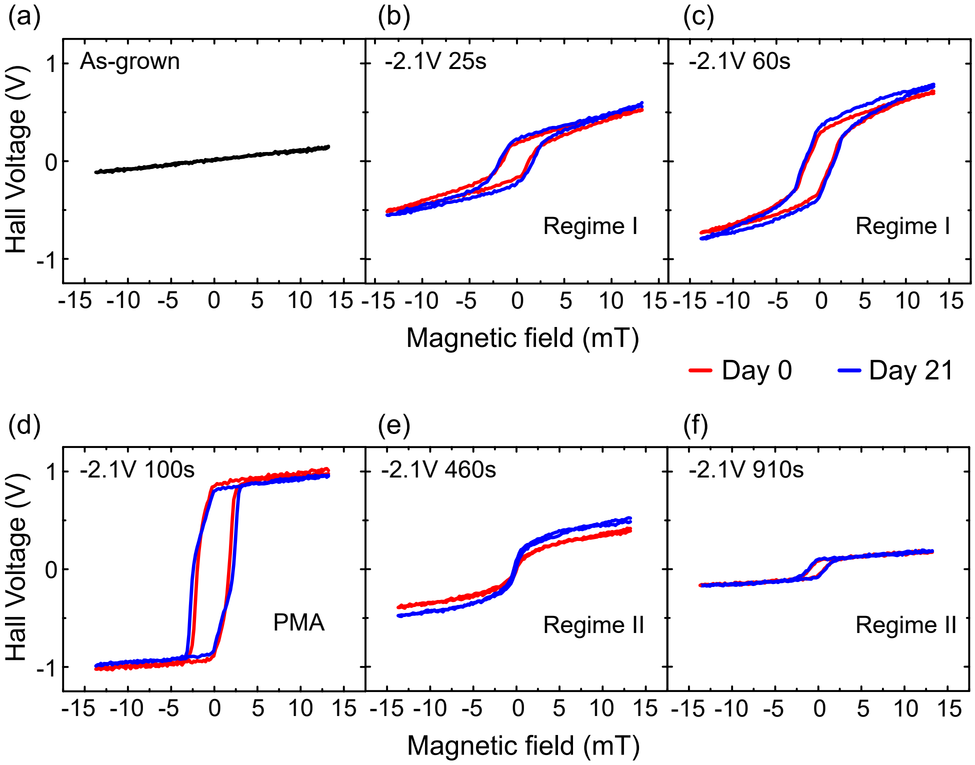

Figure 6.8: AHE hysteresis loops of an as-grown sample (a), and as-grown samples exposed to -2.1 V for (b) 25 s, (c) 60 s, (d) 100 s, (e) 460 s, and (f) 910 s showing the time evolution of the magnetic states for up to 21 days.

magnetic states after 21 days as shown in Figure 6.8b-d. However, the stability of the magnetic states in regime II presents a different scenario with respect to the 3 nm-thick HfO_2 system. An as-grown sample exposed to -2.1 V for 460 s (Figure 6.8e) showed only a slight evolution toward a less overoxidized state and a more overoxidized state (Figure 6.8f) showed almost no change after 21 days. It may be noted that the direction of evolution of magnetic anisotropy in both regimes and systems is toward an optimally oxidized state indicating that PMA is a very stable state. This disparity in the stability of magneto-ionic states in 1.5 nm and 3 nm-thick HfO_2 systems could be linked to a difference in the ease of migration of the oxygen species at the interface between CoFeB and HfO_2 and is discussed in the following section.

6.5 . Discussion

The results presented in the previous sections, where an observed difference in the stability of the magneto-ionic states in regimes I and II for different thicknesses of the HfO_2 layer, can be explained by analyzing the mobile oxygen species in the HfO_2 layer. Studies in the literature have demonstrated adsorption and dissociation of H_2O on HfO_2 surfaces creating hydroxyl (OH-) groups [122, 123, 170–172] that are bound to the Hf atoms because of the large electropositivity of Hf. In addition, the presence and migration of oxygen species in HfO_2 have also been experimentally demonstrated under a gate voltage in Pt/Co/HfO_2 [35], Ta/CoFeB/HfO_2 [148] and W/CoFeB/HfO_2 [169] systems. Figure 6.9 shows a graphic representation of a Pt/CoFeB/HfO_2 magnetic stack before and after exposure to an atmosphere containing moisture (H_2O). When an as-grown sample is exposed to the atmosphere (Figure 6.9a), adsorption of moisture most likely creates a concentration gradient of mobile oxygen species (OH- group) in the HfO_2 layer with a high concentration on the surface of HfO_2 and a low concentration at the interface between CoFeB and HfO_2 as shown in Figure 6.9b. Hence, the Hf atoms near the interface with CoFeB have less oxygen species (oxygen "deficient" sites) than the Hf atoms on the surface of HfO_2.

The proposed mechanism of the time evolution of the magneto-ionic states is depicted in Figure 6.9c-e for 3 nm-thick HfO_2 and in Figure 6.9f-h for 1.5 nm-thick HfO_2. Before exposure to a negative gate voltage ($G_V < 0$), the oxygen species gradient in the HfO_2 layers is such that there are more oxygen "deficient" sites at the CoFeB/HfO_2 interface in the 3 nm system (Figure 6.9c) than the 1.5 nm system (Figure 6.9f). When a negative gate voltage is applied, the front of the mobile oxygen species in the HfO_2 layer moves toward the interface increasing the interaction between oxygen species and the CoFeB layer. In the case of regime I, the stable magneto-ionic states found after the gate voltage is switched off indicate that the oxygen species interacting with the CoFeB may have a relatively

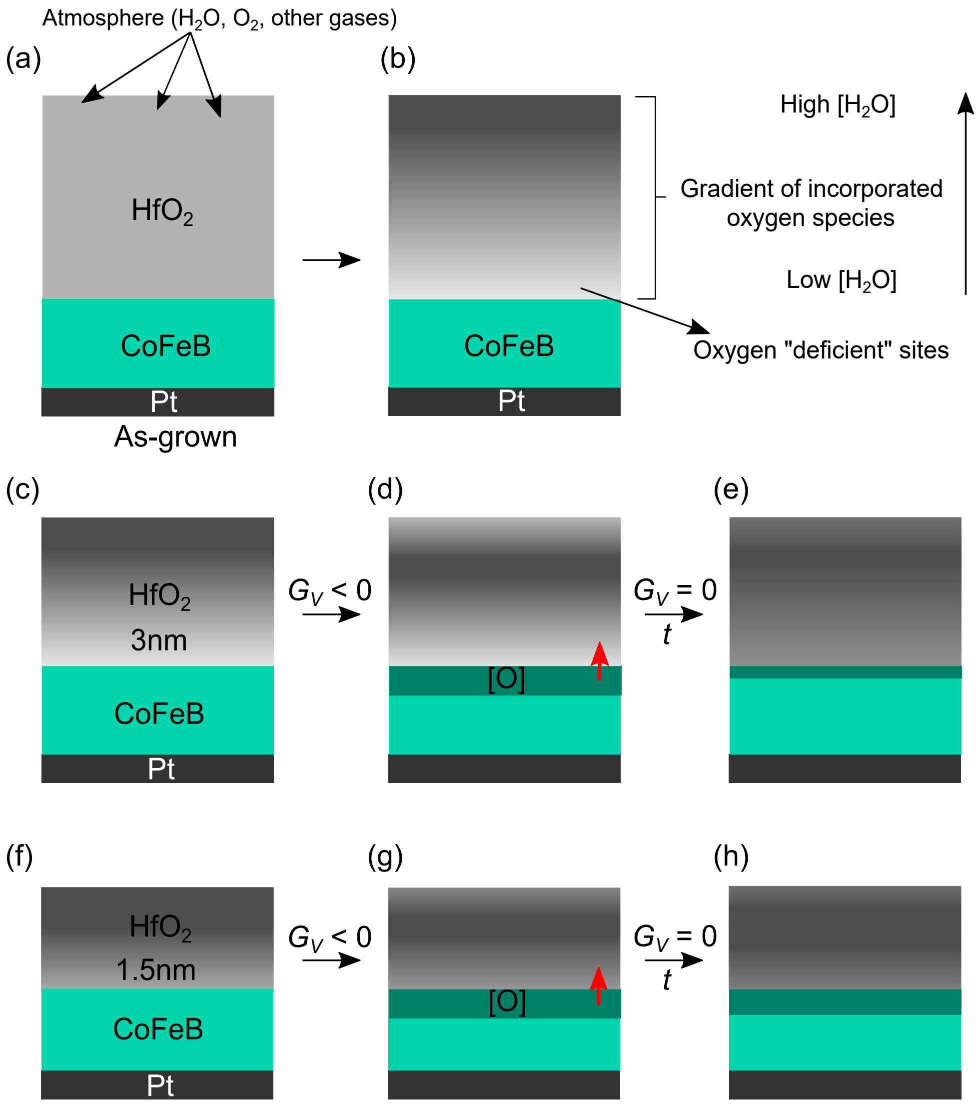

Figure 6.9: Proposed mechanism for the time evolution of the magnetic states. An as-grown sample (a) exposed to air incorporates H_2O in the HfO_2 layer developing a gradient of the incorporated oxygen species with a high concentration on the surface and a low concentration at the CoFeB/HfO_2 interface inducing oxygen "deficient" sites (b). Upon application of a negative gate voltage ($G_V < 0$), the front of the mobile oxygen species in the HfO_2 layer moves toward the CoFeB/HfO_2 interface oxidizing the CoFeB layer. After removing the gate voltage, the weakly bound oxygen species on the CoFeB layer moves to the oxygen "deficient" sites in the HfO_2 layer achieving an equilibrium state. A schematic process of achieving an equilibrium state after applying a negative gate voltage to an as-grown sample of 3 nm-thick HfO_2 layer is shown in (c-e) and 1.5 nm-thick HfO_2 layer is shown in (f-h).

high binding energy, as proposed for Ta/CoFeB/HfO_2 [148], which prevent them from migrating back toward the oxygen "deficient" sites once the gate voltage is switched off. However, in regime II, when the gate voltage is switched off, the weakly bound oxygen species at the interface with CoFeB could migrate back into the HfO_2 layer and away from the CoFeB interface, toward a more oxygen deficient region until an equilibrium state is achieved. Assuming that the 3 nm-thick HfO_2 has more oxygen "deficient" sites at the interface with the CoFeB with respect to the 1.5 nm-thick HfO_2 layer, more oxygen species driven to the CoFeB interface by the gate voltage are expected to migrate back into the HfO_2 layer, reverting significantly the magneto-ionic effects. This is well in line with the results presented above, where the observation of almost no evolution in Figure 6.8f for the 1.5 nm-thick HfO_2 layer could be due to the larger density of oxygen species in the vicinity of the CoFeB/HfO_2 interface, reabsorbing less of the oxygen species driven to the CoFeB/HfO_2 interface through gating.

6.6 . Conclusion

In conclusion, Pt/CoFeB/HfO_2 shows two magneto-ionic regimes in response to a gate voltage-induced oxidation of the CoFeB layer. The regimes I and II correspond to a transition from an underoxidized state exhibiting IPA to an optimally optimized state exhibiting PMA (regime I) and a transition from an optimally oxidized state exhibiting PMA to an overoxidized state exhibiting IPA (regime II), respectively. Both regimes show reversibility, however, the magneto-ionic states in regime I shows a significantly better stability than the magneto-ionic states in regime II, which were found to evolve with time. In addition, the stability shows a large dependence on the thickness of the HfO_2 layer in which thinner HfO_2 shows an improved stability over thicker HfO_2. This disparity in the stability of the magnetic states in regimes I and II and thicknesses of HfO_2 is proposed to be the result of the binding strength of the oxygen species at the CoFeB/HfO_2 interface and the difference in the availability of the oxygen "deficient" sites near the interface. The results presented in this chapter introduces a system that shows reversibility in both regimes and reveal the significance of time evolution of the magneto-ionic states with a method to improve them.

CONCLUSION AND OUTLOOK

Magneto-ionics is an emerging field of study that focuses on the interaction between ions and magnetism in materials where the ions are migrated using a gate voltage. Magneto-ionics has the potential to develop energy-efficient spintronics devices as it allows for non-volatile magnetic states. However, as with any emerging field, there are several challenges that must be overcome to advance research in magneto-ionics. Some of the main challenges include:

1. Lack of understanding of the role of interfacial chemistry of the magnetic interfaces on the reversibility of the process and the underlying physical mechanisms. This makes it difficult to design and optimize materials for specific applications.

2. Designing and synthesizing materials with the desired properties for specific applications. For instance, amorphous and crystalline magnetic thin films and how enhancing magnetic properties of an amorphous magnetic thin film via thermal annealing impacts magneto-ionic performance. This requires a deep understanding of the role of magnetic interfaces and ion mobility in amorphous and crystalline systems.

3. Magneto-ionics involves complex interactions between ions and materials in which the stability of the magnetic states with time needs to be addressed for the development of spintronics devices applications.

This thesis focuses on magneto-ionic modulation of magnetic properties in magnetic heterostructures for the development and understanding of non-volatile magnetic states. Magneto-ionics was demonstrated in heterostructures of heavy metal/ferromagnet/oxide grown by magnetron sputtering. In the interest of developing systems with large and stable PMA, CoFeB was chosen as the ferromagnet and HfO_2 as the ion conducting oxide where oxygen species have been demonstrated to migrate under the application of voltages. In order to apply gate voltages, ionic-liquid gating was utilized, which allowed for applying high electric fields over large surface areas, allowing for characterizing gate voltage-induced changes in magnetic properties easily before transferring to solid state devices, making it a distinctive approach.

Magneto-ionics in CoFeB/HfO_2 thin films with different heavy metal buffer layers and stoichiometry of CoFeB, where CoFeB and HfO_2 are amorphous in the as-grown state, were investigated in order to address the above-mentioned challenges to develop efficient magneto-ionic devices. Magneto-ionic effects were first explored in Ta/CoFeB/HfO_2, where the conventional charge-based VCMA effects in the archetypal Ta/CoFeB/MgO have reported significant changes in magnetic properties. The results interpreted were then used to advance magneto-ionics in W/CoFeB/HfO_2 followed by Pt/CoFeB/HfO_2. The major accomplishments of this thesis are listed below:

All as-grown systems have an underoxidized CoFeB/HfO_2 interface that exhibits IPA. Upon gate voltage-induced oxidation in all as-grown samples, only Ta/CoFeB/HfO_2 and Pt/CoFeB/HfO_2 showed a change in magnetic anisotropy, with the underoxidized IPA state first transforming to perpendicular magnetic anisotropy (PMA) and then back to IPA with further gate voltage application. However, for W/CoFeB/HfO_2, thermal annealing was a necessary step to attain PMA as interfacial oxidation of as-grown samples did not produce PMA. These findings strongly suggest that the interfacial origin of PMA is due to O 2p–(Co,Fe) 3d hybridization at CoFeB/HfO_2 for Ta/CoFeB/HfO_2 and Pt/CoFeB/HfO_2, and W 5d–(Co,Fe) 3d hybridization for W/CoFeB/HfO_2. In addition, a full magneto-ionic reversibility was only observed in Pt/CoFeB/HfO_2, which was designed based on the insights gained from magneto-ionic gating in Ta/CoFeB/HfO_2 and W/CoFeB/HfO_2.

In Ta/CoFeB/HfO_2, two magneto-ionic regimes, namely regime I (IPA→PMA transition) and regime II (PMA→IPA transition), were discerned. Regime I was found to be faster than regime II, but magneto-ionic reversibility was only observed in the regime II. This coexistence of reversible and irreversible regimes in the same system could be likely due to the changes in the oxidation states of Fe, highlighting the critical role of interfacial chemistry in magneto-ionic reversiblity. In addition, the entire IPA→PMA→IPA process was found to be slower after thermal annealing, pointing out its effect on ion mobility. This concept was extensively studied and used to improve magnetic properties and the magneto-ionic reversibility in annealed W/CoFeB/HfO_2, where thermal annealing was a necessary step to attain PMA, which could be driven to IPA with gate voltage-induced oxidation. Since annealing is expected to crystallize CoFeB and improve interfaces, magnetic properties were shown to enhance with higher temperature annealing. However, ion mobility was found to be highly hindered in samples annealed at higher temperatures due to the improved crystallization of CoFeB or, in other words, due to the reduction of grain boundary in CoFeB that serves as ion conduction channel, impeding magneto-ionic reversibility.

Hence, the magneto-ionic process was found to be faster and more reversible in the amorphous state of CoFeB than in the crystallized state. In addition, Fe-dominant CoFeB could potentially induce partial irreversibility that is likely due to the formation of stable Fe oxidation states. This led to the conclusion that an amorphous CoFeB with less Fe combined with a buffer layer that offers strong spin orbit coupling would be desirable for faster magneto-ionic gating and reversibility. This led to Pt/$Co_{60}Fe_{20}B_{20}$/HfO_2. In Pt/CoFeB/HfO_2, both regimes were found to be reversible, where major changes in oxidation and reduction were observed in Co using XPS. However, the stability of the magneto-ionic states with time was found to be significantly more stable in regime I than regime II. In addition, the stability also showed a marked dependence on the thickness of the HfO_2 layer, where thinner HfO_2 demonstrates improved stability in regime II. This disparity in the stability of the magnetic states in regimes I and II and different thicknesses of HfO_2 has been linked to the binding strength of the oxygen species at the CoFeB/HfO_2 interface and the availability of the oxygen "deficient" sites generated by the Hf atoms at the interface, respectively.

The findings elucidated within this thesis highlights the multifaceted nature of magneto-ionics in a diverse array of systems, showcasing the significance of interfacial chemistry, amorphous and crystalline nature and composition of the magnetic stack, and the stability of non-volatile magnetic states. These accomplishments include gaining a deeper understanding of the complexities of magneto-ionics, as well as identifying potential strategies for improving the efficiency of magneto-ionic devices.

Research in magneto-ionics is still in its primal stages, but it holds great promise for the future. Through a comprehensive exploration of the complexities of magneto-ionics, this thesis opens up exciting new possibilities for the future of spintronics research and application, particularly in neuromorphic computing. It is well known that the field of artificial intelligence is rapidly developing, as it enables machines to learn and perform human-like tasks. The rise in the interest of artificial intelligence also involves an enormous usage of computational processing and memory. The modern computers use an architecture known as von Neumann architecture, in which the data storage and processing units are physically separated. Hence, the large amounts of data involved in artificial intelligence need to be transferred back and forth between the data storage and processing units in order to perform a task, costing a significant amount of energy. In modern computers, most of the energy consumed to perform such a task is only from data transfer between the two processing units. A solution to this challenge is by integrating both the units together, similarly to a human brain, in which neurons are the processing units that are interconnected via synapses (memory storage units) with synaptic weights [173]. Neuromorphic computing, also known as adaptive or cognitive computing, is such a brain-inspired approach on the hardware level. It has been demonstrated that the multiple non-volatile resistance states in a resistive random access memory (memristor) can be used to update the synaptic weights in a neuromorphic circuit [174,175]. This concept could be used to develop analogous energy-efficient magnetic systems in which magneto-ionic systems presented earlier can assist in generating multiple intermediate non-volatile magnetic states for synaptic weights. In addition, the time evolution of the magnetic states observed in Pt/CoFeB/HfO_2 can be used to imitate the neuromorphic learning or forgetting functions without any applied gate voltage, which can also be reinitialized once the computation is complete. Moreover, the systems could also be studied for generating skyrmions, in which case both magneto-ionic and skyrmion-based neuromorphic device can be realized in a single device.

In favor of developing energy-efficient SOT devices, W/CoFeB/HfO_2 could be of great importance due to its large spin hall angle. As mentioned earlier in 2.5.6, magneto-ionic reversal of SOT has been demonstrated in Pt/Co/GdO_x. A careful stack engineering of the current β-W/CoFeB/HfO_2 could be used to enhance the magnitude of the spin accumulation in addition to the SOT reversal. In addition, the electric field-tuning of DMI in W/CoFeB/HfO_2 could also potentially host and modify chiral magnetic structures such as Néel domain walls and skyrmions for the development of racetrack memory. Moreover, magneto-ionic modulation of magnetic properties can be explored in the α-W and $(\alpha+\beta)$-W in order to best suit the requirements. The Pt/CoFeB/HfO_2 system presented in the last chapter, in addition to two regimes, also shows reversibility in both regimes, which could be used to develop a fast domain wall or skyrmion racetrack device that can also be a logic gate by arranging gates in a periodic manner, thanks to the large spin-orbit coupling and DMI of Pt/CoFeB. In addition, the reversibility of several magnetic properties such as DMI and damping parameter and the dependence of reversibility on the stoichiometry of CoFeB can also be explored. Moreover, the method proposed to improve the magneto-ionic stability could be implemented in developing devices that can host stable skyrmions.

RÉSUMÉ EN FRANÇAIS

Introduction et motivation

Le déclenchement du magnétisme par champ électrique est une solution novatrice qui permet de contourner les principaux problèmes liés à la réduction de l'échelle des dispositifs spintroniques tout en conservant une stabilité thermique élevée et de bonnes perspectives de fonctionnement à faible puissance. La géométrie du dispositif nécessaire pour une telle technique est celle d'un condensateur, où l'une des plaques est la couche magnétique, qui n'a besoin que d'énergie pour se charger. Le principe général du contrôle du magnétisme par le champ électrique est la modification de l'anisotropie magnétique d'un matériau magnétique par le champ électrique, en raison des changements de la densité électronique proche du niveau de Fermi, par exemple la densité d'électrons $3d$ dans les ferromagnétiques [21]. Le concept de l'influence des champs électriques sur le magnétisme a été exploré pour la première fois sur le plan théorique dans [22–24], où l'on a constaté que les énergies d'anisotropie magnétocristalline dépendaient du remplissage de bande dans des matériaux tels que le Co, le Ni et le Fe [24]. La première démonstration expérimentale de la manipulation des propriétés magnétiques par un champ électrique a été rapportée en 2000 [25] dans un semi-conducteur magnétique dilué (In,Mn)As. Dans ce système, il a été démontré qu'une tension négative appliquée augmentait la concentration de trous qui renforçait l'interaction ferromagnétique entre les ions Mn, tandis que les tensions de grille positives avaient un effet opposé [25]. Depuis lors, un grand nombre de travaux ont vu le jour et se sont concentrés sur l'influence des champs électriques sur les matériaux magnétiques [26]. Les effets du champ électrique sur le magnétisme des métaux ont été démontrés et rapportés pour la première fois en 2007 pour des films minces de FePt et FePd [27]. Dans cette étude, un changement de la coercivité du FePt et du FePd à température ambiante a été signalé pour une tension de grille appliquée, en raison de la formation d'une double couche électrique qui a servi de médiateur à l'accumulation/appauvrissement des charges de surface, comme le montre la figure 6.10 [27].

Les effets des charges sur les propriétés magnétiques se sont révélés être un outil très efficace pour contrôler la transition de phase magnétique [25], l'anisotropie magnétique perpendiculaire (PMA) [21], le pinning et les vitesses des parois de domaine [28,29], l'interaction Dzyaloshinksii-Moriya (DMI) [30,31], les skyrmions [32] et réduisent considérablement la densité de courant de commutation du MTJ [33]. De plus, récemment, une architecture de dispositif qui combine STT, et SOT avec VCMA a été rapportée pour améliorer le temps de commutation [6,34]. Il convient de mentionner que la région la plus accessible pour générer les changements de

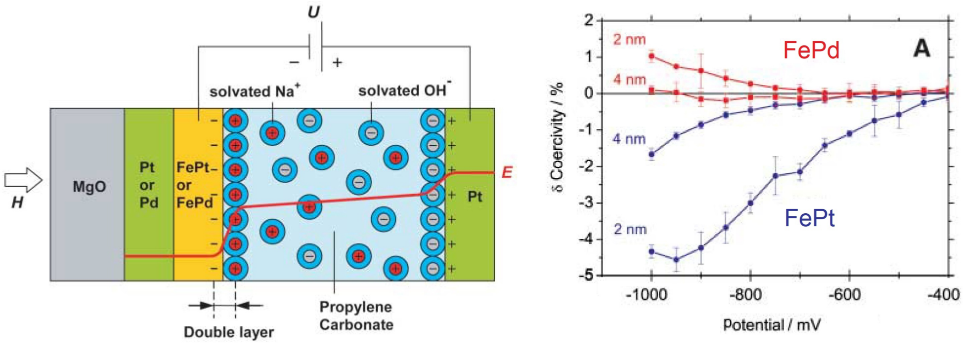

Figure 6.10: Schéma du déclenchement électrolytique d'un film de FePt ou FePd montrant la formation d'une double couche électrique sous un potentiel appliqué U (à gauche). Changements de la coercivité du FePd (rouge) et du FePt (bleu) en fonction du potentiel appliqué pour différentes épaisseurs de films (droite). Adapté de [27].

champ électrique dans la densité électronique est la surface d'un matériau magnétique, d'où la nécessité d'un rapport surface/volume important.

En plus des effets classiques d'accumulation de charges, les champs électriques peuvent également être utilisés pour induire la migration des ions à l'intérieur d'un oxyde à l'interface avec une couche ferromagnétique. Cette migration ionique induite par la tension de grille et l'interaction subséquente avec un matériau magnétique ont été rapportées pour montrer un effet plus étendu sur l'ensemble de la couche magnétique, y compris la deuxième interface d'une couche magnétique mince [35], et peut également fournir la non-volatilité [36], résolvant la volatilité de la charge et l'écran électrostatique [37] dans les ferromagnétiques. Cette technique, où la modulation des propriétés magnétiques est obtenue par la migration des ions vers/hors de l'interface magnétique à l'aide d'une tension, est connue sous le nom de magnéto-ionique [38]. Le déclenchement magnéto-ionique a suscité un grand intérêt ces dernières années en raison de la possibilité d'une modulation importante et non volatile du magnétisme et de l'efficacité magnéto-électrique extrêmement importante de l'ordre d'environ 5000 fJ/Vm [38]. Ceci est très prometteur pour

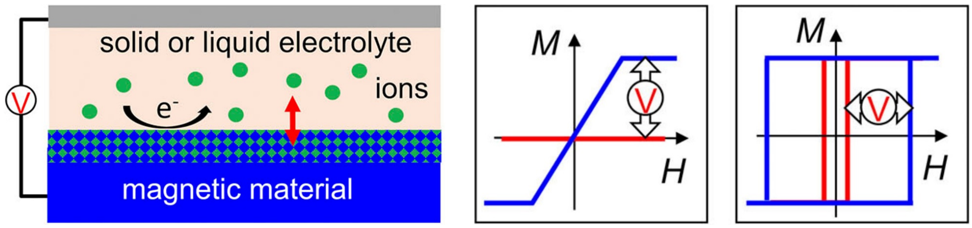

Figure 6.11: Vue schématique d'une structure magnéto-ionique montrant la migration des ions induite par la tension dans l'électrolyte (à gauche) entraînant des modifications de l'aimantation de saturation (au milieu) et de la coercivité (à droite) du matériau magnétique. Adapté de [53].

le développement de dispositifs spintroniques améliorés à haute efficacité énergétique. La figure 6.11 montre un dispositif magnéto-ionique illustrant la migration des ions sous une tension et les changements de magnétisation de saturation et de coercivité qui peuvent être induits par la magnéto-ionique [53].

Malgré le potentiel de la magnéto-ionique pour développer des dispositifs spintroniques à haut rendement énergétique, plusieurs défis doivent être relevés pour faire avancer la recherche dans ce domaine émergent. Parmi les principaux défis, on peut citer le manque de compréhension de l'impact de la chimie interfaciale sur la réversibilité du processus et les mécanismes physiques sous-jacents, ce qui entrave la conception et l'optimisation des matériaux pour des applications spécifiques. En outre, la difficulté de concevoir et d'accorder des matériaux avec les propriétés souhaitées pour des applications spécifiques, telles que les films magnétiques minces amorphes et cristallins, où le recuit thermique est utilisé pour améliorer la cristallinité et les propriétés magnétiques des films, représente un défi majeur. Cela nécessite une compréhension approfondie du rôle des interfaces magnétiques et de la mobilité des ions dans les systèmes amorphes et cristallins. Enfin, la magnéto-ionique implique des interactions complexes entre les ions et les matériaux, et la stabilité des états magnétiques non volatiles dans le temps doit être prise en compte pour le développement d'applications de dispositifs spintroniques.

Cette thèse porte sur la modulation magnéto-ionique des propriétés magnétiques dans les hétérostructures magnétiques pour le développement et la compréhension des états magnétiques non volatiles. La magnéto-ionique a été démontrée dans des hétérostructures de métal lourd/ferromagnétique/oxyde obtenues par pulvérisation magnétron. Dans le but de développer des systèmes avec des PMA importants et stables, CoFeB a été choisi comme ferromagnétique et HfO_2 comme oxyde conducteur d'ions où il a été démontré que les espèces d'oxygène migrent sous l'application de tensions. Afin d'appliquer des tensions de grille, on a utilisé un gating ionique-liquide, qui a permis d'appliquer des champs électriques élevés sur de grandes surfaces, ce qui a permis de caractériser facilement les changements de propriétés magnétiques induits par la tension de grille avant de les transférer à des dispositifs à l'état solide, ce qui en fait une approche distinctive.

La magnéto-ionique dans les films minces CoFeB/HfO_2 avec différentes couches tampons de métaux lourds et stœchiométrie de CoFeB, où CoFeB et HfO_2 sont amorphes à l'état brut, a été étudiée afin de relever les défis susmentionnés pour développer des dispositifs magnéto-ioniques efficaces. Les effets magnéto-ioniques ont d'abord été étudiés dans Ta/CoFeB/HfO_2, où les effets VCMA conventionnels basés sur la charge dans l'archétype Ta/CoFeB/MgO ont rapporté des changements significatifs dans les propriétés magnétiques. Les résultats interprétés ont ensuite été utilisés pour faire progresser la magnéto-ionique dans W/CoFeB/HfO_2, puis dans Pt/CoFeB/HfO_2. Les principales réalisations de cette thèse sont énumérées ci-dessous :

Résultats

Le **chapitre 4** traite de la magnéto-ionique dans Ta/CoFeB/HfO_2, où une oxydation induite par la tension de grille de l'interface CoFeB/HfO_2 a montré la coexistence de deux régimes magnéto-ioniques : I et II. Le régime I correspond à la région dans laquelle un système sous-oxydé présentant un IPA transite vers un PMA optimalement oxydé. Le régime II correspond à la région dans laquelle un PMA oxydé de façon optimale passe à un état suroxydé présentant un IPA. Le régime I s'avère être plus rapide que le régime II, mais la réversibilité magnéto-ionique n'est observée que dans ce dernier sous les mêmes tensions de grille. De plus, le paramètre d'amortissement effectif (α_{eff}) montre également une dépendance marquée avec les régimes. Le paramètre d'amortissement effectif (α_{eff}) montre également une dépendance marquée avec les régimes. α_{eff} passe de 0,029 dans l'état brut à 0,012 qui coïncide avec l'apparition de la PMA, et augmente légèrement à 0,014 dans le régime II. L'existence des régimes I et II est proposée comme étant le résultat d'une différence dans la force de liaison des espèces d'oxygène migrées, qui peut être corrélée avec différents sites de liaison sur la surface et à l'intérieur de la couche de CoFeB, respectivement. Les résultats présentés dans cette étude montrent la complexité des mécanismes magnéto-ioniques où le même échantillon montre la coexistence de régimes réversibles et irréversibles. Cela permet de choisir une transition IPA vers PMA, soit dans le régime I ou II, qui correspond le mieux aux exigences des applications pratiques et de concevoir des stratégies pour favoriser le fonctionnement dans l'un des deux régimes magnéto-ioniques.

Le **chapitre 5** traite de l'impact du recuit et du gating magnéto-ionique dans W/CoFeB/HfO_2 montre un compromis entre la réversibilité magnéto-ionique et les propriétés magnétiques. Les échantillons bruts présentant un état IPA sous-oxydé n'ont pas induit d'état PMA avec l'oxydation induite par la tension de grille de l'interface CoFeB/HfO_2, alors que les échantillons bruts recuits à 350° et 390° ont présenté un état PMA, indiquant l'importance de l'hybridation 5d-3d de l'interface W/CoFeB. Une oxydation induite par la tension de grille des systèmes recuits a induit une transition de PMA à IPA. Bien que la PMA soit induite dans les systèmes bruts après recuit, une forte DMI de est seulement observée dans les échantillons recuits à 390° pendant 1 heure, qui diminue de 0,60 pJ/m dans l'état initial à 0,06 pJ/m avec une oxydation induite par la tension de grille. Les propriétés magnétiques, y compris la vitesse de la paroi du domaine, s'améliorent considérablement avec l'augmentation de la température et du temps de recuit, tandis que la réversibilité magnéto-ionique est de plus en plus compromise. Les changements de PMA et de DMI induits par les tensions de grille dans les échantillons recuits à

390°C sont permanents, alors qu'une réversibilité partielle n'est observée que pour les échantillons recuits à 350°C pendant de courtes périodes. Cette dépendance de la réversibilité vis-à-vis du recuit post-génération a été associée à l'influence de la cristallisation sur la mobilité des ions. La magnéto-ionique, dans ce cas, peut fournir un moyen post-croissance simple pour ajuster les propriétés magnétiques de manière locale et non-volatile, ce qui pourrait être utilisé, par exemple, pour choisir entre un système réversible ou pour faciliter la nucléation des skyrmions ou pour moduler l'efficacité du couple spin-orbite dans les dispositifs spintroniques basés sur β-W/CoFeB.

Le **chapitre 6** traite de la magnéto-ionique dans Pt/CoFeB/HfO_2, où une oxydation de l'interface CoFeB/HfO_2 induite par une tension de grille a montré la coexistence de deux régimes magnéto-ioniques similaires à ceux de Ta/CoFeB/HfO_2, mais contrairement au système Ta, les deux régimes dans Pt/CoFeB/HfO_2 sont réversibles. Cependant, on constate que la stabilité des états magnéto-ioniques du régime I est nettement meilleure que celle des états magnéto-ioniques du régime II, qui évolue avec le temps. De plus, la stabilité montre également une dépendance marquée de l'épaisseur de la couche de HfO_2, où un HfO_2 plus fin démontre une meilleure stabilité en régime II. Cette disparité dans la stabilité des états magnétiques dans les régimes I et II et les différentes épaisseurs de HfO_2 a été liée à la force de liaison des espèces d'oxygène à l'interface CoFeB/HfO_2 et à la disponibilité des sites "déficients" en oxygène générés par les atomes de Hf à l'interface, respectivement. Les systèmes Pt/CoFeB sont connus pour leur fort couplage spin-orbite, leur DMI, leur anisotropie et la stabilisation des skyrmions à température ambiante. L'amélioration de la stabilité de l'état magnétique est donc d'une grande importance pour le développement de dispositifs spintroniques à base de magnéto-ionique.

Les résultats élucidés dans le cadre de cette thèse mettent en évidence les multiples facettes de la magnéto-ionique dans un large éventail de systèmes, en soulignant l'importance de la chimie interfaciale, de la nature amorphe et cristalline et de la composition de l'empilement magnétique, ainsi que de la stabilité des états magnétiques non volatils. Ces réalisations comprennent une meilleure compréhension des complexités de la magnéto-ionique, ainsi que l'identification de stratégies potentielles pour améliorer l'efficacité des dispositifs magnéto-ioniques.

Perspectives

Les résultats présentés dans cette thèse ouvrent plusieurs possibilités pour l'exploration des propriétés magnétiques et pour le développement de futurs dispositifs magnéto-ioniques, notamment dans l'informatique neuromorphique. Il est bien connu que le domaine de l'intelligence artificielle se développe rapidement, car il permet aux machines d'apprendre et d'exécuter des tâches semblables à celles des humains. L'intérêt croissant pour l'intelligence artificielle implique également une utilisation énorme du traitement informatique et de la mémoire. Les ordinateurs modernes utilisent une architecture dite de von Neumann, dans laquelle les unités de stockage et de traitement des données sont physiquement séparées. Par conséquent, les grandes quantités de données impliquées dans l'intelligence artificielle doivent être transférées dans les deux sens entre les unités de stockage et de traitement des données afin d'effectuer une tâche, ce qui coûte une quantité importante d'énergie. Dans les ordinateurs modernes, la majeure partie de l'énergie consommée pour effectuer une telle tâche provient uniquement du transfert de données entre les deux unités de traitement. Une solution à ce problème consiste à intégrer les deux unités ensemble, comme dans un cerveau humain, dans lequel les neurones sont les unités de traitement qui sont interconnectées par des synapses (unités de stockage de la mémoire) avec des poids synaptiques [173]. L'informatique neuromorphique, également appelée informatique adaptative ou cognitive, est une telle approche inspirée du cerveau au niveau matériel. Il a été démontré que les multiples états de résistance non volatils dans une mémoire vive résistive (memristor) peuvent être utilisés pour mettre à jour les poids synaptiques dans un circuit neuromorphique : [174, 175]. Ce concept pourrait être utilisé pour développer des systèmes magnétiques analogues économes en énergie, dans lesquels les systèmes magnéto-ioniques présentés précédemment peuvent aider à générer de multiples états magnétiques intermédiaires non volatils pour les poids synaptiques. En outre, l'évolution temporelle des états magnétiques observés dans Pt/CoFeB/HfO_2 peut être utilisée pour imiter les fonctions d'apprentissage ou d'oubli neuromorphiques sans aucune tension de grille appliquée, qui peuvent également être réinitialisées une fois le calcul terminé. En outre, les systèmes pourraient également être étudiés pour générer des skyrmions, auquel cas un dispositif neuromorphique à la fois magnéto-ionique et basé sur les skyrmions peut être réalisé dans un seul dispositif.

Dans le but de développer des dispositifs SOT efficaces en énergie, le W/CoFeB/HfO_2 pourrait être d'une grande importance en raison de son grand angle de hall de spin. Comme mentionné précédemment dans 2.5.6, l'inversion magnéto-ionique du SOT a été démontrée dans Pt/Co/GdO_x. Une ingénierie soignée de l'empilement du courant β-W/CoFeB/HfO_2 pourrait être utilisée pour augmenter l'ampleur de l'accumulation de spin en plus de l'inversion SOT. De plus, le réglage du champ électrique de la DMI dans le W/CoFeB/HfO_2 pourrait aussi potentiellement accueillir et modifier des structures magnétiques chirales telles que des parois de domaine de Néel et des skyrmions pour le développement de la mémoire en piste. De plus, la modulation magnéto-ionique des propriétés magnétiques peut être explorée dans le α-W et le $(\alpha+\beta)$-W afin de répondre au mieux aux exigences. Le système Pt/CoFeB/HfO_2 présenté dans le dernier chapitre, en plus de deux régimes, montre également une réversibilité dans les deux régimes, ce qui pourrait être utilisé pour développer un dispositif rapide à paroi de domaine ou à piste de skyrmion qui peut également être une porte logique en arrangeant les portes de manière périodique, grâce au grand couplage spin-orbite et au DMI de Pt/CoFeB. En outre, la réversibilité de plusieurs propriétés magnétiques telles que le DMI et le paramètre d'amortissement, ainsi que la dépendance de la réversibilité à la stœchiométrie de CoFeB, peuvent également être explorées. De plus, la méthode proposée pour améliorer la stabilité magnéto-ionique pourrait être mise en œuvre dans le développement de dispositifs pouvant accueillir des skyrmions stables.

List of publications

Peer-reviewed journal articles

- **Rohit Pachat**, Djoudi Ourdani, Maria-Andromachi Syskaki, Alessio Lamperti, Subhajit Roy, Song Chen, Adriano Di Pietro, Ludovic Largeau, Roméo Juge, Maryam Massouras, Cristina Balan, Johannes Wilhelmus van der Jagt, Guillaume Agnus, Yves Roussigné, Mihai Gabor, Salim Mourad Chérif, Gianfranco Durin, Shimpei Ono, Jürgen Langer, Damien Querlioz, Dafiné Ravelosona, Mohamed Belmeguenai, and Liza Herrera Diez, "Magneto-Ionics in Annealed W/CoFeB/HfO_2 Thin Films", Advanced Materials Interfaces, 9(36):2200690, 2022.

- **R. Pachat**, D. Ourdani, J.W. van der Jagt, M.-A. Syskaki, A. Di Pietro, Y. Roussigné, S. Ono, M.S. Gabor, M. Chérif, G. Durin, J. Langer, M. Belmeguenai, D. Ravelosona, and L. Herrera Diez, "Multiple Magnetoionic Regimes in Ta/$Co_{20}Fe_{60}B_{20}$/HfO_2", Physical Review Applied, 15(6):064055, June 2021.

- Adriano Di Pietro, **Rohit Pachat**, Liza Herrera Diez, Johannes W. van der Jagt, Dafiné Ravelosona, and Gianfranco Durin, "Ab-initio study of magneto-ionic mechanisms in ferromagnet/oxide multilayers", submitted, arXiv:2204.11699.

- T. Bhatnagar-Schöffmann, A. Kovàcs, **R. Pachat**, D. Ourdani, A. Lamperti, M.-A. Syskaki, T. da Câmara Santa Clara Gomes, Y. Roussigné, S. Ono, J. Langer, M. Cherif, R. E. Dunin-Borkowski, P. Schöffmann, D. Ravelosona, M. Belmeguenai, A. Solignac, and L. Herrera Diez, "Controlling interface anisotropy in CoFeB/MgO/HfO_2 using dusting layers and magneto-ionic gating", Appl. Phys. Lett. 122, 042402, 2023.

Conferences

- **R. Pachat**, D. Ourdani, M.-A. Syskaki, T. Bhatnagar-Schöffmann, S. Roy, M. Massouras, A. Lamperti, Y. Roussigné, S. Ono, J. Langer, D. Ravelosona, M. Belmeguenai, and L. Herrera Diez, "Stability of under/over oxidized magneto-ionic states in Pt/Co_{60} $Fe_{20}B_{20}$/HfO_2", Magnetism and Magnetic Materials (MMM) 2022, oral presentation.

- **R. Pachat**, D. Ourdani, M.-A. Syskaki, A. Lamperti, S. Roy, A. di Pietro, L. Largeau, R. Juge, C. Balan, J. W. van der Jagt, Y. Roussigné, M. Gabor, S. M. Chérif, G. Durin, S. Ono, J. Langer, M. Belmeguenai, D. Ravelosona, and L. Herrera Diez, "Magneto-ionics in CoFeB/HfO_2 on Ta and W buffer layers", MagnEFi Conference 2022, poster presentation.

- **R. Pachat**, D. Ourdani, M.-A. Syskaki, A. Lamperti, S. Roy, A. di Pietro, R. Juge, J. W. van der Jagt, G. Agnus, G. Durin, Y. Roussigné, S. Ono, J. Langer, D. Ravelosona, M. Belmeguenai, L. Herrera Diez, "Magneto-ionic Reversibility in Annealed W/CoFeB/HfO_2", Joint European Magnetic Symposia (JEMS) 2022, oral presentation.

- **Rohit Pachat**, Djoudi Ourdani, Maria-Andromachi Syskaki, Adriano Di Pietro, Ludovic Largeau, Roméo Juge, Cristina Balan, Johannes Wilhelmus van der Jagt, Yves Roussigné, Mihai Gabor, Salim Mourad Chérif, Gianfranco Durin, Shimpei Ono, Jürgen Langer, Dafiné Ravelosona, Mohamed Belmeguenai, and Liza Herrera Diez, "Effect of Annealing on Magnetoionics in W/$Co_{20}Fe_{60}B_{20}$/HfO_2", Joint MMM-INTERMAG 2022, oral presentation.

- **R. Pachat**, D. Ourdani, J. W. van der Jagt, M.-A. Syskaki, A. di Pietro, M. Belmeguenai, Y. Roussigné, G. Durin, S. Ono, J. Langer, D. Ravelosona, and L. Herrera Diez, "Reversible and Irreversible Magneto-ionic Regimes in Ta/CoFeB/HfO_2", INTERMAG 2021, oral presentation.

Bibliography

[1] M. N. Baibich, J. M. Broto, A. Fert, F. Nguyen Van Dau, F. Petroff, P. Etienne, G. Creuzet, A. Friederich, and J. Chazelas. Giant Magnetoresistance of (001)Fe/(001)Cr Magnetic Superlattices. *Physical Review Letters*, 61(21):2472–2475, November 1988. Publisher: American Physical Society.

[2] G. Binasch, P. Grünberg, F. Saurenbach, and W. Zinn. Enhanced magnetoresistance in layered magnetic structures with antiferromagnetic interlayer exchange. *Physical Review B*, 39(7):4828–4830, March 1989. Publisher: American Physical Society.

[3] M. Julliere. Tunneling between ferromagnetic films. *Physics Letters A*, 54(3):225–226, September 1975.

[4] Claude Chappert, Albert Fert, and Frédéric Nguyen Van Dau. The emergence of spin electronics in data storage. *Nature Materials*, 6(11):813–823, November 2007. Number: 11 Publisher: Nature Publishing Group.

[5] Seagate Reaches 1 Terabit Per Square Inch Milestone In Hard Drive Storage With New Technology Demonstration | News Archive | Seagate US.

[6] B. Dieny, I. L. Prejbeanu, K. Garello, P. Gambardella, P. Freitas, R. Lehndorff, W. Raberg, U. Ebels, S. O. Demokritov, J. Akerman, A. Deac, P. Pirro, C. Adelmann, A. Anane, A. V. Chumak, A. Hirohata, S. Mangin, Sergio O. Valenzuela, M. Cengiz Onbaşlı, M. d'Aquino, G. Prenat, G. Finocchio, L. Lopez-Diaz, R. Chantrell, O. Chubykalo-Fesenko, and P. Bortolotti. Opportunities and challenges for spintronics in the microelectronics industry. *Nature Electronics*, 3(8):446–459, August 2020. Number: 8 Publisher: Nature Publishing Group.

[7] Andrew D. Kent and Daniel C. Worledge. A new spin on magnetic memories. *Nature Nanotechnology*, 10(3):187–191, March 2015. Number: 3 Publisher: Nature Publishing Group.

[8] S. S. P. Parkin, M. Hayashi, and L. Thomas. Magnetic Domain-Wall Racetrack Memory. *Science*, 320(5873):190–194, April 2008.

[9] Klaus D. Sattler, editor. *Handbook of Nanophysics: Principles and Methods*. CRC Press, Boca Raton, September 2010.

[10] J. C. Slonczewski. Current-driven excitation of magnetic multilayers. *Journal of Magnetism and Magnetic Materials*, 159(1):L1–L7, June 1996.

[11] L. Berger. Emission of spin waves by a magnetic multilayer traversed by a current. *Physical Review B*, 54(13):9353–9358, October 1996. Publisher: American Physical Society.

[12] Ioan Mihai Miron, Kevin Garello, Gilles Gaudin, Pierre-Jean Zermatten, Marius V. Costache, Stéphane Auffret, Sébastien Bandiera, Bernard Rodmacq, Alain Schuhl, and Pietro Gambardella. Perpendicular switching of a single ferromagnetic layer induced by in-plane current injection. *Nature*, 476(7359):189–193, August 2011. Number: 7359 Publisher: Nature Publishing Group.

[13] Y. K. Kato, R. C. Myers, A. C. Gossard, and D. D. Awschalom. Observation of the Spin Hall Effect in Semiconductors. *Science*, 306(5703):1910–1913, December 2004. Publisher: American Association for the Advancement of Science.

[14] Jairo Sinova, Sergio O. Valenzuela, J. Wunderlich, C.H. Back, and T. Jungwirth. Spin Hall effects. *Reviews of Modern Physics*, 87(4):1213–1260, October 2015. Publisher: American Physical Society.

[15] J. Wunderlich, B. Kaestner, J. Sinova, and T. Jungwirth. Experimental Observation of the Spin-Hall Effect in a Two-Dimensional Spin-Orbit Coupled Semiconductor System. *Physical Review Letters*, 94(4):047204, February 2005. Publisher: American Physical Society.

[16] H. Sanada, Y. Kunihashi, H. Gotoh, K. Onomitsu, M. Kohda, J. Nitta, P. V. Santos, and T. Sogawa. Manipulation of mobile spin coherence using magnetic-field-free electron spin resonance. *Nature Physics*, 9(5):280–283, May 2013. Number: 5 Publisher: Nature Publishing Group.

[17] A. Manchon, H. C. Koo, J. Nitta, S. M. Frolov, and R. A. Duine. New perspectives for Rashba spin–orbit coupling. *Nature Materials*, 14(9):871–882, September 2015. Number: 9 Publisher: Nature Publishing Group.

[18] Arne Brataas, Andrew D. Kent, and Hideo Ohno. Current-induced torques in magnetic materials. *Nature Materials*, 11(5):372–381, May 2012. Number: 5 Publisher: Nature Publishing Group.

[19] Yue Zhang, Xueying Zhang, Jingtong Hu, Jiang Nan, Zhenyi Zheng, Zhizhong Zhang, Youguang Zhang, Nicolas Vernier, Dafine Ravelosona, and Weisheng Zhao. Ring-shaped Racetrack memory based on spin orbit torque driven chiral domain wall motions. *Scientific Reports*, 6(1):35062, October 2016. Number: 1 Publisher: Nature Publishing Group.

[20] Prashanth Barla, Vinod Kumar Joshi, and Somashekara Bhat. Spintronic devices: a promising alternative to CMOS devices. *Journal of Computational Electronics*, 20(2):805–837, April 2021.

[21] T. Maruyama, Y. Shiota, T. Nozaki, K. Ohta, N. Toda, M. Mizuguchi, A. A. Tulapurkar, T. Shinjo, M. Shiraishi, S. Mizukami, Y. Ando, and Y. Suzuki. Large voltage-induced magnetic anisotropy change in a few atomic layers of iron. *Nature Nanotechnology*, 4(3):158–161, March 2009. Bandiera_abtest: a Cg_type: Nature Research Journals Number: 3 Primary_atype: Research Publisher: Nature Publishing Group.

[22] S. Methfessel. Potential applications of magnetic rare earth compunds. *IEEE Transactions on Magnetics*, 1(3):144–155, September 1965. Conference Name: IEEE Transactions on Magnetics.

[23] G. H. O. Daalderop, P. J. Kelly, and M. F. H. Schuurmans. First-principles calculation of the magnetocrystalline anisotropy energy of iron, cobalt, and nickel. *Physical Review B*, 41(17):11919–11937, June 1990. Publisher: American Physical Society.

[24] G. H. O. Daalderop, P. J. Kelly, and M. F. H. Schuurmans. Magnetocrystalline anisotropy and orbital moments in transition-metal compounds. *Physical Review B*, 44(21):12054–12057, December 1991.

[25] H. Ohno, D. Chiba, F. Matsukura, T. Omiya, E. Abe, T. Dietl, Y. Ohno, and K. Ohtani. Electric-field control of ferromagnetism. *Nature*, 408(6815):944–946, December 2000. Number: 6815 Publisher: Nature Publishing Group.

[26] Cheng Song, Bin Cui, Fan Li, Xiangjun Zhou, and Feng Pan. Recent progress in voltage control of magnetism: Materials, mechanisms, and performance. *Progress in Materials Science*, 87:33–82, June 2017.

[27] M. Weisheit, S. Fahler, A. Marty, Y. Souche, C. Poinsignon, and D. Givord. Electric Field-Induced Modification of Magnetism in Thin-Film Ferromagnets. *Science*, 315(5810):349–351, January 2007.

[28] A. Bernand-Mantel, L. Herrera-Diez, L. Ranno, S. Pizzini, J. Vogel, D. Givord, S. Auffret, O. Boulle, I. M. Miron, and G. Gaudin. Electric-field control of domain wall nucleation and pinning in a metallic ferromagnet. *Applied Physics Letters*, 102(12):122406, March 2013.

[29] Y. T. Liu, S. Ono, G. Agnus, J.-P. Adam, S. Jaiswal, J. Langer, B. Ocker, D. Ravelosona, and L. Herrera Diez. Electric field controlled domain wall dynamics and magnetic easy axis switching in liquid gated CoFeB/MgO films. *Journal of Applied Physics*, 122(13):133907, October 2017.

[30] Titiksha Srivastava, Marine Schott, Roméo Juge, Viola Křižáková, Mohamed Belmeguenai, Yves Roussigné, Anne Bernand-Mantel, Laurent Ranno, Stefania Pizzini, Salim-Mourad Chérif, Andrey Stashkevich, Stéphane Auffret, Olivier Boulle, Gilles Gaudin, Mairbek Chshiev, Claire Baraduc, and Hélène

Béa. Large-Voltage Tuning of Dzyaloshinskii–Moriya Interactions: A Route toward Dynamic Control of Skyrmion Chirality. *Nano Letters*, 18(8):4871–4877, August 2018.

[31] Tomohiro Koyama, Yoshinobu Nakatani, Jun'ichi Ieda, and Daichi Chiba. Electric field control of magnetic domain wall motion via modulation of the Dzyaloshinskii-Moriya interaction. *Science Advances*, 4(12):eaav0265, December 2018.

[32] Wang Kang, Yangqi Huang, Chentian Zheng, Weifeng Lv, Na Lei, Youguang Zhang, Xichao Zhang, Yan Zhou, and Weisheng Zhao. Voltage Controlled Magnetic Skyrmion Motion for Racetrack Memory. *Scientific Reports*, 6(1):23164, March 2016. Number: 1 Publisher: Nature Publishing Group.

[33] Wei-Gang Wang, Mingen Li, Stephen Hageman, and C. L. Chien. Electric-field-assisted switching in magnetic tunnel junctions. *Nature Materials*, 11(1):64–68, January 2012.

[34] Eva Grimaldi, Viola Krizakova, Giacomo Sala, Farrukh Yasin, Sébastien Couet, Gouri Sankar Kar, Kevin Garello, and Pietro Gambardella. Single-shot dynamics of spin–orbit torque and spin transfer torque switching in three-terminal magnetic tunnel junctions. *Nature Nanotechnology*, 15(2):111–117, February 2020. Number: 2 Publisher: Nature Publishing Group.

[35] L. Herrera Diez, Y.T. Liu, D.A. Gilbert, M. Belmeguenai, J. Vogel, S. Pizzini, E. Martinez, A. Lamperti, J.B. Mohammedi, A. Laborieux, Y. Roussigné, A.J. Grutter, E. Arenholtz, P. Quarterman, B. Maranville, S. Ono, M. Salah El Hadri, R. Tolley, E.E. Fullerton, L. Sanchez-Tejerina, A. Stashkevich, S.M. Chérif, A.D. Kent, D. Querlioz, J. Langer, B. Ocker, and D. Ravelosona. Nonvolatile Ionic Modification of the Dzyaloshinskii-Moriya Interaction. *Physical Review Applied*, 12(3):034005, September 2019.

[36] Uwe Bauer, Satoru Emori, and Geoffrey S. D. Beach. Voltage-controlled domain wall traps in ferromagnetic nanowires. *Nature Nanotechnology*, 8(6):411–416, June 2013.

[37] Shufeng Zhang. Spin-Dependent Surface Screening in Ferromagnets and Magnetic Tunnel Junctions. *Physical Review Letters*, 83(3):640–643, July 1999.

[38] Uwe Bauer, Lide Yao, Aik Jun Tan, Parnika Agrawal, Satoru Emori, Harry L. Tuller, Sebastiaan van Dijken, and Geoffrey S. D. Beach. Magneto-ionic control of interfacial magnetism. *Nature Materials*, 14(2):174–181, February 2015.

[39] Louis Néel. Anisotropie magnétique superficielle et surstructures d'orientation. *Journal de Physique et le Radium*, 15(4):225–239, April 1954. Publisher: Revue Générale de l'Electricité.

[40] Alex Hubert and Rudolf Schäfer. *Magnetic Domains*. Springer, Berlin, Heidelberg, 1998.

[41] B. Dieny and M. Chshiev. Perpendicular magnetic anisotropy at transition metal/oxide interfaces and applications. *Reviews of Modern Physics*, 89(2):025008, June 2017. Publisher: American Physical Society.

[42] Hongxin Yang, Jinghua Liang, and Qirui Cui. First-principles calculations for Dzyaloshinskii–Moriya interaction. *Nature Reviews Physics*, pages 1–19, November 2022. Publisher: Nature Publishing Group.

[43] Tôru Moriya. Anisotropic Superexchange Interaction and Weak Ferromagnetism. *Physical Review*, 120(1):91–98, October 1960.

[44] Charles-Elie Fillion, Johanna Fischer, Raj Kumar, Aymen Fassatoui, Stefania Pizzini, Laurent Ranno, Djoudi Ourdani, Mohamed Belmeguenai, Yves Roussigné, Salim-Mourad Chérif, Stéphane Auffret, Isabelle Joumard, Olivier Boulle, Gilles Gaudin, Liliana Buda-Prejbeanu, Claire Baraduc, and Hélène Béa. Gate-controlled skyrmion and domain wall chirality. *Nature Communications*, 13(1):5257, September 2022. Number: 1 Publisher: Nature Publishing Group.

[45] I. Dzyaloshinsky. A thermodynamic theory of "weak" ferromagnetism of antiferromagnetics. *Journal of Physics and Chemistry of Solids*, 4(4):241–255, January 1958.

[46] S. Mühlbauer, B. Binz, F. Jonietz, C. Pfleiderer, A. Rosch, A. Neubauer, R. Georgii, and P. Böni. Skyrmion Lattice in a Chiral Magnet. *Science*, 323(5916):915–919, February 2009. Publisher: American Association for the Advancement of Science.

[47] Nicolas Josten, Thomas Feggeler, Ralf Meckenstock, Detlef Spoddig, Marina Spasova, Ke Chai, Iliya Radulov, Zi-An Li, Oliver Gutfleisch, Michael Farle, and Benjamin Zingsem. Dynamic unidirectional anisotropy in cubic FeGe with antisymmetric spin-spin-coupling. *Scientific Reports*, 10(1):2861, February 2020. Number: 1 Publisher: Nature Publishing Group.

[48] Shouzhong Peng, Daoqian Zhu, Jiaqi Zhou, Boyu Zhang, Anni Cao, Mengxing Wang, Wenlong Cai, Kaihua Cao, and Weisheng Zhao. Modulation of Heavy Metal/Ferromagnetic Metal Interface for High-Performance Spintronic Devices. *Advanced Electronic Materials*, 5(8):1900134, 2019. _eprint: https://onlinelibrary.wiley.com/doi/pdf/10.1002/aelm.201900134.

[49] Dayane de Souza Chaves, Fernando Ajejas, Viola Křižáková, Jan Vogel, and Stefania Pizzini. Oxidation dependence of the Dzyaloshinskii-Moriya interaction in Pt / Co / M O x trilayers (M = Al or Gd). *Physical Review B*, 99(14):144404, April 2019.

[50] Ki-Young Lee, Sujin Jo, Aik Jun Tan, Mantao Huang, Dongwon Choi, Jung Hoon Park, Ho-Il Ji, Ji-Won Son, Joonyeon Chang, Geoffrey S. D. Beach, and Seonghoon Woo. Fast Magneto-Ionic Switching of Interface Anisotropy Using Yttria-Stabilized Zirconia Gate Oxide. *Nano Letters*, 20(5):3435–3441, May 2020.

[51] Karin Leistner. Electrochemical approaches to room temperature magnetoelectric materials. *Current Opinion in Electrochemistry*, 25:100636, February 2021.

[52] Jonas Zehner, Rico Huhnstock, Steffen Oswald, Ulrike Wolff, Ivan Soldatov, Arno Ehresmann, Kornelius Nielsch, Dennis Holzinger, and Karin Leistner. Nonvolatile Electric Control of Exchange Bias by a Redox Transformation of the Ferromagnetic Layer. *Advanced Electronic Materials*, 5(6):1900296, 2019. _eprint: https://onlinelibrary.wiley.com/doi/pdf/10.1002/aelm.201900296.

[53] M. Nichterwitz, S. Honnali, M. Kutuzau, S. Guo, J. Zehner, K. Nielsch, and K. Leistner. Advances in magneto-ionic materials and perspectives for their application. *APL Materials*, 9(3):030903, March 2021. Publisher: American Institute of Physics.

[54] P. Kondaiah, Habibuddin Shaik, and G. Mohan Rao. Studies on RF magnetron sputtered HfO2 thin films for microelectronic applications. *Electronic Materials Letters*, 11(4):592–600, July 2015.

[55] Chong Bi, Yaohua Liu, T. Newhouse-Illige, M. Xu, M. Rosales, J. W. Freeland, Oleg Mryasov, Shufeng Zhang, S. G. E. te Velthuis, and W. G. Wang. Reversible Control of Co Magnetism by Voltage-Induced Oxidation. *Physical Review Letters*, 113(26):267202, December 2014.

[56] Johanna Seidemann. *Iontronics - Field effect study of different devices, using techniques of ionic liquid gating*. PhD thesis, Université Grenoble Alpes, 2017.

[57] S. Ono, K. Miwa, S. Seki, and J. Takeya. A comparative study of organic single-crystal transistors gated with various ionic-liquid electrolytes. *Applied Physics Letters*, 94(6):063301, February 2009. Publisher: American Institute of Physics.

[58] Srđan Begić, Fangfang Chen, Erlendur Jónsson, and Maria Forsyth. Overscreening and crowding in electrochemical ionic liquid systems. *Physical Review Materials*, 3(9):095801, September 2019. Publisher: American Physical Society.

[59] Martin Z. Bazant, Brian D. Storey, and Alexei A. Kornyshev. Double Layer in Ionic Liquids: Overscreening versus Crowding. *Physical Review Letters*, 106(4):046102, January 2011. Publisher: American Physical Society.

[60] Michel Armand, Frank Endres, Douglas R. MacFarlane, Hiroyuki Ohno, and Bruno Scrosati. Ionic-liquid materials for the electrochemical challenges of the future. *Nature Materials*, 8(8):621–629, August 2009. Number: 8 Publisher: Nature Publishing Group.

[61] R. Martel, V. Derycke, C. Lavoie, J. Appenzeller, K. K. Chan, J. Tersoff, and Ph. Avouris. Ambipolar Electrical Transport in Semiconducting Single-Wall Carbon Nanotubes. *Physical Review Letters*, 87(25):256805, December 2001. Publisher: American Physical Society.

[62] Patricia C. Marr and Andrew C. Marr. Ionic liquid gel materials: applications in green and sustainable chemistry. *Green Chemistry*, 18(1):105–128, December 2015. Publisher: The Royal Society of Chemistry.

[63] Takuya Fujimoto and Kunio Awaga. Electric-double-layer field-effect transistors with ionic liquids. *Physical Chemistry Chemical Physics*, 15(23):8983–9006, May 2013. Publisher: The Royal Society of Chemistry.

[64] Takahiro Ampo and Takahide Oya. Development of Paper Actuators Based on Carbon-Nanotube-Composite Paper. *Molecules*, 26(5):1463, January 2021. Number: 5 Publisher: Multidisciplinary Digital Publishing Institute.

[65] A. Cimini, O. Palumbo, E. Simonetti, M. De Francesco, G. B. Appetecchi, S. Fantini, R. Lin, A. Falgayrat, and A. Paolone. Decomposition temperatures and vapour pressures of selected ionic liquids for electrochemical applications. *Journal of Thermal Analysis and Calorimetry*, 142(5):1791–1797, December 2020.

[66] Kallidanthiyil Chellappan Lethesh, Ahmed Bahaa, Mariam Abdullah, Musbaudeen O. Bamgbopa, and Rahmat Agung Susantyoko. Temperature-Dependent Electrochemical Stability Window of Bis(trifluoromethanesulfonyl)imide and Bis(fluorosulfonyl)imide Anion Based Ionic Liquids. *Frontiers in Chemistry*, 10, 2022.

[67] Maan Hayyan, Farouq S. Mjalli, Mohd Ali Hashim, Inas M. AlNashef, and Tan Xue Mei. Investigating the electrochemical windows of ionic liquids. *Journal of Industrial and Engineering Chemistry*, 19(1):106–112, January 2013.

[68] S. Ono, S. Seki, R. Hirahara, Y. Tominari, and J. Takeya. High-mobility, low-power, and fast-switching organic field-effect transistors with ionic liquids. *Applied Physics Letters*, 92(10):103313, March 2008. Publisher: American Institute of Physics.

[69] S. Kanai, M. Yamanouchi, S. Ikeda, Y. Nakatani, F. Matsukura, and H. Ohno. Electric field-induced magnetization reversal in a perpendicular-anisotropy CoFeB-MgO magnetic tunnel junction. *Applied Physics Letters*, 101(12):122403, September 2012. Publisher: American Institute of Physics.

[70] Takayuki Nozaki, Anna Kozioł-Rachwał, Masahito Tsujikawa, Yoichi Shiota, Xiandong Xu, Tadakatsu Ohkubo, Takuya Tsukahara, Shinji Miwa, Motohiro Suzuki, Shingo Tamaru, Hitoshi Kubota, Akio Fukushima, Kazuhiro Hono, Masafumi Shirai, Yoshishige Suzuki, and Shinji Yuasa. Highly efficient voltage control of spin and enhanced interfacial perpendicular magnetic anisotropy in iridium-doped Fe/MgO magnetic tunnel junctions. *NPG Asia Materials*, 9(12):e451–e451, December 2017. Number: 12 Publisher: Nature Publishing Group.

[71] Xiangjun Zhou, Yinuo Yan, Miao Jiang, Bin Cui, Feng Pan, and Cheng Song. Role of Oxygen Ion Migration in the Electrical Control of Magnetism in Pt/Co/Ni/HfO2 Films. *The Journal of Physical Chemistry C*, 120(3):1633–1639, January 2016. Publisher: American Chemical Society.

[72] Q. Li, S. S. Yan, J. Xu, S. D. Li, G. X. Zhao, Y. Z. Long, T. T. Shen, K. Zhang, and J. Zhang. Electrical control of exchange bias via oxygen migration across CoO-ZnO nanocomposite barrier. *Applied Physics Letters*, 109(25):252406, December 2016. Publisher: American Institute of Physics.

[73] Dustin A. Gilbert, Justin Olamit, Randy K. Dumas, B. J. Kirby, Alexander J. Grutter, Brian B. Maranville, Elke Arenholz, Julie A. Borchers, and Kai Liu. Controllable positive exchange bias via redox-driven oxygen migration. *Nature Communications*, 7(1):11050, April 2016.

[74] Cristina Balan, Jose Peña Garcia, Aymen Fassatoui, Jan Vogel, Dayane de Souza Chaves, Marlio Bonfim, Jean-Pascal Rueff, Laurent Ranno, and Stefania Pizzini. Tuning the Dynamics of Chiral Domain Walls of Ferrimagnetic Films by Magnetoionic Effects. *Physical Review Applied*, 18(3):034065, September 2022. Publisher: American Physical Society.

[75] Y. N. Yan, X. J. Zhou, F. Li, B. Cui, Y. Y. Wang, G. Y. Wang, F. Pan, and C. Song. Electrical control of Co/Ni magnetism adjacent to gate oxides with low oxygen ion mobility. *Applied Physics Letters*, 107(12):122407, September 2015. Publisher: American Institute of Physics.

[76] Ke Gu, Yicheng Guan, Binoy Krishna Hazra, Hakan Deniz, Andrea Migliorini, Wenjie Zhang, and Stuart S. P. Parkin. Three-dimensional racetrack memory devices designed from freestanding magnetic heterostructures. *Nature Nanotechnology*, 17(10):1065–1071, October 2022. Number: 10 Publisher: Nature Publishing Group.

[77] A. Bogdanov and A. Hubert. Thermodynamically stable magnetic vortex states in magnetic crystals. *Journal of Magnetism and Magnetic Materials*, 138(3):255–269, December 1994.

[78] Wanjun Jiang, Pramey Upadhyaya, Wei Zhang, Guoqiang Yu, M. Benjamin Jungfleisch, Frank Y. Fradin, John E. Pearson, Yaroslav Tserkovnyak, Kang L. Wang, Olle Heinonen, Suzanne G. E. te Velthuis, and Axel Hoffmann. Blowing magnetic skyrmion bubbles. *Science*, 349(6245):283–286, July 2015. Publisher: American Association for the Advancement of Science.

[79] Albert Fert, Nicolas Reyren, and Vincent Cros. Magnetic skyrmions: advances in physics and potential applications. *Nature Reviews Materials*, 2(7):17031, July 2017.

[80] X. Z. Yu, N. Kanazawa, W. Z. Zhang, T. Nagai, T. Hara, K. Kimoto, Y. Matsui, Y. Onose, and Y. Tokura. Skyrmion flow near room temperature in an ultralow current density. *Nature Communications*, 3(1):988, August 2012. Number: 1 Publisher: Nature Publishing Group.

[81] Albert Fert, Vincent Cros, and João Sampaio. Skyrmions on the track. *Nature Nanotechnology*, 8(3):152–156, March 2013.

[82] R. Tomasello, E. Martinez, R. Zivieri, L. Torres, M. Carpentieri, and G. Finocchio. A strategy for the design of skyrmion racetrack memories. *Scientific Reports*, 4(1):6784, October 2014. Number: 1 Publisher: Nature Publishing Group.

[83] Se Kwon Kim, Geoffrey S. D. Beach, Kyung-Jin Lee, Teruo Ono, Theo Rasing, and Hyunsoo Yang. Ferrimagnetic spintronics. *Nature Materials*, 21(1):24–34, January 2022. Number: 1 Publisher: Nature Publishing Group.

[84] Joseph Finley and Luqiao Liu. Spintronics with compensated ferrimagnets. *Applied Physics Letters*, 116(11):110501, March 2020. Publisher: American Institute of Physics.

[85] Lucas Caretta, Maxwell Mann, Felix Büttner, Kohei Ueda, Bastian Pfau, Christian M. Günther, Piet Hessing, Alexandra Churikova, Christopher Klose, Michael Schneider, Dieter Engel, Colin Marcus, David Bono, Kai Bagschik, Stefan Eisebitt, and Geoffrey S. D. Beach. Fast current-driven domain walls

and small skyrmions in a compensated ferrimagnet. *Nature Nanotechnology*, 13(12):1154–1160, December 2018. Number: 12 Publisher: Nature Publishing Group.

[86] Kab-Jin Kim, Se Kwon Kim, Yuushou Hirata, Se-Hyeok Oh, Takayuki Tono, Duck-Ho Kim, Takaya Okuno, Woo Seung Ham, Sanghoon Kim, Gyoungchoon Go, Yaroslav Tserkovnyak, Arata Tsukamoto, Takahiro Moriyama, Kyung-Jin Lee, and Teruo Ono. Fast domain wall motion in the vicinity of the angular momentum compensation temperature of ferrimagnets. *Nature Materials*, 16(12):1187–1192, December 2017. Number: 12 Publisher: Nature Publishing Group.

[87] Kaiming Cai, Zhifeng Zhu, Jong Min Lee, Rahul Mishra, Lizhu Ren, Shawn D. Pollard, Pan He, Gengchiau Liang, Kie Leong Teo, and Hyunsoo Yang. Ultrafast and energy-efficient spin–orbit torque switching in compensated ferrimagnets. *Nature Electronics*, 3(1):37–42, January 2020. Number: 1 Publisher: Nature Publishing Group.

[88] I. Radu, K. Vahaplar, C. Stamm, T. Kachel, N. Pontius, H. A. Dürr, T. A. Ostler, J. Barker, R. F. L. Evans, R. W. Chantrell, A. Tsukamoto, A. Itoh, A. Kirilyuk, Th Rasing, and A. V. Kimel. Transient ferromagnetic-like state mediating ultrafast reversal of antiferromagnetically coupled spins. *Nature*, 472(7342):205–208, April 2011. Number: 7342 Publisher: Nature Publishing Group.

[89] S. S. P. Parkin, N. More, and K. P. Roche. Oscillations in exchange coupling and magnetoresistance in metallic superlattice structures: Co/Ru, Co/Cr, and Fe/Cr. *Physical Review Letters*, 64(19):2304–2307, May 1990. Publisher: American Physical Society.

[90] P. Bruno and C. Chappert. Ruderman-Kittel theory of oscillatory interlayer exchange coupling. *Physical Review B*, 46(1):261–270, July 1992. Publisher: American Physical Society.

[91] Anabela Veloso and Paulo P. Freitas. Spin valve sensors with synthetic free and pinned layers. *Journal of Applied Physics*, 87(9):5744–5746, May 2000. Publisher: American Institute of Physics.

[92] Dmytro Apalkov, Bernard Dieny, and J. M. Slaughter. Magnetoresistive Random Access Memory. *Proceedings of the IEEE*, 104(10):1796–1830, October 2016. Conference Name: Proceedings of the IEEE.

[93] E. Monteblanco, F. Garcia-Sanchez, D. Gusakova, L. D. Buda-Prejbeanu, and U. Ebels. Spin transfer torque nano-oscillators based on synthetic ferrimagnets: Influence of the exchange bias field and interlayer exchange cou-

pling. *Journal of Applied Physics*, 121(1):013903, January 2017. Publisher: American Institute of Physics.

[94] Jiho Yoon, See-Hun Yang, Jae-Chun Jeon, Andrea Migliorini, Ilya Kostanovskiy, Tianping Ma, and Stuart S. P. Parkin. Local and global energy barriers for chiral domain walls in synthetic antiferromagnet–ferromagnet lateral junctions. *Nature Nanotechnology*, 17(11):1183–1191, November 2022. Number: 11 Publisher: Nature Publishing Group.

[95] Yicheng Guan, Xilin Zhou, Fan Li, Tianping Ma, See-Hun Yang, and Stuart S. P. Parkin. Ionitronic manipulation of current-induced domain wall motion in synthetic antiferromagnets. *Nature Communications*, 12(1):5002, August 2021. Number: 1 Publisher: Nature Publishing Group.

[96] See-Hun Yang, Kwang-Su Ryu, and Stuart Parkin. Domain-wall velocities of up to 750 m s1 driven by exchange-coupling torque in synthetic antiferromagnets. *Nature Nanotechnology*, 10(3):221–226, March 2015. Number: 3 Publisher: Nature Publishing Group.

[97] Kevin Garello, Ioan Mihai Miron, Can Onur Avci, Frank Freimuth, Yuriy Mokrousov, Stefan Blügel, Stéphane Auffret, Olivier Boulle, Gilles Gaudin, and Pietro Gambardella. Symmetry and magnitude of spin–orbit torques in ferromagnetic heterostructures. *Nature Nanotechnology*, 8(8):587–593, August 2013. Number: 8 Publisher: Nature Publishing Group.

[98] Ioan Mihai Miron, Gilles Gaudin, Stéphane Auffret, Bernard Rodmacq, Alain Schuhl, Stefania Pizzini, Jan Vogel, and Pietro Gambardella. Current-driven spin torque induced by the Rashba effect in a ferromagnetic metal layer. *Nature Materials*, 9(3):230–234, March 2010. Number: 3 Publisher: Nature Publishing Group.

[99] Rahul Mishra, Farzad Mahfouzi, Dushyant Kumar, Kaiming Cai, Mengji Chen, Xuepeng Qiu, Nicholas Kioussis, and Hyunsoo Yang. Electric-field control of spin accumulation direction for spin-orbit torques. *Nature Communications*, 10(1):248, December 2019.

[100] Aik Jun Tan, Mantao Huang, Can Onur Avci, Felix Büttner, Maxwell Mann, Wen Hu, Claudio Mazzoli, Stuart Wilkins, Harry L. Tuller, and Geoffrey S. D. Beach. Magneto-ionic control of magnetism using a solid-state proton pump. *Nature Materials*, 18(1):35–41, January 2019.

[101] Fengling Zhang, Zhaohui Li, Qingtao Xia, Qinghua Zhang, Chen Ge, Yanxue Chen, Xiangkun Li, Leqing Zhang, Kai Wang, Hongsen Li, Lin Gu, Shishen Yan, Guo-Xing Miao, and Qiang Li. Li-ionic control of magnetism through spin capacitance and conversion. *Matter*, 4(11):3605–3620, November 2021.

[102] Yong Hu, Weiyi Gong, Sichen Wei, Saurabh Khuje, Yulong Huang, Zheng Li, Yuguang C. Li, Fei Yao, Qimin Yan, and Shenqiang Ren. Lithiating magneto-ionics in a rechargeable battery. *Proceedings of the National Academy of Sciences*, 119(25):e2122866119, June 2022. Publisher: Proceedings of the National Academy of Sciences.

[103] Dhanapal Pravarthana, Baomin Wang, Zeeshan Mustafa, Sandeep Agarwal, Ke Pei, Huali Yang, and Run-Wei Li. Reversible Control of Magnetic Anisotropy and Magnetization in Amorphous ${\mathrm{Co}}_{40}{\mathrm{Fe}}_{40}{\mathrm{B}}_{20}$ Thin Films via All-Solid-State Li-ion Redox Capacitor. *Physical Review Applied*, 12(5):054065, November 2019. Publisher: American Physical Society.

[104] Sami Vasala, Anna Jakob, Kerstin Wissel, Aamir Iqbal Waidha, Lambert Alff, and Oliver Clemens. Reversible Tuning of Magnetization in a Ferromagnetic Ruddlesden–Popper-Type Manganite by Electrochemical Fluoride-Ion Intercalation. *Advanced Electronic Materials*, 6(2):1900974, 2020. _eprint: https://onlinelibrary.wiley.com/doi/pdf/10.1002/aelm.201900974.

[105] Julius de Rojas, Alberto Quintana, Aitor Lopeandía, Joaquín Salguero, Beatriz Muñiz, Fatima Ibrahim, Mairbek Chshiev, Aliona Nicolenco, Maciej O. Liedke, Maik Butterling, Andreas Wagner, Veronica Sireus, Llibertat Abad, Christopher J. Jensen, Kai Liu, Josep Nogués, José L. Costa-Krämer, Enric Menéndez, and Jordi Sort. Voltage-driven motion of nitrogen ions: a new paradigm for magneto-ionics. *Nature Communications*, 11(1):5871, November 2020. Bandiera_abtest: a Cc_license_type: cc_by Cg_type: Nature Research Journals Number: 1 Primary_atype: Research Publisher: Nature Publishing Group Subject_term: Magnetic properties and materials;Surfaces, interfaces and thin films Subject_term_id: magnetic-properties-and-materials;surfaces-interfaces-and-thin-films.

[106] Mantao Huang, Muhammad Usama Hasan, Konstantin Klyukin, Delin Zhang, Deyuan Lyu, Pierluigi Gargiani, Manuel Valvidares, Sara Sheffels, Alexandra Churikova, Felix Büttner, Jonas Zehner, Lucas Caretta, Ki-Young Lee, Joonyeon Chang, Jian-Ping Wang, Karin Leistner, Bilge Yildiz, and Geoffrey S. D. Beach. Voltage control of ferrimagnetic order and voltage-assisted writing of ferrimagnetic spin textures. *Nature Nanotechnology*, 16(9):981–988, September 2021. Number: 9 Publisher: Nature Publishing Group.

[107] G. Hildebrandt. The Discovery of the Diffraction of X-rays in Crystals — A Historical Review. *Crystal Research and Technology*, 28(6):747–766, 1993. _eprint: https://onlinelibrary.wiley.com/doi/pdf/10.1002/crat.2170280602.

[108] Naoto Nagaosa, Jairo Sinova, Shigeki Onoda, A. H. MacDonald, and N. P. Ong. Anomalous Hall effect. *Reviews of Modern Physics*, 82(2):1539–1592, May 2010. Publisher: American Physical Society.

[109] Michael Faraday. On the magnetization of light and the illumination of magnetic lines of force. *Philosophical Transactions of the Royal Society of London*, 136:1–20, 1846.

[110] John Kerr. XLIII. On rotation of the plane of polarization by reflection from the pole of a magnet. *The London, Edinburgh, and Dublin Philosophical Magazine and Journal of Science*, 3(19):321–343, May 1877. Publisher: Taylor & Francis _eprint: https://doi.org/10.1080/14786447708639245.

[111] Woldemar Voigt. *Magneto-und elektrooptik*. Number 3. BG Teubner, 1908.

[112] Z. Q Qiu and S. D Bader. Surface magneto-optic Kerr effect (SMOKE). *Journal of Magnetism and Magnetic Materials*, 200(1):664–678, October 1999.

[113] Soong-Geun Je, Duck-Ho Kim, Sang-Cheol Yoo, Byoung-Chul Min, Kyung-Jin Lee, and Sug-Bong Choe. Asymmetric magnetic domain-wall motion by the Dzyaloshinskii-Moriya interaction. *Physical Review B*, 88(21):214401, December 2013. Publisher: American Physical Society.

[114] R. Soucaille, M. Belmeguenai, J. Torrejon, J.-V. Kim, T. Devolder, Y. Roussigné, S.-M. Chérif, A. A. Stashkevich, M. Hayashi, and J.-P. Adam. Probing the Dzyaloshinskii-Moriya interaction in CoFeB ultrathin films using domain wall creep and Brillouin light spectroscopy. *Physical Review B*, 94(10):104431, September 2016. Publisher: American Physical Society.

[115] Simon Foner. Versatile and Sensitive Vibrating-Sample Magnetometer. *Review of Scientific Instruments*, 30(7):548–557, July 1959. Publisher: American Institute of Physics.

[116] Brillouin, Léon. Diffusion de la lumière et des rayons X par un corps transparent homogène - Influence de l'agitation thermique. *Ann. Phys.*, 9(17):88–122, 1922.

[117] Mohamed Belmeguenai, Jean-Paul Adam, Yves Roussigné, Sylvain Eimer, Thibaut Devolder, Joo-Von Kim, Salim Mourad Cherif, Andrey Stashkevich, and André Thiaville. Interfacial Dzyaloshinskii-Moriya interaction in perpendicularly magnetized Pt/Co/AlO x ultrathin films measured by Brillouin light spectroscopy. *Physical Review B*, 91(18):180405, May 2015.

[118] H. Hertz. Ueber einen Einfluss des ultravioletten Lichtes auf die electrische Entladung. *Annalen der Physik*, 267(8):983–1000, 1887. _eprint: https://onlinelibrary.wiley.com/doi/pdf/10.1002/andp.18872670827.

[119] Kai Siegbahn. Electron spectroscopy for atoms, molecules, and condensed matter. *Reviews of Modern Physics*, 54(3):709–728, July 1982. Publisher: American Physical Society.

[120] A Manchon, C Ducruet, L Lombard, S Auffret, B Rodmacq, B Dieny, S Pizzini, J Vogel, and V Uhlí. Analysis of oxygen induced anisotropy crossover in Pt/Co/MOx trilayers. *J. Appl. Phys.*, page 8, 2008.

[121] T. Nagata, M. Haemori, Y. Yamashita, H. Yoshikawa, Y. Iwashita, K. Kobayashi, and T. Chikyow. Oxygen migration at Pt/HfO2/Pt interface under bias operation. *Applied Physics Letters*, 97(8):082902, August 2010. Publisher: American Institute of PhysicsAIP.

[122] Sergey V. Ushakov and Alexandra Navrotsky. Direct measurements of water adsorption enthalpy on hafnia and zirconia. *Applied Physics Letters*, 87(16):164103, October 2005. Publisher: American Institute of Physics.

[123] C. Driemeier, E. P. Gusev, and I. J. R. Baumvol. Room temperature interactions of water vapor with HfO2 films on Si. *Applied Physics Letters*, 88(20):201901, May 2006. Publisher: American Institute of Physics.

[124] Shinji Yuasa, Yoshishige Suzuki, Toshikazu Katayama, and Koji Ando. Characterization of growth and crystallization processes in CoFeBMgOCoFeB magnetic tunnel junction structure by reflective high-energy electron diffraction. *Applied Physics Letters*, 87(24):242503, December 2005. Publisher: American Institute of Physics.

[125] W. G. Wang, J. Jordan-sweet, G. X. Miao, C. Ni, A. K. Rumaiz, L. R. Shah, X. Fan, P. Parsons, R. Stearrett, E. R. Nowak, J. S. Moodera, and J. Q. Xiao. In-situ characterization of rapid crystallization of amorphous CoFeB electrodes in CoFeB/MgO/CoFeB junctions during thermal annealing. *Applied Physics Letters*, 95(24):242501, December 2009. Publisher: American Institute of Physics.

[126] H. Nakayama, K. Ando, K. Harii, T. Yoshino, R. Takahashi, Y. Kajiwara, K. Uchida, Y. Fujikawa, and E. Saitoh. Geometry dependence on inverse spin Hall effect induced by spin pumping in Ni${}_{81}$Fe${}_{19}$/Pt films. *Physical Review B*, 85(14):144408, April 2012. Publisher: American Physical Society.

[127] M Belmeguenai, M S Gabor, F Zighem, N Challab, T Petrisor, R B Mos, and C Tiusan. Ferromagnetic-resonance-induced spin pumping in Co $_{20}$ Fe $_{60}$ B $_{20}$ /Pt systems: damping investigation. *Journal of Physics D: Applied Physics*, 51(4):045002, January 2018.

[128] M. Belmeguenai, D. Apalkov, Y. Roussigné, M. Chérif, A. Stashkevich, G. Feng, and X. Tang. Exchange stiffness and damping constants in diluted CoxFeyB1-x-ythin films. *Journal of Physics D: Applied Physics*, 50(41):415003, September 2017. Publisher: IOP Publishing.

[129] Bijoy K. Kuanr, R. E. Camley, and Z. Celinski. Extrinsic contribution to Gilbert damping in sputtered NiFe films by ferromagnetic resonance. *Journal of Magnetism and Magnetic Materials*, 286:276–281, February 2005.

[130] Amir Capua, See-hun Yang, Timothy Phung, and Stuart S. P. Parkin. Determination of intrinsic damping of perpendicularly magnetized ultrathin films from time-resolved precessional magnetization measurements. *Physical Review B*, 92(22):224402, December 2015. Publisher: American Physical Society.

[131] L. Herrera Diez, M. Voto, A. Casiraghi, M. Belmeguenai, Y. Roussigné, G. Durin, A. Lamperti, R. Mantovan, V. Sluka, V. Jeudy, Y. T. Liu, A. Stashkevich, S. M. Chérif, J. Langer, B. Ocker, L. Lopez-Diaz, and D. Ravelosona. Enhancement of the Dzyaloshinskii-Moriya interaction and domain wall velocity through interface intermixing in Ta/CoFeB/MgO. *Physical Review B*, 99(5):054431, February 2019.

[132] Guang Yang, Jing-Yan Zhang, Shao-Long Jiang, Bo-Wen Dong, Shou-Guo Wang, Jia-Long Liu, Yun-Chi Zhao, Chao Wang, Young Sun, and Guang-Hua Yu. Effect of oxygen migration on magnetic anisotropy and damping constant in perpendicular Ta/CoFeB/Gd/MgO/Ta multilayers. *Applied Surface Science*, 396:705–710, February 2017.

[133] S. Ikeda, K. Miura, H. Yamamoto, K. Mizunuma, H. D. Gan, M. Endo, S. Kanai, J. Hayakawa, F. Matsukura, and H. Ohno. A perpendicular-anisotropy CoFeB–MgO magnetic tunnel junction. *Nature Materials*, 9(9):721–724, September 2010.

[134] I. Benguettat-El Mokhtari, Y. Roussigné, S. M. Chérif, A. Stashkevich, S. Auffret, C. Baraduc, M. Gabor, H. Béa, and M. Belmeguenai. Interface phenomena in ferromagnet/$\mathrm{Ta}{\mathrm{O}}_{x}$-based systems: Damping, perpendicular magnetic anisotropy, and Dzyaloshinskii-Moriya interaction. *Physical Review Materials*, 4(12):124408, December 2020. Publisher: American Physical Society.

[135] Satoshi Iihama, Shigemi Mizukami, Hiroshi Naganuma, Mikihiko Oogane, Yasuo Ando, and Terunobu Miyazaki. Gilbert damping constants of Ta/CoFeB/MgO(Ta) thin films measured by optical detection of precessional magnetization dynamics. *Physical Review B*, 89(17), 2014.

[136] James Lourembam, Abhijit Ghosh, Minggang Zeng, Seng Kai Wong, Qi Jia Yap, and Sze Ter Lim. Thickness-Dependent Perpendicular Magnetic Anisotropy and Gilbert Damping in Hf / Co 20 Fe 60 B 20 / Mg O Heterostructures. *Physical Review Applied*, 10(4):044057, October 2018.

[137] Dustin A. Gilbert, Alexander J. Grutter, Elke Arenholz, Kai Liu, B. J. Kirby, Julie A. Borchers, and Brian B. Maranville. Structural and magnetic depth profiles of magneto-ionic heterostructures beyond the interface limit. *Nature Communications*, 7(1):12264, November 2016.

[138] M. E. Bridge and R. M. Lambert. Oxygen chemisorption, surface oxidation, and the oxidation of carbon monoxide on cobalt (0001). *Surface Science*, 82(2):413–424, April 1979.

[139] C.R. Brundle. Oxygen adsorption and thin oxide formation at iron surfaces: An XPS/UPS study. *Surface Science*, 66(2):581–595, September 1977.

[140] Gary W. Simmons and Daniel J. Dwyer. A LEED-AES study of the initial stages of oxidation of Fe (001). *Surface Science*, 48(2):373–392, March 1975.

[141] L. Herrera Diez, F. García-Sánchez, J.-P. Adam, T. Devolder, S. Eimer, M. S. El Hadri, A. Lamperti, R. Mantovan, B. Ocker, and D. Ravelosona. Controlling magnetic domain wall motion in the creep regime in He+-irradiated CoFeB/MgO films with perpendicular anisotropy. *Applied Physics Letters*, 107(3):032401, July 2015. Publisher: American Institute of Physics.

[142] Gyu Won Kim, Alexander S. Samardak, Yong Jin Kim, In Ho Cha, Alexey V. Ognev, Alexandr V. Sadovnikov, Sergey A. Nikitov, and Young Keun Kim. Role of the Heavy Metal's Crystal Phase in Oscillations of Perpendicular Magnetic Anisotropy and the Interfacial Dzyaloshinskii-Moriya Interaction in W / Co Fe B / MgO Films. *Physical Review Applied*, 9(6):064005, June 2018.

[143] Abhijit Ghosh, Hong Jing Chung, Khoong Hong Khoo, Janaki Shanmugam, Jinjun Qiu, Salauddeen Allauddin, and Sze Ter Lim. Probing the Spin Hall Characteristics of W/CoFeB/MgO Based Heterostructures for Spin-Orbit Torque Based Magnetic Random Access Memory Application. *Advanced Electronic Materials*, n/a(n/a):2100982. _eprint: https://onlinelibrary.wiley.com/doi/pdf/10.1002/aelm.202100982.

[144] Gwang-Guk An, Ja-Bin Lee, Seung-Mo Yang, Jae-Hong Kim, Woo-Seong Chung, and Jin-Pyo Hong. Highly stable perpendicular magnetic anisotropies of CoFeB/MgO frames employing W buffer and capping layers. *Acta Materialia*, 87:259–265, April 2015.

[145] Kai-Uwe Demasius, Timothy Phung, Weifeng Zhang, Brian P. Hughes, See-Hun Yang, Andrew Kellock, Wei Han, Aakash Pushp, and Stuart S. P. Parkin. Enhanced spin–orbit torques by oxygen incorporation in tungsten films. *Nature Communications*, 7(1):10644, February 2016. Bandiera_abtest: a Cc_license_type: cc_by Cg_type: Nature Research Journals Number: 1 Primary_atype: Research Publisher: Nature Publishing Group Subject_term: Spintronics;Surfaces, interfaces and thin films Subject_term_id: spintronics;surfaces-interfaces-and-thin-films.

[146] Girija S. Chaubey, Yuan Yao, Julien P. A. Makongo, Pranati Sahoo, Dinesh Misra, Pierre F. P. Poudeu, and John B. Wiley. Microstructural and thermal investigations of HfO2 nanoparticles. *RSC Advances*, 2(24):9207–9213, September 2012. Publisher: The Royal Society of Chemistry.

[147] Yong Jin Kim, Sung-Gyu Kang, Yeonju Oh, Gyu Won Kim, In Ho Cha, Heung Nam Han, and Young Keun Kim. Microstructural evolution and electrical resistivity of nanocrystalline W thin films grown by sputtering. *Materials Characterization*, 145:473–478, November 2018.

[148] R. Pachat, D. Ourdani, J.W. van der Jagt, M.-A. Syskaki, A. Di Pietro, Y. Roussigné, S. Ono, M.S. Gabor, M. Chérif, G. Durin, J. Langer, M. Belmeguenai, D. Ravelosona, and L. Herrera Diez. Multiple Magnetoionic Regimes in Ta/$Co_{20}Fe_{60}B_{20}$/HfO_2. *Physical Review Applied*, 15(6):064055, June 2021. Publisher: American Physical Society.

[149] Witold Skowroński, Takayuki Nozaki, Duong D. Lam, Yoichi Shiota, Kay Yakushiji, Hitoshi Kubota, Akio Fukushima, Shinji Yuasa, and Yoshishige Suzuki. Underlayer material influence on electric-field controlled perpendicular magnetic anisotropy in CoFeB/MgO magnetic tunnel junctions. *Physical Review B*, 91(18):184410, May 2015.

[150] S. Jaiswal, K. Litzius, I. Lemesh, F. Büttner, S. Finizio, J. Raabe, M. Weigand, K. Lee, J. Langer, B. Ocker, G. Jakob, G. S. D. Beach, and M. Kläui. Investigation of the Dzyaloshinskii-Moriya interaction and room temperature skyrmions in W/CoFeB/MgO thin films and microwires. *Applied Physics Letters*, 111(2):022409, July 2017. Publisher: American Institute of Physics.

[151] Syamlal S k, Shailesh Kalal, Hari Prasanth Perumal, Dileep Kumar, Mukul Gupta, and Jaivardhan Sinha. X-ray photoelectron spectroscopy investigation of Ta/CoFeB/TaOx heterostructures. *Materials Science and Engineering: B*, 272:115367, October 2021.

[152] Beng Jit Tan, Kenneth J. Klabunde, and Peter M. A. Sherwood. X-ray photoelectron spectroscopy studies of solvated metal atom dispersed catalysts.

Monometallic iron and bimetallic iron-cobalt particles on alumina. *Chemistry of Materials*, 2(2):186–191, March 1990.

[153] Beng Jit Tan, Kenneth J. Klabunde, and Peter M. A. Sherwood. XPS studies of solvated metal atom dispersed (SMAD) catalysts. Evidence for layered cobalt-manganese particles on alumina and silica. *Journal of the American Chemical Society*, 113(3):855–861, January 1991.

[154] D.D. Sarma and C.N.R. Rao. XPES studies of oxides of second- and third-row transition metals including rare earths. *Journal of Electron Spectroscopy and Related Phenomena*, 20(1):25–45, January 1980.

[155] C. D. Wagner, D. A. Zatko, and R. H. Raymond. Use of the oxygen KLL Auger lines in identification of surface chemical states by electron spectroscopy for chemical analysis. *Analytical Chemistry*, 52(9):1445–1451, August 1980.

[156] X. D. Xu, K. Mukaiyama, S. Kasai, T. Ohkubo, and K. Hono. Impact of boron diffusion at MgO grain boundaries on magneto-transport properties of MgO/CoFeB/W magnetic tunnel junctions. *Acta Materialia*, 161:360–366, December 2018.

[157] A. V. Khvalkovskiy, V. Cros, D. Apalkov, V. Nikitin, M. Krounbi, K. A. Zvezdin, A. Anane, J. Grollier, and A. Fert. Matching domain-wall configuration and spin-orbit torques for efficient domain-wall motion. *Physical Review B*, 87(2):020402, January 2013. Publisher: American Physical Society.

[158] Thai Ha Pham, J. Vogel, J. Sampaio, M. Vaňatka, J.-C. Rojas-Sánchez, M. Bonfim, D. S. Chaves, F. Choueikani, P. Ohresser, E. Otero, A. Thiaville, and S. Pizzini. Very large domain wall velocities in Pt/Co/GdOx and Pt/Co/Gd trilayers with Dzyaloshinskii-Moriya interaction. *EPL (Europhysics Letters)*, 113(6):67001, March 2016.

[159] V. Krizakova, J. Peña Garcia, J. Vogel, N. Rougemaille, D. de Souza Chaves, S. Pizzini, and A. Thiaville. Study of the velocity plateau of Dzyaloshinskii domain walls. *Physical Review B*, 100(21):214404, December 2019. Publisher: American Physical Society.

[160] Jose Peña Garcia, Aymen Fassatoui, Marlio Bonfim, Jan Vogel, André Thiaville, and Stefania Pizzini. Magnetic domain wall dynamics in the precessional regime: Influence of the Dzyaloshinskii-Moriya interaction. *Physical Review B*, 104(1):014405, July 2021. Publisher: American Physical Society.

[161] C. Burrowes, N. Vernier, J.-P. Adam, L. Herrera Diez, K. Garcia, I. Barisic, G. Agnus, S. Eimer, Joo-Von Kim, T. Devolder, A. Lamperti, R. Mantovan, B. Ockert, E. E Fullerton, and D. Ravelosona. Low depinning fields in

Ta-CoFeB-MgO ultrathin films with perpendicular magnetic anisotropy. *Applied Physics Letters*, 103(18):182401, October 2013. Publisher: American Institute of Physics.

[162] Kyoung-Woong Moon, Seungmo Yang, Tae-Seong Ju, Changsoo Kim, Byoung Sun Chun, Sungkyun Park, and Chanyong Hwang. Universal method for magnetic skyrmion bubble generation by controlling the stripe domain instability. *NPG Asia Materials*, 13(1):20, December 2021.

[163] F. Pan, S. Gao, C. Chen, C. Song, and F. Zeng. Recent progress in resistive random access memories: Materials, switching mechanisms, and performance. *Materials Science and Engineering: R: Reports*, 83:1–59, September 2014.

[164] Xiaojian Zhu, Wenjing Su, Yiwei Liu, Benlin Hu, Liang Pan, Wei Lu, Jiandi Zhang, and Run-Wei Li. Observation of Conductance Quantization in Oxide-Based Resistive Switching Memory. *Advanced Materials*, 24(29):3941–3946, 2012. _eprint: https://onlinelibrary.wiley.com/doi/pdf/10.1002/adma.201201506.

[165] Aymen Fassatoui, Laurent Ranno, Jose PeñaGarcia, Cristina Balan, Jan Vogel, Hélène Béa, and Stefania Pizzini. Kinetics of Ion Migration in the Electric Field-Driven Manipulation of Magnetic Anisotropy of Pt/Co/Oxide Multilayers. *Small*, 17(38):2102427, 2021. _eprint: https://onlinelibrary.wiley.com/doi/pdf/10.1002/smll.202102427.

[166] S. Tacchi, R.E. Troncoso, M. Ahlberg, G. Gubbiotti, M. Madami, J. Åkerman, and P. Landeros. Interfacial Dzyaloshinskii-Moriya Interaction in $\mathrm{Pt}/\mathrm{CoFeB}$ Films: Effect of the Heavy-Metal Thickness. *Physical Review Letters*, 118(14):147201, April 2017. Publisher: American Physical Society.

[167] Jaehun Cho, Nam-Hui Kim, Sukmock Lee, June-Seo Kim, Reinoud Lavrijsen, Aurelie Solignac, Yuxiang Yin, Dong-Soo Han, Niels J. J. van Hoof, Henk J. M. Swagten, Bert Koopmans, and Chun-Yeol You. Thickness dependence of the interfacial Dzyaloshinskii–Moriya interaction in inversion symmetry broken systems. *Nature Communications*, 6(1):7635, July 2015. Number: 1 Publisher: Nature Publishing Group.

[168] Ludovico Cestarollo, Karthik Srinivasan, and Amal El-Ghazaly. Investigation of perpendicular magnetic anisotropy in Pt/Co20Fe60B20/Pt multilayer structures. *Journal of Magnetism and Magnetic Materials*, 562:169825, November 2022.

[169] Rohit Pachat, Djoudi Ourdani, Maria-Andromachi Syskaki, Alessio Lamperti, Subhajit Roy, Song Chen, Adriano Di Pietro, Ludovic Largeau,

Roméo Juge, Maryam Massouras, Cristina Balan, Johannes Wilhelmus van der Jagt, Guillaume Agnus, Yves Roussigné, Mihai Gabor, Salim Mourad Chérif, Gianfranco Durin, Shimpei Ono, Jürgen Langer, Damien Querlioz, Dafiné Ravelosona, Mohamed Belmeguenai, and Liza Herrera Diez. Magneto-Ionics in Annealed W/CoFeB/HfO2 Thin Films. *Advanced Materials Interfaces*, 9(36):2200690, 2022. _eprint: https://onlinelibrary.wiley.com/doi/pdf/10.1002/admi.202200690.

[170] C. Driemeier, R. M. Wallace, and I. J. R. Baumvol. Oxygen species in HfO2 films: An in situ x-ray photoelectron spectroscopy study. *Journal of Applied Physics*, 102(2):024112, July 2007. Publisher: American Institute of Physics.

[171] Atashi B. Mukhopadhyay, Charles B. Musgrave, and Javier Fdez. Sanz. Atomic Layer Deposition of Hafnium Oxide from Hafnium Chloride and Water. *Journal of the American Chemical Society*, 130(36):11996–12006, September 2008. Publisher: American Chemical Society.

[172] Lu Li, Xin Huang, Yong-Fan Zhang, Xin Guo, and Wen-Kai Chen. First-principles investigation of H2O on HfO2 (110) surface. *Applied Surface Science*, 264:424–432, January 2013.

[173] J. Grollier, D. Querlioz, K. Y. Camsari, K. Everschor-Sitte, S. Fukami, and M. D. Stiles. Neuromorphic spintronics. *Nature Electronics*, 3(7):360–370, July 2020. Number: 7 Publisher: Nature Publishing Group.

[174] Stefano Ambrogio, Pritish Narayanan, Hsinyu Tsai, Robert M. Shelby, Irem Boybat, Carmelo di Nolfo, Severin Sidler, Massimo Giordano, Martina Bodini, Nathan C. P. Farinha, Benjamin Killeen, Christina Cheng, Yassine Jaoudi, and Geoffrey W. Burr. Equivalent-accuracy accelerated neural-network training using analogue memory. *Nature*, 558(7708):60–67, June 2018. Number: 7708 Publisher: Nature Publishing Group.

[175] Xinjiang Zhang, Anping Huang, Qi Hu, Zhisong Xiao, and Paul K. Chu. Neuromorphic Computing with Memristor Crossbar. *physica status solidi (a)*, 215(13):1700875, 2018. _eprint: https://onlinelibrary.wiley.com/doi/pdf/10.1002/pssa.201700875.